



UNIVERSITÉ DE  
SHERBROOKE

Faculté des sciences appliquées

Département de génie électrique et génie informatique

# Nano-ingénierie de bande interdite des semiconducteurs quantiques par recuit thermique rapide au laser

Thèse de doctorat

Spécialité: Génie électrique

Composition du jury:

Jan J. Dubowski, Université de Sherbrooke, directeur

Vincent AIMEZ, Université de Sherbrooke, expert interne

Richard ARÈS, Université de Sherbrooke, expert interne

Amr S. HELMY, University of Toronto, expert externe

Radosław Wojciech Stanowski

Man is worth as much as he gives from himself to others.

**John Paul II**

# RÉSUMÉ

La capacité de fabriquer des substrats semi-conducteurs avec des régions localisées de matériau à bande interdite différente est nécessaire pour la fabrication des circuits photoniques monolithiques intégrés (PIC). Bien que ce sujet ait été étudié pendant trois décennies et que de nombreuses approches d'ingénierie semi-conductrice ont été proposées, le problème d'obtenir des résultats reproductibles a constamment mis au défi les scientifiques et les ingénieurs. Cela concerne non seulement les techniques de transmission sur plusieurs croissances épitaxiales séquentielles et l'épitaxie sélective localisée, mais aussi la technique conventionnelle de puits quantiques intermixés (QWI), étudiée comme une approche post-croissance pour l'ingénierie de bande interdite. Parmi les différentes techniques QWI, celles fondées sur l'utilisation de différents lasers semblent être intéressantes dans le cadre d'une haute précision et concernant le potentiel pour l'ingénierie de bande interdite à bon rapport coût-efficacité. Par exemple, un faisceau laser infrarouge (IR) étroitement focalisé pourrait être utilisé pour le recuit de petites régions d'un substrat semi-conducteurs comprenant différentes microstructures de puits quantiques (QW) ou de points quantiques (QD). La précision d'une telle approche dans la prestation de substrats avec des régions bien définies de matériau à différentes bandes interdites dépendra de la capacité de contrôler la température induite par laser, de la dynamique du processus de chauffage et de refroidissement et de l'utilisation des diagnostics d'ingénierie des bandes interdites.

Dans le cadre de cette thèse, j'ai étudié des processus QWI induit par laser IR sur des substrats QW comprenant des microstructures en GaAs/AlGaAs et en InP/InGaAsP ainsi que des microstructures QD InAs crues sur substrats InP. Dans ce but, j'ai conçu et assemblé un système à deux lasers permettant le recuit thermique rapide de zones sélectives (Laser-RTA) de substrats semi-conducteurs. L'avantage d'une telle approche est d'effectuer un recuit avec un gradient de température chauffage-refroidissement irréalisable avec les techniques classiques RTA, tandis que le faisceau étroitement focalisé de l'un des lasers IR est utilisé pour le 'recuit localisé'. Ces caractéristiques m'ont permis de présenter une nouvelle méthode itérative pour l'ingénierie de bande interdite à certaines zones choisies du substrat semi-conducteur (IBESA). Cette méthode prouve la capacité d'offrir des substrats QW/QD sur GaAs et InP avec les régions à différentes énergies de bande interdite contrôlées à mieux que

$\pm 1$  nm de longueur d'onde d'émission spectrale. La technique IBESA pourraient être utilisées pour affiner les caractéristiques optiques des régions particulières d'une tranche de QW préparées pour la fabrication d'un PIC. En outre, cette approche permet d'affiner la longueur d'onde d'émission des boîtes quantiques individuelles dans des substrats conçus, par exemple, pour la fabrication des émetteurs de photons uniques.

Dans le 1<sup>ier</sup> chapitre de la thèse, je donne un bref aperçu de la littérature sur les techniques QWI et une introduction sur le laser - méthode RTA. Le 2<sup>ième</sup> chapitre est consacré à la description des processus fondamentaux liés à l'absorption de la lumière laser dans les semiconducteurs. Je présente aussi les résultats de la méthode par éléments finis appliquées à la modélisation et la description semi-quantitative de processus Laser - RTA. Les détails de l'installation expérimentale et les procédures développées sont présentés dans le 3<sup>ième</sup> chapitre. Les résultats concernant l'ingénierie directe de bande interdite et l'ingénierie itérative de bande interdite sont présentés et interprétés respectivement dans les chapitres 4 et 5.

Mots clés : Interdiffusion de puits quantique, ingénierie laser de bande interdite, recuit thermique rapide au laser, circuits photoniques monolithiques intégrés, affiner les caractéristiques optiques, réglages des caractéristiques optiques de point quantique.

# ABSTRACT

The ability to fabricate semiconductor wafers with spatially selected regions of different bandgap material is required for the fabrication of monolithic photonic integrated circuits (PIC's). Although this subject has been studied for three decades and many semiconductor engineering approaches have been proposed, the problem of achieving reproducible results has constantly challenged scientists and engineers. This concerns not only the techniques relying on multiple sequential epitaxial growth and selective area epitaxy, but also the conventional quantum well intermixing (QWI) technique that has been investigated as a post-growth approach for bandgap engineering. Among different QWI techniques, those based on the use of different lasers appear to be attractive in the context of high-precision and the potential for cost-effective bandgap engineering. For instance, a tightly focused beam of the infrared (IR) laser could be used for the annealing of small regions of a semiconductor wafer comprising different quantum well (QW) or quantum dot (QD) microstructures. The precision of such an approach in delivering wafers with well defined regions of different bandgap material will depend on the ability to control the laser-induced temperature, dynamics of the heating-cooling process and the ability to take advantage of the bandgap engineering diagnostics.

In the frame of this thesis, I have investigated IR laser-induced QWI processes in QW wafers comprising GaAs/AlGaAs and InP/InGaAsP microstructures and in InAs QD microstructures grown on InP substrates. For that purpose, I have designed and set up a 2-laser system for selective area rapid thermal annealing (Laser-RTA) of semiconductor wafers. The advantage of such an approach is that it allows carrying out annealing with heating-cooling rates unattainable with conventional RTA techniques, while a tightly focused beam of one of the IR lasers is used for 'spot annealing'. These features have enabled me to introduce a new method for iterative bandgap engineering at selected areas (IBESA) of semiconductor wafers. The method proves the ability to deliver both GaAs and InP based QW/QD wafers with regions of different bandgap energy controlled to better than  $\pm 1\text{nm}$  of the spectral emission wavelength. The IBESA technique could be used for tuning the optical characteristics of particular regions of a QW wafer prepared for the fabrication of a PIC. Also, this approach has the potential for tuning the emission wavelength of individual QDs in wafers designed, e.g., for the fabrication of single photon emitters.

In the 1<sup>st</sup> Chapter of the thesis, I provide a short review of the literature on QWI techniques and I introduce the Laser – RTA method. The 2<sup>nd</sup> Chapter is devoted to the description of the fundamental processes related to the absorption of laser light in semiconductors. I also discuss the results of the finite element method applied for modeling and semi-quantitative description of the Laser – RTA process. Details of the experimental setup and developed procedures are provided in the 3<sup>rd</sup> Chapter. The results concerning direct bandgap engineering and iterative bandgap engineering are discussed in the 4<sup>th</sup> and 5<sup>th</sup> Chapters, respectively.

Keywords: quantum well intermixing, laser bandgap engineering, laser rapid thermal annealing, monolithically integrated photonic circuits, quantum dot tuning.

# Acknowledgements

Firstly, I would like to thank Jan J. Dubowski, the director of my Ph.D. project and professor at the Department of Electrical Engineering of Sherbrooke University, for his high quality and valuable mentoring of my Ph.D. research. For his unconditional and friendly support and efforts made towards shaping the young scientist to think creatively and critically in a positive fashion. His continuous interest and engagement in delivery of high quality research and his will of sharing his experience allowed me to perform my Ph.D. study with a great amount of freedom and to communicate and present my Ph.D. project results with other researchers at many international conferences and in scientific journals.

I would like to thank H. Granberg, professor at ‘Centre d’applications et de recherche en télédétection’ (CARTEL) at the Geography Department of Sherbrooke University and S. Chelkowski, professor at the Department of Science at Sherbrooke University for many valuable discussions helping me to look at my Ph.D. project from other perspectives.

I would like to thank prof. V. Aimez, prof. P. Charette, prof. R. Arès, prof. D. Morris, prof. J. Beerens for their kind support and valuable discussions and for providing me access to their laboratories infrastructures.

I would like to thank postdoctoral fellows: Dr. M. Martin, Dr. O. Voznyy, and interns: S. Bouaziz, J. Vermette and M. Bisson-Viens as well as the whole professional researchers and technical support teams at ‘Centre de Recherche en Nanofabrication et Nanocaractérisation’ (CRN2) for support with development of Laser-RTA technique and procedures for preparation and characterization of quantum semiconductor wafers.

I would like to thank my parents Teresa and Stanisław Stanowscy, my sister Joanna Popłońska and my wife Monika Stanowska for their great moral support that allowed me to maintain balance of my professional and family life. I want to thank my children Ania and Paweł Stanowscy for their smiles capable relaxing any stresses and their interest in ‘what Papa was doing with light’.

# Table of Contents

Nano-ingénierie de bande interdite des semiconducteurs quantiques par recuit thermique rapide au laser.....	1
RÉSUMÉ.....	3
ABSTRACT.....	5
Acknowledgements.....	7
Table of Contents.....	8
Table of Figures.....	12
Abbreviations.....	19
Introduction.....	21
Chapter 1.....	23
Quantum semiconductor bandgap engineering - state of the art.....	23
1.1 Epitaxial growth based bandgap engineering.....	23
1.2 Quantum well intermixing.....	26
1.3 Spatially selective QWI techniques.....	29
1.3.1 Impurity Induced Disordering.....	29
1.3.2 Ion Implantation Disordering.....	31
1.3.3 Universal damage technique.....	33
1.3.4 Impurity Free Vacancy Disordering.....	34
1.4 Laser assisted QWI techniques.....	37
1.4.1 Pulsed Laser QWI.....	37
1.4.2 Excimer laser induced QWI.....	38
1.4.3 Nd:YAG laser induced QWI.....	39
1.5 CW infrared Laser – RTA: One-step QWI process.....	42
Bibliography.....	45



Chapter 2 .....	50
Process design for CW IR Laser – RTA of QS wafers .....	50
2.1 Selective area heat generation in Si, GaAs and InP wafers induced with CW 980 and 1064 nm laser beams .....	50
2.1.1 Photon’s energies at 980 and 1064 nm wavelengths.....	51
2.1.2 Laser light interaction with the semiconductor wafer microstructure.....	51
2.1.3 Absorption of laser light radiation by Si, GaAs and InP wafers. ....	54
2.1.4 Antireflection layer of SiO <sub>2</sub> .....	63
2.2 Finite element method of modeling temperature profiles in GaAs and InP semiconductors .....	63
2.2.1 Calculation of the heat transfer .....	63
2.2.2 Transient temperature profiles .....	67
2.2.3 Lateral and in-depth temperature profiles .....	71
2.3 Processing with moving Nd:YAG laser beam.....	74
2.4 Conclusions .....	76
Bibliography .....	77
Chapter 3 .....	82
Infrared Laser Rapid Thermal Annealing Experimental Details.....	82
3.1 QS microstructures .....	82
3.1.1 AX04-182.....	82
3.1.2 RA30360 .....	83
3.1.3 02-161.....	84
3.2 Conventional – RTA QWI.....	85
3.3 Laser – RTA Surface Damage Test.....	86
3.4 Setup description .....	87

3.4.1	Sample holder.....	87
3.4.2	CW laser diode.....	89
3.4.3	Quantronics Q-Mark Condor system .....	90
3.4.4	MIKRON M680 pyrometer.....	94
3.4.5	Custom designed infrared camera (IR-CAM).....	97
3.4.6	Process monitoring camera .....	100
3.5	Photoluminescence mapping .....	102
3.6	Laser – RTA processing methodology .....	103
3.7	Conclusions .....	105
Chapter 4 .....		106
Direct Bandgap Engineering at Selected Sites .....		106
4.1	Introduction .....	106
4.2	Single spot Laser – RTA QWI .....	106
4.3	Resolution of Laser – RTA QWI technique .....	110
4.4	Uniform QWI profiles .....	112
4.4.1	Array of QWI spots .....	112
4.4.2	Array of QWI lines.....	114
4.5	Arbitrary QWI profiles .....	116
4.5.1	Gradually QWI lines for fabrication of superluminescent diodes (SLDs).....	116
4.6	Arbitrary QWI patterns.....	119
Chapter 5 .....		121
Iterative Bandgap Engineering at Selected Areas – IBESA for QW and QD wafers .....		121
5.1	Introduction .....	121
5.2	IR Laser-RTA IBESA of QWs semiconductor wafer .....	122
5.2.1	Experimental details.....	122

5.2.2	Results and discussion.....	123
5.3	IR Laser-RTA IBESA of QDs semiconductor wafer .....	126
5.3.1	Experimental details.....	126
5.3.2	Results and discussion.....	126
5.3.3	Conclusion.....	129
	Summary and prospect .....	131
	Bibliography .....	133
	Appendix .....	138
	LabVIEW interface for IR Laser – RTA IBESA technique.....	138
	Articles written during the PhD thesis: .....	152

# Table of Figures

Figure 1.1.1 AlGaAs waveguide fabrication process flow for MBE single step re-growth technique [Yu, Scaccabarozzi et al. 2003].	24
Figure 1.1.2 Various techniques for achieving active and passive sections orthogonal to the growth direction [Raring and Coldren 2007].	25
Figure 1.2.1 GaAs/AlGaAs waveguide fabricated by using QWI technique [Marsh 1993]. Cross-section schematic diagram of epitaxy grown QW active region: as-grown vs. QWI processed regions (a); corresponding energy band structure (b) and different functionality of active region areas as the result of band edge modification (c).	26
Figure 1.3.1 'Polka-dot' pattern of GaAs-AlAs superlattice disks (38 $\mu\text{m}$ diameter on 76 $\mu\text{m}$ centers) surrounded by (b) yellow-gap $\text{Al}_x\text{Ga}_{1-x}\text{As}$ [Holonyak 1981].	29
Figure 1.3.2 Ion implantation techniques (a) through a metal mask and (b) through a gray-scale dielectric capping layer [Vieu, 2000].	30
Figure 1.3.3 Effective amplitude of photoluminescence peak position wavelength shift vs. the implantation dose [Charbonnea 1998].	31
Figure 1.3.4 Multiple wavelength blueshift versus $\text{SiO}_2$ ion-implantation mask thickness [Aimez, Beauvais et al. 2002].	32
Figure 1.3.5 Schematic diagram of the lattice hops comprised in Ga out-diffusion from the QWs, and the QW interface crossings carried out by group-III vacancies during the random walks associated with their diffusion [Helmy, Aitchison et al. 1998].	34
Figure 1.3.6 Schematic representation of vacancy diffusion profile in $\text{SrF}_2$ masked QW material (not to scale). The high mobility of the vacancies leads to a uniform distribution at the MQWs for patterns of a smaller dimension than the diffusion length (3 $\mu\text{m}$ ) [Boon Siew, 1997].	35
Figure 1.3.7 PL-shift as function of the thickness of PECVD $\text{SiO}_2$ protection layer [Pépin, 2000; Liu, 2000].	36
Figure 1.4.1 Low temperature photoluminescence spectra after UV laser irradiation and annealing at 900°C [Genest, Dubowski et al. 2004].	38
Figure 1.4.2 PL map of ArF induced selected area intermixing (a) and dependence of the blueshift amplitude (b) [Genest, Beal et al. 2008].	39

Figure 1.4.3 Schematic diagram of the interference grating structuring of an MBE-grown QW system, and the radiative processes due to the resulting modulation [Kelly, Nebel et al. 1996].	40
Figure 1.4.4 (a) Scanning electron microscopy image of a GaAs micro-disk containing In(Ga)As QDs and schematic illustration of the ILP method. Inset: Atomic force microscopy image of self-assembled In(Ga)As QDs (dark in the image) with low surface density. (b) Calculated temperature profile for a micro-disc [Rastelli, Ulhaq et al.]	41
Figure 2.1.1 Absorption of light in a semiconductor material	52
Figure 2.1.2 The schematic of incident laser beam on the semiconductor surface [Steen 1998]	53
Figure 2.1.3 Schematic of the valence band, direct and indirect bandgap conduction bands. The curves I, II and III in the valence band are called heavy hole, light hole, and split-off hole states respectively [Singh, 2000]	54
Figure 2.1.4 Schematic of the indirect energy bandgap for Si (a) and the direct energy bandgaps of GaAs (b) and InP (c) [Singh, 2000]	55
Figure 2.1.5 Energy bandgap deformation: elastic (a) and electrostatic (b) [Bacewicz 1995]	55
Figure 2.1.6 Optical transitions with participation of shallow donors (a) Absorption spectra for donors (b) and acceptors (c). Dashed line on (b) and (c) corresponds to interband absorption [Bacewicz 1995]	56
Figure 2.1.7 Transitions acceptor - donor (a), acceptor – donor transition energy dependence on acceptor – donor distance [Bacewicz 1995]	56
Figure 2.1.8 Thermalisation of excited electrons ( $\hbar\omega_0$ – absorbed photon energy, $\hbar\omega_e$ emitted photon energy) (a) and influence of occupied states in conduction band on optical transitions. Burstein-Moss effect. $E_F$ - Fermi energy (b) [Bacewicz 1995]	57
Figure 2.1.9 Calculated dependence of the $E_g$ for Si, GaAs and InP semiconductor materials according to the temperature. Vertical lines indicate temperatures at which $E_g$ of GaAs and InP equals the photons energies of the LD or Nd:YAG lasers respectively	58
Figure 2.1.10 Absorption edge of silicon at two different temperatures [Bacewicz 1995] (a) and of GaAs at 109 °C and InP at 108 °C [Beaudoin, DeVries et al. 1997] (b)	59

Figure 2.1.11 Low-level absorption spectrum of high purity Si at various temperatures (a) [Macfarlane, McLean et al. 1959] and absorption coefficient vs. photon energy at different temperatures (b) [Sze 1981; Jellison and Modine 1982].	60
Figure 2.1.12 GaAs intrinsic absorption coefficient near the intrinsic absorption edge for different temperatures (a) [Sturge 1962] and absorption coefficient versus photon energy (b) [Casey, Sell et al. 1975].	60
Figure 2.1.13 InP intrinsic absorption coefficient near the intrinsic absorption edge for different temperatures (a) [Turner, Reese et al. 1964] and absorption coefficient vs. photon energy (b) [Aspnes and Studna 1983].	61
Figure 2.1.14 Structure of Laser - RTA processed QS wafer (a) and energy band structure of active region (b).	62
Figure 2.2.1 Thermal conductivity dependence on temperature - $k(T)$ (a) and optical absorption dependence on temperature - $\alpha(T)$ (b) [Stanowski 2005].	67
Figure 2.2.2 Emissivity dependence on maximum temperature [Stanowski 2005].	68
Figure 2.2.3 Calculated vs measured ( $\epsilon = 1$ ) transient point GaAs wafer temperature induced with 980 nm LD (a) emissivity corrected ( $\epsilon = 0.7$ ) (b).	68
Figure 2.2.4 Calculated vs measured ( $\epsilon = 0.7$ ) transient point Si wafer temperature induced with 980 nm LD and 1064 nm Nd:YAG lasers [Stanowski and Dubowski 2009].	69
Figure 2.2.5 Calculated vs measured ( $\epsilon = 0.7$ ) transient point GaAs (a) and InP (b) wafers temperature induced with 980 nm LD and 1064 nm Nd:YAG lasers [Stanowski and Dubowski 2009].	70
Figure 2.2.6 Lateral (a) and in-depth (b) temperature profiles induced with 700 $\mu\text{m}$ in diameter Nd:YAG laser beam for various convection ( $h=0 ; 20 ; 100$ ) coefficients [Stanowski 2005].	71
Figure 2.2.7 Lateral (a) and in-depth (b) temperature profiles induced with 100 $\mu\text{m}$ in diameter Nd:YAG laser beam [Stanowski 2005].	71
Figure 2.2.8 Lateral (a) and in-depth (b) temperature profiles induced with 700 $\mu\text{m}$ in diameter Nd:YAG laser beam [Stanowski 2005].	72
Figure 2.2.9 Lateral (a) and in-depth (b) temperature profiles induced with 100 $\mu\text{m}$ in diameter Nd:YAG laser beam [Stanowski 2005].	72

Figure 2.2.10 Calculated temperature profiles on the surface and 2 $\mu\text{m}$ below the surface for InP wafer irradiated by laser beams of 100 $\mu\text{m}$ (a) and 12 $\mu\text{m}$ (b) diameters. Horizontal, dotted line indicates the threshold temperature for which a 90 s RTA includes no significant PL shift [Voznyy 2006].....	73
Figure 2.3.1 Modulo function implemented to the equation 2.3.1 for modeling of the moving laser beam. ....	74
Figure 2.3.2 Surface temperature plot for 3 chosen moments of irradiation by rapidly moving laser beam (a) and corresponding lateral temporal temperature (b) [Stanowski 2005].....	75
Figure 2.3.3 Temperature profiles along the center of an InP sample induced with 41W 980 nm LD (24 mm diameter spot) and a spot (500 $\mu\text{m}$ ) of the 1.2 W Nd:YAG laser moving in one direction (a) and in two directions (b) [Stanowski 2005]. ....	75
Figure 3.1.1 Slab diagram of AX04-182 wafer microstructure (a) and its PL spectrum in range 750 – 880 nm (b). ....	83
Figure 3.1.2 Slab diagram of RA30360 wafer microstructure (a) and its PL spectrum in range 1450 – 1580 nm (b). ....	84
Figure 3.2.1 Conventional rapid thermal annealing of AX04-182 induced QWI corresponding shift of the PL peak position. ....	85
Figure 3.3.1 Laser - RTA test of surface damage threshold.....	86
Figure 3.4.1 Schematic diagram of the infrared laser rapid thermal annealing experimental setup.....	87
Figure 3.4.2 Cross-section (a) and top view (b) of the sample holder 1 – sample; 2 – Si wafer; 3a – opening in a graphite plate; 3b – graphite plate; 4 – fused silica spacer; 5 – Al 2'' ring; 6 – stainless steel ring; 7 – laser diode fiber; 8 – fused silica rod holder; 9 – Al support pin; 10 – Theta circular motor; 11 – fiber housing; 12 graphite ring beam stopper.....	88
Figure 3.4.3 Apollo Instruments Inc. CW, $\lambda=980$ nm, fiber pigtailed laser diode [Apollo_Instruments_Inc,]. ....	89
Figure 3.4.4 The GaAs/AlGaAs $\lambda=980$ nm CW LD output power [W] vs power supply current [A] dependence curve.....	90
Figure 3.4.5 Quantronics Condor Nd:YAG laser marker processing unit [Quantronix] .....	91
Figure 3.4.6 Nd:YAG 1064 nm CW laser output power after 50/50 % beam splitter [W] vs power supply current [A] dependence curve.....	91

Figure 3.4.7 The 100 $\mu\text{m}$ (a) and 500 $\mu\text{m}$ (b) according to 4 $\sigma$ criterion Nd:YAG laser beam profiles measured with LBA-FW Ophir - Spiricon Inc. beam profiler. ....	92
Figure 3.4.8 Photo of the developed Laser - RTA setup .....	93
Figure 3.4.9 Mikron pyrometer set. Infrared sensor unit (a), connecting optical fiber (b), lens assembly (c) [Mikron_Infrared_Inc]. ....	94
Figure 3.4.10 Mikron M680 radiation collection spot. Measurement setup (a). Measured profile (b).....	95
Figure 3.4.11 Temperature maps of the Laser – RTA processed AX04-182 wafer irradiated with (a) LD only and (b) LD and Nd:YAG laser beams. ....	96
Figure 3.4.12 Custom designed IR-CAM assembly elements. Standard USB interfaced ‘Pine’ webcam (a) and 820 – 840 nm infrared bandpass filter (b) [Pine]. ....	97
Figure 3.4.13 Schematic diagram of the IR-CAM calibration setup.....	98
Figure 3.4.14 IR-CAM temperature distribution map of 2" Si wafer irradiated with LD 980 nm beam (a) and its cross-section plot (b).....	98
Figure 3.4.16 LD 980 nm beam transmission intensity through a 2" Si wafer map (a) and cross-section profile (b).....	99
Figure 3.4.15 IR-CAM temperature distribution map of 2" GaAs wafer irradiated with LD 980 nm beam (a) and its cross-section plot (b).....	99
Figure 3.4.17 Commercially available 2MP ‘Rocketfish’ webcam used for process monitoring and sample repositioning [Rocketfish]. ....	101
Figure 3.6.1 Block diagram of Laser - RTA process (green – function name; yellow - common steps ; red - specific steps for chosen process). ....	103
Figure 3.6.2 Block diagram of the IR Laser – RTA IBESA technique processing steps.....	104
Figure 4.2.1 PL map of a single Laser-RTA irradiated spot (a) and the PL map cross-section profiles of blue-shift amplitude vs. the lasers induced surface temperature (b).....	107
Figure 4.2.2 Blue-shift amplitude vs. the 30 sec irradiation time with variable Nd:YAG laser power (a) and a profile of the QWI site that was blue-shifted by 230 nm (b).....	107
Figure 4.2.3 PL map of a single Laser-RTA irradiated spot (a) and the PL map cross-section profiles of blueshift amplitude vs. the lasers induced surface temperature.....	109
Figure 4.2.4 Dynamics of bandgap engineering of AX04-182 microstructure induced with Laser-RTA technique. ....	109



Figure 4.3.1 PL wavelength map of AX04-182 with 4 written spots (a) and their corresponding PL cross-section curve (b).	111
Figure 4.3.2 Selectivity of the Laser – RTA bandgap engineering technique illustrated on PL wavelength map of AX04-182 microstructure.	111
Figure 4.4.1 PL map of AX04-182 that was irradiated at nominally the same conditions in nine spots (a), and the PL peak position plot along A-A direction (b).	113
Figure 4.4.2 PL maps of AX04-182 irradiated under nominally identical conditions in nine spots (a) and after spots 2, 4, 6 and 8 additionally irradiated for 40 sec (b).	113
Figure 4.4.3 PL map of a Laser - RTA processed InGaAsP/InP QW sample with 5 lines of the intermixed material (a), PL peak position along the as-grown material, line 1, and the Laser - RTA produced line 2 of the intermixed material (b), and PL peak position across the sample (c).	115
Figure 4.5.1 PL map of a Laser - RTA processed AX04-182 QW wafer with 3 lines of gradually QWI material (a) and PL peak position along the line #1 (b).	117
Figure 4.5.2 PL map of a Laser - RTA processed AX04-182 QW wafer with 3 arbitrary gradient lines of QWI material (a) and PL peak position along the line #3 (b).	117
Figure 4.5.3 PL wavelength map of a sample exposed to a CW laser beam moving at variable speed (a) and the bandgap energy profile along the AB line (b).	119
Figure 4.6.1 PL wavelength map of the Laser - RTA processed RA30360 sample with a 'watermark' of the QWI material.	120
Figure.5.2.1. Schematic idea of the IBESA process.	123
Figure 5.2.2 PL peak wavelength map of an InGaAs/InGaAsP QW wafer with 20 sites of QWI material fabricated by Laser-RTA (a), and PL spectra of the as-grown and 70 nm blueshifted (site A3) materials (b). The inset shows details of the processed microstructure.	124
Figure 5.2.3 PL peak wavelength cross-scans for A1, A2, A3 and A4 sites following the 1st (a), 2nd (b) and 3rd (c) IBESA annealing step.	125
Figure 5.2.4 PL peak wavelength cross-scans for B1, B2, B3 and B4 sites following the 1st (a), 2nd (b) and 3rd (c) IBESA annealing step.	125
Figure 5.3.1 PL peak emission wavelength maps and corresponding cross-scans for A1, A2, A3, B1, B2, B3 following the 1st (a,c) and last (b,d) emission wavelength tuning steps.	128
5.3.2 PL spectra of the as-grown and 15 nm (green) and 25 nm (red) blueshifted materials.	129

Figure 6.1.1 LabVIEW based IR Laser – RTA IBESA interface. In-situ process monitoring, position or reposition section.....	<b>Erreur ! Signet non défini.</b>
Figure 6.1.2 Block diagram of sample repositioning processing steps. ....	139
Figure 6.1.3 Video Image with detected horizontal and vertical sample's edges.....	140
Figure 6.1.4 Sample on processing stage. Two straight lines denominate its position in the camera's field of view. ....	141
Figure 6.1.5 Console presenting actual direction of sample's movement .....	142
Figure 6.1.6 Change detection image a) before and b) after sample's repositioning process..	143
Figure 6.1.7 Sum pix Intensity in ROI a) before and b) after sample's repositioning process	143
Figure 6.1.8 Sample repositioning technique based on differential pixels intensity counting. ....	144
Figure 6.1.9 Move sample routine.....	145
Figure 6.1.10 LabVIEW based IR Laser – RTA IBESA interface. Automated processing routines. ....	145
Figure 6.1.11 Variable speed sample displacement module .....	146
Figure 6.1.12 Measured and expected temporal temperature behavior measured with the first channel of M680 pyrometer .....	147
Figure 6.1.13 IR-CAM module .....	148
Figure 6.1.14 Nd:YAG galvo-scanner interface controller .....	148
Figure 6.1.15 Nd:YAG power stability monitor .....	149
Figure 6.1.16 IR LD current control module.....	150
Figure 6.1.17 IBESA PROCESS routine module .....	150

# Abbreviations

FEM – finite element method

IBESA – Iterative bandgap engineering at selected areas

Laser – RTA – Laser Rapid Thermal Annealing

ILP – in-situ laser processing

$J_{th}$  - threshold current density

MQWs – multi quantum wells

NA – numerical aperture

Nd:YAG – neodymium-doped yttrium aluminum garnet

PICs – photonic integrated circuits

PIDs – photonic integrated devices

PAID – photo-absorption induced disordering

QD – quantum dot

QDI – quantum dot intermixing

QS – quantum semiconductor

QW – quantum well

QWI – quantum well intermixing

VGa – Ga atom vacancy

TMA - trimethylaluminum

Bandgap nanoengineering of quantum semiconductors  
with a laser rapid thermal annealing technique

Thèse de doctorat

# Introduction

Selective area semiconductor bandgap engineering is one of the base technologies required for manufacturing of Photonic Integrated Circuits (PIC's) [Miller, 1969; Heidrich, 2003]. Typically, a circuit consisting of two active elements, such as a semiconductor laser and an optical modulator, is set together from two different components that have to be aligned and stitched together. The ability to fabricate various elements of the PIC's within same semiconductor wafer has the potential to offer devices with improved overall efficiency at significantly reduced costs. This stems from the fact that different wafer components could be made inherently aligned with each other, which would lead to the significantly reduced packaging costs. Bandgap engineering has been traditionally achieved by multiple spatially selective sequential epitaxial growth, etch and re-growth steps.

Selective area epitaxy is conventionally the most flexible and widely used method for fabrication of multi-bandgap wafers [Yap, Elliott et al. 2001]. However, the re-growth method is relatively complex and suffers from the lack of manufacturing precision/reproducibility that is critical for PICs. For instance, the achieved energy bandgap profiles are known only after the growth as no precise diagnostics exists to monitor and control such a process in-situ.

In this context, a quantum well intermixing (QWI) technique, which is a post-growth bandgap engineering process, has been given a significant attention [Li, 2000; Skogen, 2005; Pan, 2008]. The attraction of the QWI process is in its ability to deliver multi-bandgap wafers produced with an epitaxial technique setup for the growth of a nominally same-bandgap material. The spatially selective use of QWI technique allows tuning of the optical characteristics in a single epi-wafer for optimizing performance of PIC's elements such as laser sources, photodetectors, waveguides, modulators, etc. QWI relies on modification of quantum well/barriers interfaces sharpness due to intentional (elevated temperature) induction of diffusion of atoms from barriers towards the well region. This results usually in increase of the QW bandgap energy what blue-shifts the QW emission wavelength. Post-growth QWI techniques such as impurity induced disordering (IID) and impurity free vacancy disordering (IFVD) require multiple masking steps and are followed by non-selective area rapid thermal

annealing processing step. Post-growth processes reported in literature [Marsh, 1993; Dubowski, 1999; Boon Siew, 2004; Genest, 2007] that incorporate lasers for selective area QWI suffer from multi-step or long processing routines, bulky setups and not sufficient control of the induced blue-shift amplitudes reproducibility. Although the idea of PIC's fabrication is known since more than three decades and many methods were developed and proposed to address subject of selective area semiconductor bandgap engineering, there is still no PIC's fabrication technique, which would offer high reproducibility of spectral control of monolithically integrated regions with different bandgap material that maintain comparable to as-grown structure signal intensity from the QWI processed areas. In the frame of this work I have developed the IR Laser – RTA technique and corresponding instrument comprising two IR laser sources to address the cost-efficient monolithic fabrication of arbitrary shape patterns of QWI material in a one-step process. This IR Laser – RTA technique takes advantage of rapid on/off switching and precise control of the laser beam intensity during the process and simplicity of bringing the processing laser across the desired pattern what makes it a strong candidate for quasi-instantaneous spatially selective emission wavelength tuning of QWs/QDs semiconductor wafers.

# Chapter 1

## Quantum semiconductor bandgap engineering - state of the art

In this chapter I provide a short review of the semiconductor bandgap engineering techniques. I also highlight the attractive features of an infrared (IR) laser for the rapid thermal annealing of quantum well (QW) and quantum dot (QD) microstructures.

### 1.1 Epitaxial growth based bandgap engineering

Monolithic integration of individual optoelectronic devices in a photonic integrated circuit (PIC) has been a goal actively pursued worldwide after Miller's original proposals in late sixties of 20<sup>th</sup> century [Miller 1969]. The selective area epitaxial growth, etching and re-growth at selected areas of a semiconductor wafer has been arguably the most frequently investigated approach employed for this purpose. It requires both the precise control of a set of epitaxial growth parameters and multiple masking steps. It suffers from optical propagation losses at the re-grown interfaces because of various dimensions and refractive indices of adjacent alloys forming the optical path [Trivedi and Anderson 1996; Ravindra, Ganapathy et al. 2007]. The structure in Fig. 1.1.1 presents the template fabrication process for elimination of waveguide core corrugation and high transmission loss, however the alignment of adjacent regions has been improved the inherent disadvantage of sticking together of various alloys with different average compositions of atoms that persists and results in refractive index discontinuity between adjacent sections which causes parasitic reflections and degrades performance of the photonic device.

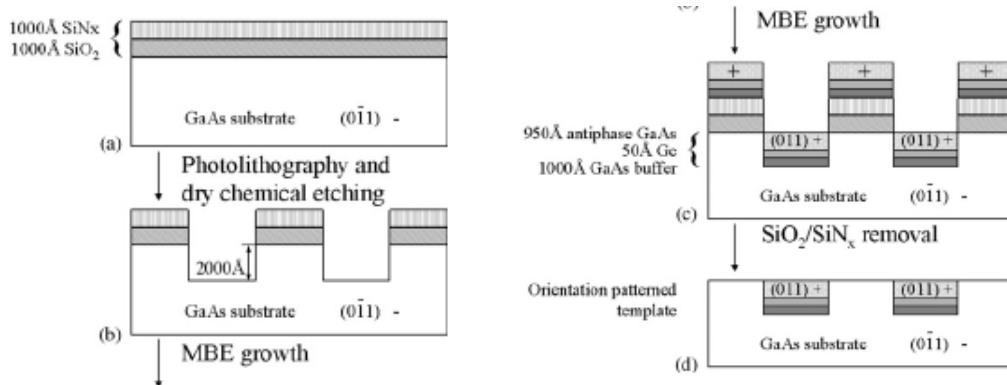


**Figure 1.1.1 AlGaAs waveguide fabrication process flow for MBE single step re-growth technique [Yu, Scaccabarozzi et al. 2003].**

Various growth-regrowth techniques of selective area fabricated couplings of the active and passive sections are presented in figure 1.1.2. These coupling techniques are responsible for the optical loss and final performance of the device. The technologically sophisticated butt-joint technique (figure 1.1.2 a) suffers from difficulty in achieving high optical quality butt-joint interfaces and losses in the optical waveguide [Wallin, Landgren et al. 1992; Tiemeijer 1997]. The selective area growth technique (figure 1.1.2 b) although provides multiple bandgap edges across the fabricated chip, it requires high-degree of calibration/optimization and control of the MOCVD reactor conditions. A simple - one step, blanket type regrowth – offset QW technique (figure 1.1.2 c) allows for only two band-edges on a single-chip. In the dual QW technique (figure 1.1.2 d) the MQW region is grown in the center of the bulk waveguide below the offset MQW, such as the second QW band-edge is defined on the single-chip. The dual QW platform cannot provide optimal modal gain to the laser active region, since the peak of mode is offset from the wells. The asymmetric twin waveguide structure (figure 1.1.2 e) is realized by the growth of multiple waveguides on top of each other and followed by selective removal of the upper ‘active’ waveguide in such a way that the lower ‘passive’ waveguide remains in the areas where ‘active’ functions are not required. Although this approach eliminates regrowth step, the nature of the vertical coupling into different epitaxial layers creates great difficulty. These various epitaxial bandgap engineering techniques presented in figure 1.1.2 require high-degree of optimization and control of epitaxy, photolithography and etch processes parameters.



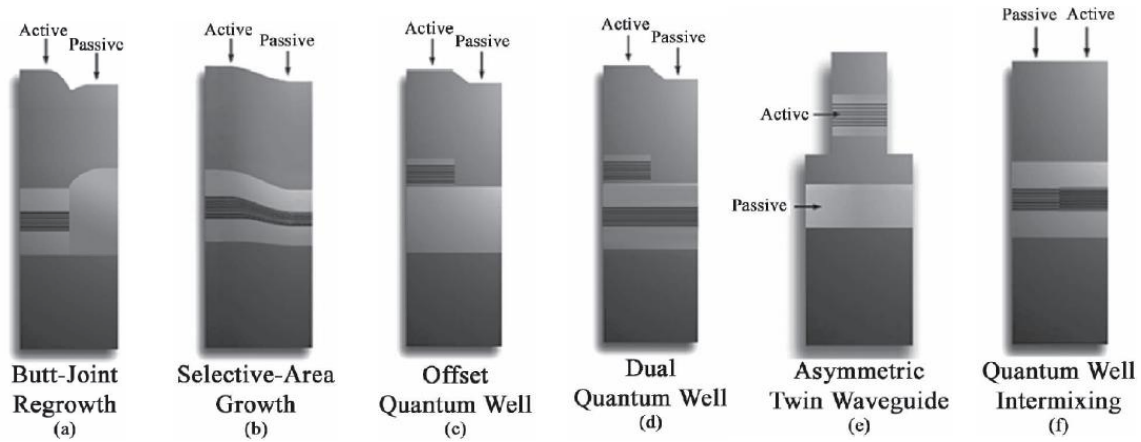


**Figure 1.1.2 Various techniques for achieving active and passive sections orthogonal to the growth direction [Raring and Coldren 2007].**

The alternative QWI technique (figure 1.1.2 f) is a strategic approach that eliminates the multiple epitaxy growth-regrowth processing cycles, while offering spatially selective fabrication of regions of multiple band-gaps across the processed chip. QWI does not change the average composition of the MQW region therefore there is a negligible refractive index discontinuity at the interface between the adjacent QW sections what eliminates parasitic reflections that could degrade the performance of the device. Selective growth-regrowth methods due to their inherent complicity and use of expensive epitaxial growth systems and ultra-clean environment require development of rapid, post-growth selective area emission wavelength tuning techniques that are required to increase the production yield of low-cost Photonic Integrated Circuits.

## 1.2 Quantum well intermixing

The selective area semiconductor bandgap engineering may be performed after the epitaxial growth of the MQW or QD microstructure by employing the QWI process. This technique takes advantage that a QW is inherently a meta-stable system due to the large concentration gradient of atomic species across the QW and barriers interfaces. Figure 1.2.1 presents schematically the QWI processed and as-grown regions of GaAs/AlGaAs QW material. The QWI leads to the change of the atomic concentration profile from an abrupt to graded-like (figure 1.2.1 (a)). Diffusion of atoms in the crystal lattice across the QW/barrier interface decreases the sharpness of the energy wave function profile as shown in figure 1.2.1 (b).

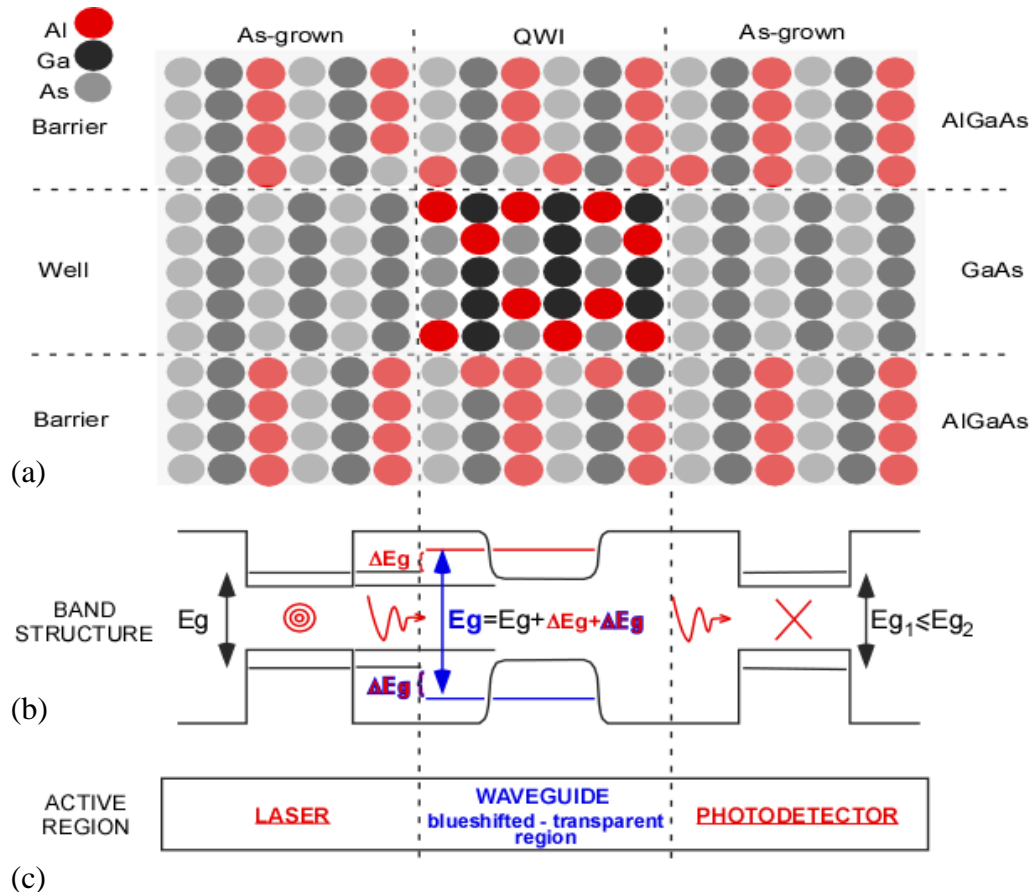


Figure 1.2.1 GaAs/AlGaAs waveguide fabricated by using QWI technique [Marsh 1993]. Cross-section schematic diagram of epitaxy grown QW active region: as-grown vs. QWI processed regions (a); corresponding energy band structure (b) and different functionality of active region areas as the result of band edge modification (c).

This affects the optical properties of the QWI processed region and decides the functional behaviour of the QWI region as an active or passive element of the integrated photonic circuit as shown in figure 1.2.1 (c). QWI results in change of effective mass of charge carriers and refractive index change. The change in refractive index can be used to provide optical confinement [Kapon, Stoffel et al. 1988, Wolf, 1989], gratings [Ralston, Wicks et al. 1986], or even laser reflectors [Holonyak 1981, Laidig, 1984]. The QWI process has been employed to fabricate a waveguide region in GaAs/AlGaAs QW microstructure [Marsh 1993]. The bandgap of intermixed alloy becomes usually larger than that of the original QW microstructure and relies on group V sublattice interdiffusion. However it may turn smaller if the group III sublattice interdiffusion rate become dominant at low annealing temperatures [Nie, Mei et al. 2006]. The changes of wave-function modify the confined energy levels in the QW. These levels in QW mechanical structure can be deduced approximately upon having information about PL shift and solving the Time Independent Schrödinger (TIS) equation:

$$H_{op} \Psi_i = E_i \Psi_i \quad (1.1)$$

where,

$$H_{op} = \frac{-\hbar^2}{2m} \frac{\partial^2}{\partial x^2} + V(x)$$

- operator associated with the system energy called Hamiltonian

$$\frac{-\hbar^2}{2m} \frac{\partial^2}{\partial x^2}$$

- kinetic energy operator, where m is the mass of the particle,

$$V(x)$$

- potential energy at position 'x',

$$E_i$$

- standing wave solutions, which are the states with definite energy values,

$$\Psi_i$$

- probability amplitude for the particle to be found at position 'x'

The diffusion coefficients can be calculated from the confined bandgap energy shifts by solving the potential profile induced by the QWI process and TIS equation. The diffusion constant has been reported to be the same in the wells and barriers [Cibert, Petroff et al. 1986, Schlesinger, 1986]. This constant can be determined from the Fick's second law in the direction of crystal growth:

$$\frac{\partial C}{\partial t} = D \frac{\partial^2 C}{\partial x^2} \quad (1.2)$$

where  $C(x,t)$  is the Al concentration and  $D(=D_{QW}+D_B)$  is the diffusion constant in wells ( $D_{QW}$ ) and barriers ( $D_B$ ).

The solution is:

$$C(x,t) = \frac{1}{2\sqrt{\pi Dt}} \int_{-\infty}^{\infty} f(\lambda) \exp\left(-\frac{(\lambda-x)^2}{4Dt}\right) d\lambda \quad (1.3)$$

where the initial condition is:

$$t = 0, c(x,0) = f(x), -\infty < x < \infty \quad (1.4)$$

The diffusion length is defined as  $\Delta = \sqrt{Dt}$ , which is related to the degree of disordering.

The temperature dependence of interdiffusion can be described by:

$$D(T) = D_0 \exp\left[\frac{-E_A}{K_B T}\right] \quad (1.5)$$

where  $E_A$  is the activation energy,  $K_B$  is Boltzmann's constant,  $T$  is the absolute temperature. It is clear from this formula that the diffusion processes are more effective at elevated temperatures. Atomic interaction within the lattice depends on the potential energy stored by an atom. This energy can be modified by cooling or heating the atoms. It can be achieved in macro-scale by modifying the temperature of the whole crystal or more selectively by irradiation of a selected part of the crystal with the focused laser beam. After the atom's potential energy exceeds the activation energy for displacement (depending on its mass, radius and electrical properties), it can travel among other atoms in the lattice in hopping manner until it loses its energy overload and takes interstitial or any other position. Atoms are supplied with energy of crystal lattice oscillations, which are called phonons. The movement of Ga atoms take place mostly through vacancy diffusion, therefore the profile of the diffused Al arises from a certain number of Ga hops in lattice [Helmy, Aitchison et al. 1998].

### 1.3 Spatially selective QWI techniques

In all cases, QWI leads to exchange of inherent positions between the atoms in QW and barriers at amounts dictated by diffusion rates. It is possible to enhance or prevent the QWI process by implementing various processing steps and/or choosing proper QWI technique. The most commonly studied selective area bandgap modification techniques take advantage of impurity-induced disordering (IID) and impurity-free vacancy disordering (IFVD) and laser assisted QWI techniques described in section 1.4.

#### 1.3.1 Impurity Induced Disordering

Impurity induced disordering has been studied as post-growth, selective area, bandgap engineering technique for fabrication of various forms of double-heterostructure and quantum-well heterostructure lasers capable for continuous operation at room-temperature. Disc-shaped IR-red GaAs-AlAs superlattice lasers that were monolithically integrated into rectangular yellow gap were demonstrated [N. Holonyak 1981]. The yellow-gap  $\text{Al}_{0.77}\text{Ga}_{0.23}\text{As}$  was generated by low temperature Zn diffusion (575 °C, 30min), which has disordered selected portions of the superlattice. Complementary regions were masked to prevent disordering with  $\text{Si}_3\text{N}_4$ . The array of fabricated lasers is presented in Figure 1.3.1. The presented result made

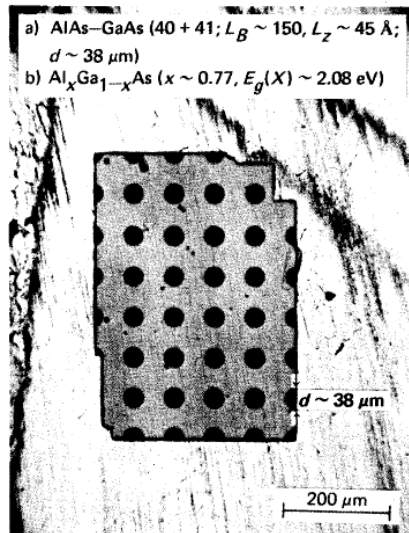
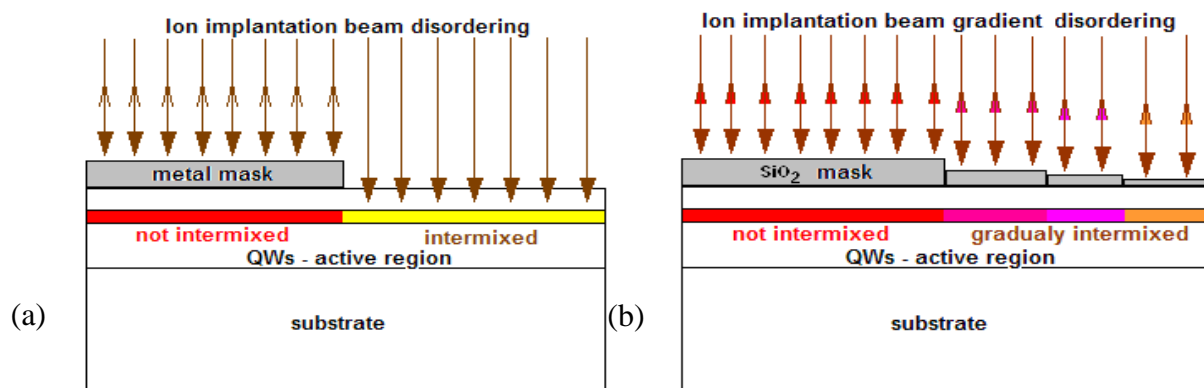


Figure 1.3.1 'Polka-dot' pattern of GaAs-AlAs superlattice disks (38 μm diameter on 76 μm centers) surrounded by (b) yellow-gap  $\text{Al}_x\text{Ga}_{1-x}\text{As}$  [Holonyak 1981].

clear evidence that it is possible to fabricate an optoelectronic chip with a large variety of narrower-gap elements. Further investigations were conducted using other atoms as impurities such as Be, Ge, Mg, S, Se, Si and O [Jagadish 2000- Kahen, 1990]. Dopants are simply divided into two major groups – electrically and non-electrically active species. It has been demonstrated that introduction of all these impurities leads to presence of Al-Ga disordering at significantly lower annealing temperatures. The relation between the concentration of point defects induced by ion implantation and resulting QWI has been studied for InGaAsP microstructures using SiO<sub>2</sub> mask of different thicknesses and is shown in figure 1.3.1 [Vieu, 2000]. Figure 1.3.1 presents the Impurity Induced Disordering techniques, which utilize metal or grey-scale masks lithography. In brief, the spatial control of the SiO<sub>2</sub> mask thickness is achieved by using a grey-mask lithography technique followed by a one-step reactive-ion etching (RIE) process. The near surface low-energy ion beam is used to increase the surface density of point defects, which in turn, increase spatially the QWI process rate and widening the energy bandgap across a planar QW system. This technique clearly offers fabrication of various bandgap materials but introduces residual impurities into the QW crystal layers that act as recombination centers and therefore are detrimental to the optical quality of the intermixed regions what limits the performance of such fabricated optoelectronic devices, i.e. its use for fabrication of passive optical elements such as waveguides [Kappon 1988]. More recent studies have used chemically identical inert ions (inert gases) or ions that are identical to the constituent atoms of the material system (Al, Ga, As) [Marsh, Hansen et al. 1991];[Vieu, Schneider et al. 1991];[Laruelle, Bagchi et al. 1990].



**Figure 1.3.2 Ion implantation techniques (a) through a metal mask and (b) through a gray-scale dielectric capping layer [Vieu, 2000].**

### 1.3.2 Ion Implantation Disordering

Ion implantation is a versatile technique employed for for bandgap engineering of precisely selected regions of the QW semiconductor wafer with control over introduced defects profiles by selecting the appropriate ion energy or dose. The ion implantation technique uses ions of the same kind of atoms that the quantum microstructure consists of. Depending on the ion acceleration energies there are two different approaches to perform the ion induced disordering of quantum semiconductor wafers. The original approach uses high acceleration energies (0.5 to 10MeV), which dopes the semiconductor material across the quantum well layers and also often through the whole thickness of the processed wafer. The less invasive approach uses low acceleration energies (below 500 keV) to implant ions into the very first layers of processed semiconductor wafer – above the QW region. In both cases the implanted ions collide with the atoms of the semiconductor crystal lattice and displace them from their inherent positions what results in the formation of multiple point defects - vacancies and interstitials called the Frenkel's pairs defects. The result of effective blue-shift achieved in AlGaAs/GaAs based microstructure vs. used ion implantation dose is presented in figure 1.3.2.

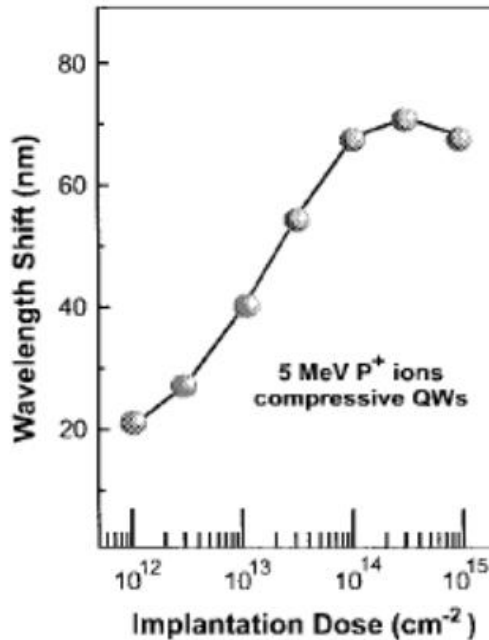
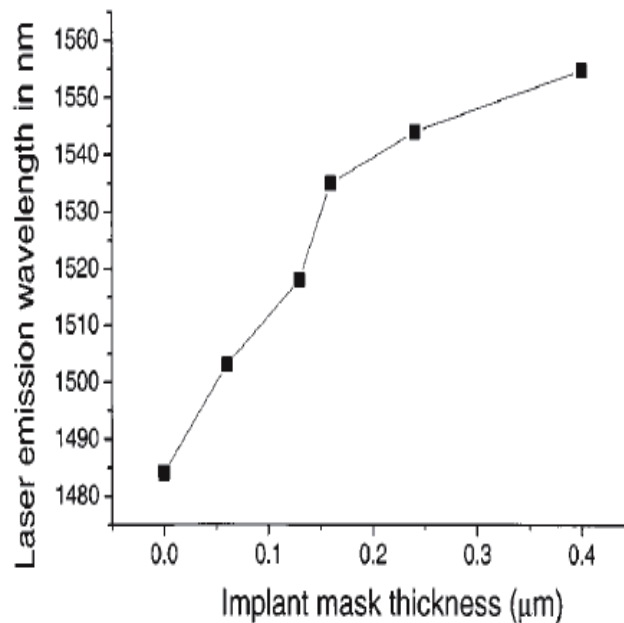


Figure 1.3.3 Effective amplitude of photoluminescence peak position wavelength shift vs. the implantation dose [Charbonnea 1998].

It demonstrates that the ion implantation doses of  $10^{12} \text{ cm}^{-2}$  up to  $10^{14} \text{ cm}^{-2}$  were sufficient to achieve significant blue-shift amplitudes. Further increase of implantation dose results in higher concentration of point defects and material disordering and deterioration however it does not lead to higher blue-shift amplitudes. The AlGaAs/GaAs based QW microstructures demonstrate high thermal stability of the lattice against disordering. They require ion implantation with high acceleration energies in order to achieve relevant amplitudes of blue-shift by QWI during the following RTA processing step. The induced blue-shift amplitude is proportional to the amount of the implanted impurities and their diffusion rates. Low-energy ion-implantation QWI technique has been employed to fabricate moderately blueshifted (i.e., by about 30 nm) discrete laser diodes with characteristics (threshold current density -  $J_{th}$  and slope efficiencies) that are identical to that of devices from as-grown material. It must be noted that the penetration depth and the degree of damage to the lattice structure are increased for higher implantation energy of impurities. There have been also fabricated for the first time intracavity electro-absorption modulators that were monolithically integrated with laser devices [Aimez, Beauvais et al. 2002]. Figure 1.3.2 presents the selective area induced multiple wavelengths blueshift versus  $\text{SiO}_2$  ion-implantation mask thickness [Aimez, 2002].



**Figure 1.3.4** Multiple wavelength blueshift versus  $\text{SiO}_2$  ion-implantation mask thickness [Aimez, Beauvais et al. 2002].



The low energy ion implantation QWI method is of particular interest, especially in device fabrication because complications and reliability problems that may be associated with extensive crystal lattice damage can be avoided. In the fabrication of semiconductor lasers, different types of implanted ions can be used. Nevertheless, the introduced defects must be removed in device applications. The ion implantation technique takes advantage of the RTA processing step to initialize and enhance the QWI process. RTA treatment improves the mobility of carriers by reducing the lattice damage due to annihilation of generated point defects. The typical RTA processing times are in range of 10-20 seconds in the temperature range depending on the processed QWs material system (typically from 750 to 975°C for AlGaAs/GaAs systems). During the annealing step, the layers intermix and ion implantation damage, if present, is removed to a large extent [Ziegler 1992]. Although ion implantation technique offers control of spatial area selectivity the usefulness of this technique is limited by the potential doping of the material introduced during the process. Moreover, the process on ion implantation disordering may suffer from variation of SiO<sub>2</sub> grey-scale mask thickness and porosity, which depend strongly on the SiO<sub>2</sub> deposition technique [Vieu, 2000].

### **1.3.3 Universal damage technique**

The dielectric deposition technique plays a major role, because it can affect the quality of the key SiO<sub>2</sub>/GaAs or SiO<sub>2</sub>/InP interface. The universal damage technique relies on SiO<sub>2</sub>, Si<sub>3</sub>N<sub>4</sub>, or SiC dielectric sputtering on the top of the substrate by magnetron sputtering [Kowalski, 1998]. The sputtering process creates point defects in the close to the surface layers. During the subsequent thermal annealing process those defects diffuse towards the quantum well region to promote QWI. Spatial control can be achieved using 2 μm thick layer of photoresist to protect the sample from the damage induced by sputtering. This technique allows large bandgap shifts to be obtained for range of GaAs and InP based QW material systems covering the wavelength range of 600 – 1600 nm. This technique provides an important tool for photonic integration however it compromises the final product quality because it creates significant sub-surface damage to the material. It has been demonstrated that laser diodes fabricated with this QWI technique demonstrate a threshold current 300% higher in compare to those laser diodes fabricated from as-grown material [McDougall, 1999; Franck, 2004].

### 1.3.4 Impurity Free Vacancy Disordering

Impurity-free vacancy disordering (IFVD) technique has been used to promote the disordering in QWs material system [Marsh 1993]. In order to achieve QWI by IFVD, a dielectric capping layer (e.g.  $\text{SiO}_2$ ,  $\text{Ga}_2\text{O}_3$ ,  $\text{Al}_2\text{O}_3$ ,  $\text{SrF}_2$ ,  $\text{Si}_3\text{N}_4$ ), [Boon Siew, McIlvaney et al. 1997; Dubowski, Poole et al. 1999; H H Tan 2000; H. H. Tan 2000; Liu, Qiu et al. 2000; Aimez, Beauvais et al. 2001] is deposited on the surface of a semiconductor microstructure according to a pattern demanded by the future PIC. Then, the entire sample has to be annealed in RTA processor. Elevated temperature processing starts and enhances the diffusion of atoms through the QWs interface thanks to diffusion of group III vacancies in the crystal lattice from the semiconductor's surface towards the in-depth of the microstructure. At high temperatures range (between background and processing temperatures) due to different expansion coefficients of  $\text{SiO}_2$  and GaAs or InP lattices, the high stress is generated and accumulated on the  $\text{SiO}_2/\text{GaAs}$  or  $\text{SiO}_2/\text{InP}$  interface. Since the  $\text{SiO}_2$  layer exhibits a sponge-like behaviour against the in-diffusing Ga or P atoms, it can be expected that a massive amount of these atoms can be pumped through this strongly strained interface due to difference in the thermal expansion coefficients. The  $\text{SiO}_2$  thin film deposited on GaAs in the PECVD process is already under slight tension stress at room temperature. The Ga atoms take interstitial positions in  $\text{SiO}_2$  lattice after bonds associated with As are broken. Additionally the group III atoms (e.g. Ga) have a very high diffusion rate in dielectric capping layer at high temperature, what leads to more efficient out-diffusion of group III atoms (e.g. Ga) and their significant

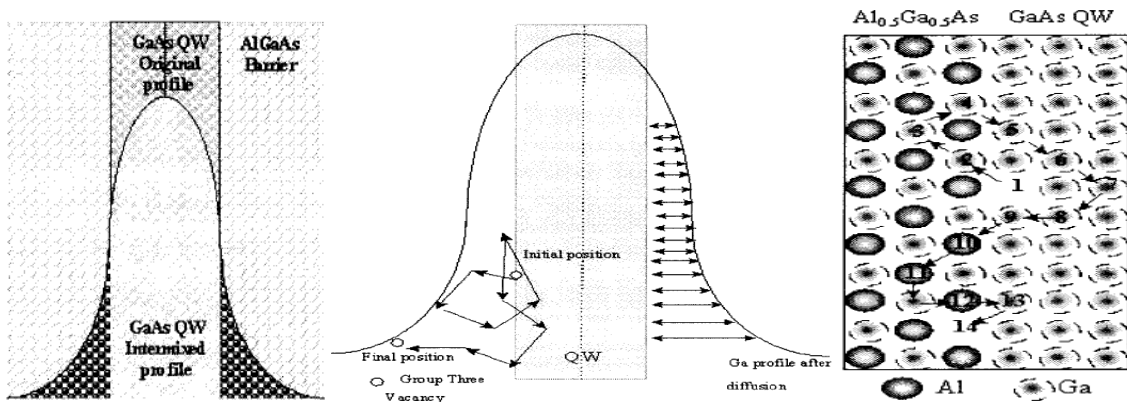
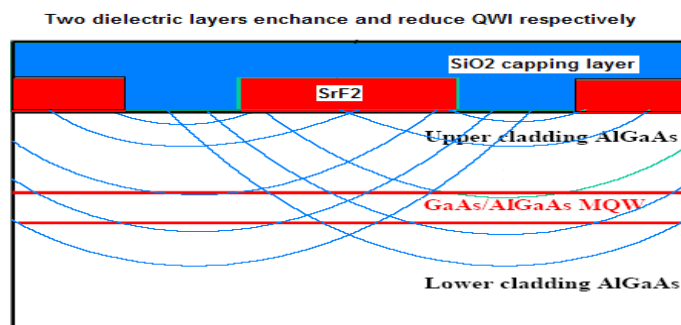


Figure 1.3.5 Schematic diagram of the lattice hops comprised in Ga out-diffusion from the QWs, and the QW interface crossings carried out by group-III vacancies during the random walks associated with their diffusion [Helmy, Aitchison et al. 1998].

presence in SiO<sub>2</sub> capping layer [Pépin 2000]. The vacancies created in the III-V compound (e.g. GaAs) diffuse rapidly sinking into the structure. When the vacancies penetrate the III-V QWs interface (e.g. AlGaAs/GaAs), QWI occurs as presented in figure 1.3.5. The shape of QWs is slightly distorted by IFVD such that the bandgap of the QWs is shifted to a higher energy state, and its refractive index is often reduced [Ralston, O'Brien et al. 1988]. This method is a very attractive tool because no impurity is introduced into the process but only vacancies, which are mostly generated by different thermal expansion coefficients of SiO<sub>2</sub> coating layer and GaAs cap, so this technique has a better chance to be controlled. The number of such created vacancies varies with the thickness of SiO<sub>2</sub> deposited layer. The speed and extent of QWI induced by IFVD can be spatially controlled by dedicated patterning with various dielectric materials. While one area of the wafer is coated with a patterned dielectric cap (e.g. SrF<sub>2</sub>, GaO<sub>3</sub>, Al<sub>2</sub>O<sub>3</sub>), which acts as the QWI inhibitor, the rest of the processed wafer is coated with SiO<sub>2</sub> or other promoting QWI capping layer [Choi 2000] as presented in figure 1.3.4. Extent of intermixing is then found to depend on the area of semiconductor's surface, which is in direct contact with the SiO<sub>2</sub> layer. Selective area intermixing across the wafer can also be obtained with the variation of thickness of the deposited or generated dielectric capping layer. The higher Al content, the greater values of PL-shift should be observed, if the sample is grown with low O content trimethylaluminum (TMA) source in MOCVD or by Molecular Beam Epitaxy [H H Tan 2000]. Complications may occur due to chemical reactions between the dielectric cap and the semiconductor that lead to the formation of native oxides and introduction of doping atoms.



**Figure 1.3.6** Schematic representation of vacancy diffusion profile in SrF<sub>2</sub> masked QW material (not to scale). The high mobility of the vacancies leads to a uniform distribution at the MQWs for patterns of a smaller dimension than the diffusion length (3µm) [Boon Siew, 1997].

This is particularly a serious problem with Al-containing semiconductor alloys, such as AlGaAs, because Al is a very effective reducing agent. So when the SiO<sub>2</sub> is in direct contact with AlGaAs, the O and Al react to form Al<sub>2</sub>O<sub>3</sub>, leaving Si so that it can diffuse through the semiconductor and cause impurity induced disordering [H H Tan 2000]. The presence of Si in the semiconductor also dopes it n-type [Epler, Burnham et al. 1986]. The O-Al reaction can be suppressed by formation of native oxide on AlGaAs surface and such a process has been used in the fabrication of lasers [Burton, Schlesinger et al. 1993]. IFVD technique may fabricate PL-shifted QWs regions as shown in (figure 1.3.5), however the lateral diffusion of vacancies generated at the surface limits its resolution, and therefore nanometer scale resolution is difficult to achieve at depths useful for guided wave optoelectronic applications [Pépin, Vieu et al. 1995]. Ga vacancies can be trapped at the SiO<sub>2</sub>/GaAs interface defects and thus become ineffective for the interdiffusion process. Also, pores in the SiO<sub>2</sub> layer can change the nature of the intermixing mechanism involved by inducing Si diffusion inside the semiconductor, presumably through reduction processes. The effect of thermal stress on V<sub>Ga</sub> creation was also observed by Cusumano et al [Cusumano, Ooi et al. 1997] who found out that phosphorous doped silica containing 5 wt% P effectively inhibited Ga-Al interdiffusion in GaAs/AlGaAs heterostructures and attributed this property to a strain relaxation effect of the cap layer during annealing. Furthermore, the kinetics of the pumping should also be affected [Cibert, Petroff et al. 1986], the larger stress difference between the film and the surface of the substrate inducing a faster out-diffusion of Ga towards SiO<sub>2</sub>. Such a behaviour was indeed observed by Katayama et al. [Katayama, Tokuda et al. 1989] in rapid thermal anneals for the same duration but at different heating rates, and they attributed this effect to the spreading and possibly

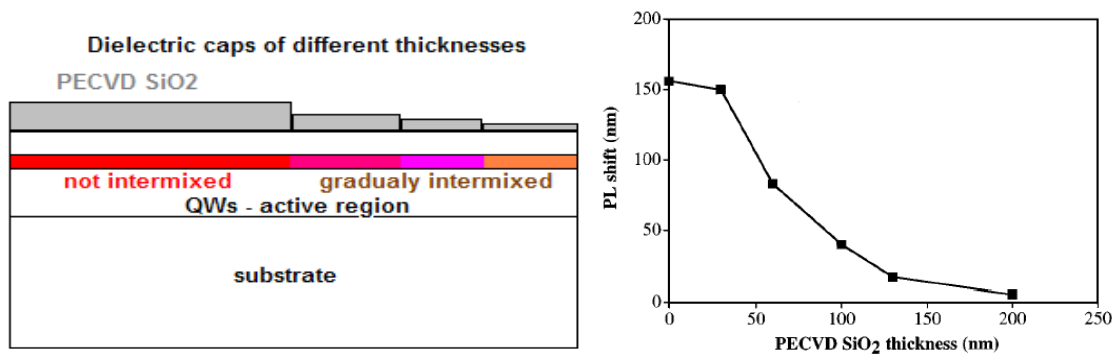


Figure 1.3.7 PL-shift as function of the thickness of PECVD SiO<sub>2</sub> protection layer [Pépin, 2000; Liu, 2000].

the cut-off of the Si-O bonds due to the larger stress, which caused an easier pass for Ga out-diffusion. This is of significant importance for laser annealing, when the heating zone is extremely small inducing high temperature gradients followed by extremely high thermal stresses induced in the SiO<sub>2</sub>, GaAs and InP lattices and mainly at the SiO<sub>2</sub>/GaAs or SiO<sub>2</sub>/InP interface.

## **1.4 Laser assisted QWI techniques**

Bandgap of MQW and QD semiconductor material can be modified at selected areas of a wafer by using intense pulsed or CW laser beams. Laser based QWI techniques are impurity-free and are relatively easy to apply for local processing. Processing with pulsed laser must be followed by thermal annealing step [Marsh, 1996; Dubowski, 1999]. However the CW laser light e.g. Nd:YAG ( $\lambda=1064$  nm) offers in-situ annealing of the processed spot that with proper control of the induced temperature and irradiation time controls the extent of QWI process precisely with high spatial and spectral resolution. Moreover, a comparative study of laser- and ion implantation- induced QWI in GaInAsP/InP microstructures demonstrated that Laser – QWI yields material with comparable, or better optical properties [Dubowski, et al. 1997]. Numerous laser based techniques discussed in literature require hot-plates for background heating of processed samples [Marsh, 1996; McKee, 1997] or rely on additional ex-situ RTA processors [Dubowski, 1999; Boon Siew, 2004; Genest, 2007].

### **1.4.1 Pulsed Laser QWI**

Pulse laser has been employed to induce QWI in both InP and GaAs QW semiconductor wafers [McKee, 1997; Qiu, 1998; Boon Siew, 2004]. Pulse laser light breaks atomic bonds in the crystal lattice by rapid and local absorption in a small volume of high energy laser radiation cumulated within tens of nanoseconds time window. This mechanism increases significantly the number of point defects in the lattice within first 30 nm in-depth layer from the irradiated semiconductor's surface depending on the irradiation wavelength and absorption of the material. During the consecutive or in-situ annealing, the created point defects migrate towards the active region of the wafer containing QWs to promote QWI process. The amplitude of the pulse laser induced QWI depends on concentration of defects and time of

applied RTA process e.g. the wavelength shift in non-irradiated InGaAs/InGaAsP sample after a total annealing time of 240s at 700 °C is only 10 nm and in comparison the exposed samples to 600 and 9000 pulses at 10 Hz repetition rate to  $\sim 5 \text{ mJ mm}^{-2}$  of Nd:YAG laser energy density were shifted by 123 and 180 nm respectively [Marsh, 1996].

### 1.4.2 Excimer laser induced QWI

Excimer lasers have been used in semiconductor wafers' microfabrication laboratories for high resolution photolithography or thin film annealing. They are attractive tools to induce QWI as they can be used to pattern wafers in numerous sites with different doses of radiation required for generation of intermixing-enhancing defects [Dubowski 2009]. Excimer laser radiation ( $\lambda=248\text{nm}$ ) is highly absorbed by III-V semiconductor material systems. Due to its optical absorption, almost all delivered power is absorbed in within the very first few atomic layers. This high concentration of photo-induced electrons leads to directly generated defects in the semiconductor lattice by various mechanisms. Therefore the RTA processing step is necessary to decrease concentration of the created defects in the structure. Direct irradiation with excimer laser radiation in room ambient environment leads to development of a  $\text{Ga}_2\text{O}_3$  oxide layer on the surface of the InGaAs/InGaAsP system, which may enhance QW photoluminescence (PL) [Dubowski, Poole et al. 1999]. It has been also demonstrated that in

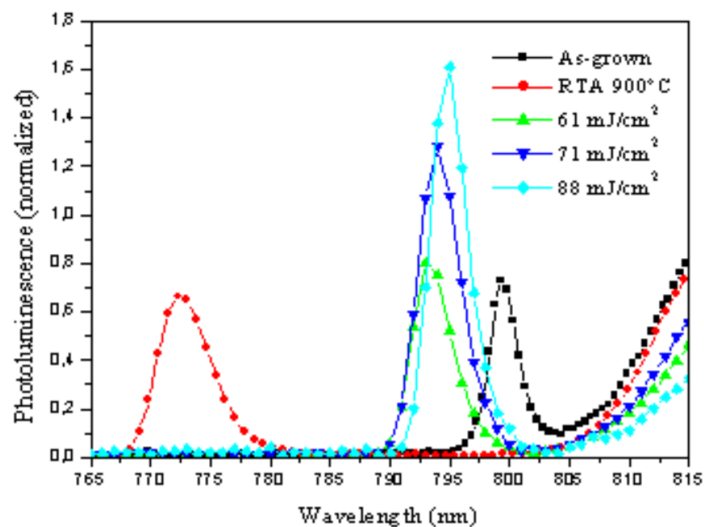
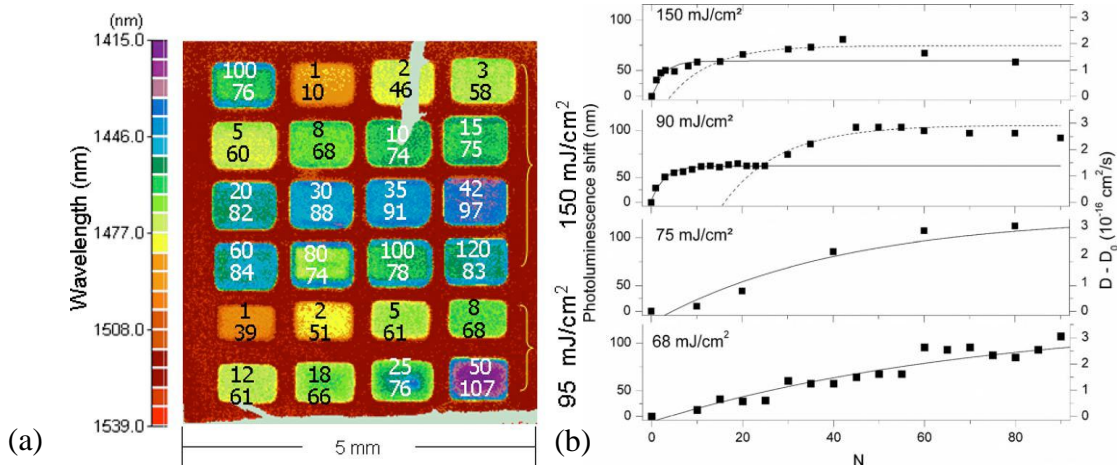


Figure 1.4.1 Low temperature photoluminescence spectra after UV laser irradiation and annealing at 900°C [Genest, Dubowski et al. 2004].



**Figure 1.4.2** PL map of ArF induced selected area intermixing (a) and dependence of the blueshift amplitude (b) [Genest, Beal et al. 2008].

GaAs based heterostructures the excimer laser radiation could inhibit QWI by growing a stressor layer that slows down the diffusion of surface point defects toward the QW region as illustrated in figure 1.4.1. [Dubowski 2003; Genest, Dubowski et al. 2004; Genest and et al. 2007]. However, the excimer laser irradiation of InP/InGaAs/InGaAsP QW microstructures in air environment generally leads to the increased intermixing rates as illustrated in figure 1.4.2 [Genest, Beal et al. 2008]. Spatial resolutions of the pulsed laser induced QWI process have been reported to be of 2.4  $\mu\text{m}$  and 1  $\mu\text{m}$  achieved with Nd:YAG ( $\lambda = 1064$  nm) [Ong 1999] and excimer ( $\lambda = 193$  nm) [Genest and et al. 2007] lasers, respectively. These characteristics make the pulsed laser QWI technique potentially attractive for nano-scale bandgap engineering, however, the quantitative description of the mechanisms involved in this process have yet to be developed.

### 1.4.3 Nd:YAG laser induced QWI

The lateral structuring of III-V QW systems with pulsed-laser-induced transient thermal gratings has been proposed by M. K. Kelly et al. in 1996 [Kelly, Nebel et al. 1996]. A QW structure grown by molecular beam epitaxy has been laterally structured with a pattern produced by the interfering beams of a high-energy pulsed  $\lambda=532$  nm laser (2nd harmonic Nd:YAG laser radiation). The resulting thermal grating produces a reduction in the carrier density and causes a lateral modulation in the band levels, with a period of 380 nm. The

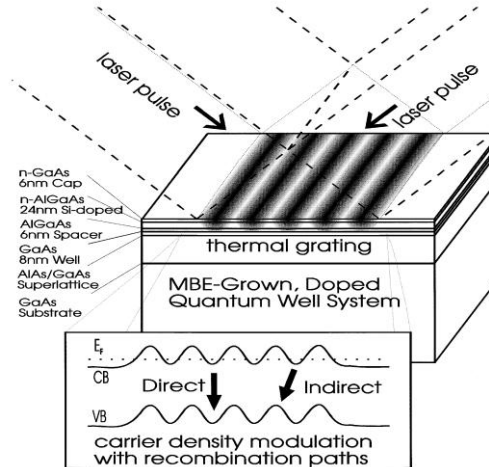


**Figure 1.4.3 Schematic diagram of the interference grating structuring of an MBE-grown QW system, and the radiative processes due to the resulting modulation [Kelly, Nebel et al. 1996].**

interference of two laser beams (split from 8mm original beam) with included angle  $\alpha$  creates a striped intensity pattern with sinusoidal profile of period  $\lambda/2 \cdot \sin(\alpha/2)$ , so periods down to half the radiation wavelength are possible. The samples were structured with two s-polarized beams at  $45^\circ$  incidence angle, overlapping to form a  $90^\circ$  included angle. Kelly et al. report that the effect of the structuring on the surface was not readily apparent to the eye with normal reflection, and the surface also appeared unchanged under a microscope, but diffracted light could be observed due to the imposed grating. The existence of the 380 nm grating could also be confirmed by cathodoluminescence microscopy, as stripes of contrasting intensity in the signal from the QW layer [Kelly, Nebel et al. 1996]. Another interesting approach for in-situ laser microprocessing of single self-assembled quantum dots and optical cavities is presented in figure 1.4.4 [Rastelli, Ulhaq et al. 2007]. A 532 nm laser beam, focused to  $1.5\mu\text{m}$  in diameter, is used in experiment for both characterisation (at low power) and for post processing (at high power) of individual InAs QD of a semiconductor sample placed in the cryostat of a micro PL setup. Although this technique works well for tuning of single QD within a micro-disk on a standing cone, its utility for processing of large size planar wafers is rather limited. This technique does not incorporate any background heating, therefore laser-irradiated areas experience high thermal stress that could lead to material damage. Also, the requirement of a cryostat inhibits the introduction of such a process to an industrial environment.



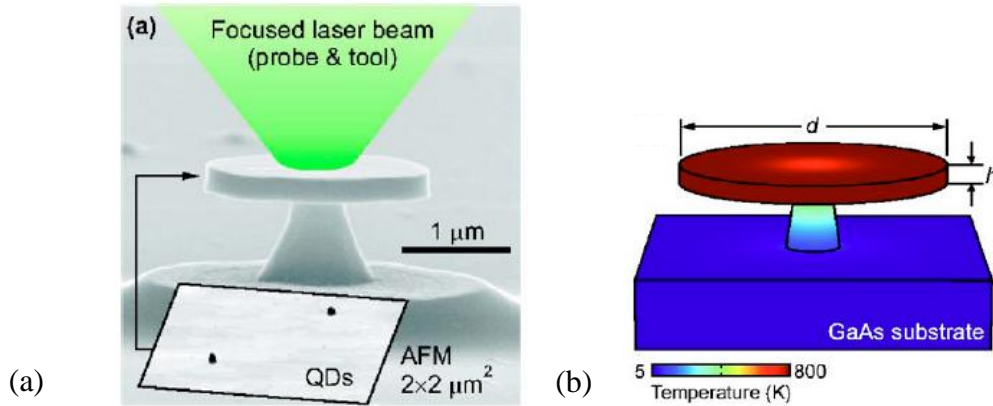


**Figure 1.4.4 (a) Scanning electron microscopy image of a GaAs micro-disk containing In(Ga)As QDs and schematic illustration of the ILP method. Inset: Atomic force microscopy image of self-assembled In(Ga)As QDs (dark in the image) with low surface density. (b) Calculated temperature profile for a micro-disc [Rastelli, Ulhaq et al.].**

The pulsed laser irradiation through a metal mask at 1064nm has also been performed and it was found that it can substantially alter the local thermal stability of the III-V material system [Marsh 1993; McKee, McLean et al. 1997]. Subsequent annealing has allowed bandgap increases by up to about 100 meV. The spatial resolution of the process was measured to be better than 25 μm, a value which was limited by the resolution of their PL system. The spatial resolution of the pulsed laser process is adequate for the realisation of photonic integrated circuits. In May 2004 Ooi et al. achieved 2.5 μm resolution of the pulsed laser induced QWI process by employing Nd:YAG laser irradiation of the InGaAs-InGaAsP microstructure through a 200 nm thick gold mask [Boon Siew, Teik Kooi et al. 2004]. The achieved QW PL peak shift was about 160 nm. To verify the capability of the QWI process for PIC fabrication of high-quality bandgap tuned lasers, two-section extended cavity lasers and multiple-wavelength laser chips were fabricated. In June 2005, the idea of selective QWI by various patterning techniques has been patented [Marsh 2005]. Marsh claims the ability of selective bandgap shifting control with multiple and sequential masking / thermal processing steps. At first the QWI – initiating material is patterned on the surface followed by the thermal processing step and then at the second step the QWI – initiating material is patterned at second regions of the surface, distinct from the first mentioned regions and conducting the second RTA step to induce blue-shift [Marsh, 2005]. During the second RTA step in the previous area there will be cumulative shift involved. It is worth pointing out that such a QWI method is

selective for the processed areas only at the first RTA step. During the next processing steps the previously shifted regions shifted again, so the process cannot deliver highly-contrasted regions of the QWI material. Simultaneous use of pulse and CW lasers has been studied for monolithic integration in InGaAs/InGaAsP MQWs structure for fabrication of the extended cavity-ridge lasers with 800  $\mu\text{m}$  long active sections and 1000  $\mu\text{m}$  long passive sections [Qiu, Bryce et al. 1998]. However, these authors employed a ceramic hotplate to raise background temperature to about 380  $^{\circ}\text{C}$  to reduce the incident CW laser power density required to heat the sample to a temperature for QWI to take place. Incorporating the hot-plate into the setup usually is not an elegant approach because of the mismatch between the processed samples' dimensions and the hot-plate area. It requires dissipation of the excessive thermal energy from the areas that are not in contact with the processed samples.

## **1.5 CW infrared Laser – RTA: One-step QWI process**

A number of QWI techniques have been proposed for spatial bandgap engineering; however, the spectral control/reproducibility of induced blueshifts at selected areas has remained to be a challenging task. First reports of CW Nd:YAG laser induced QWI, called photo-absorption induced disordering (PAID), discussed the 30-minute process involving also a hot-plate heating to maintain sample's background temperature around 220  $^{\circ}\text{C}$ . This technique has been investigated for irradiation times down to about 4 min and proved to yield material of comparable or better optical quality when compared to ion induced QWI [Dubowski, et al. 1997]. The PAID technique has been employed to modify the bandgap of the InGaAs/InGaAsP MQWs material to be useful in the fabrication of monolithically integrated lasers, modulators, and passive waveguides [McKee, McLean et al. 1997]. It is important to note that bandgap tuning procedure reported by McKee was not spatially selective. The steady Nd:YAG laser beam spot has been projected on the surface of the processed microstructure which resulted in a maximum of 110 nm blueshift in the middle of the laser spot and gradual decrease of blueshift towards the as-grown material on  $\sim 400$   $\mu\text{m}$  distance [Qiu, 1998]. After the laser irradiation and PL map analysis, a series of extended cavity lasers were fabricated from arbitrarily chosen areas from gradually intermixed transition region between fully intermixed and as-grown material [Qiu, 1998]. The maskless CW Nd:YAG laser

writing of the InP/InGaAsP QW microstructure with speed of 20  $\mu\text{m/s}$  and triple pass of the 7.5  $\text{W/mm}^2$  laser beam yield the 90 nm blue-shifted material. The achieved resolution of the process was 400  $\mu\text{m}$ , which was about half of the processing laser beam radius [Dubowski, 1998]. In 1999, the CW Nd:YAG laser scanning technique was utilized for fabrication of semiconductor laser array by laser-induced QWI by J.J. Dubowski et al. [Dubowski 1999]. Bars with arrays of broad area lasers, having lengths from 300 to 600  $\mu\text{m}$ , were fabricated. An individual bar (2 to 3 mm long) included lasers operate typically between 1.4 and 1.5  $\mu\text{m}$ . The lasers showed stable threshold current density and quantum efficiency as function of the operating wavelength. In 2000, the Nd:YAG laser has been used for annealing of InAs/GaAs quantum-dot (QD) microstructures for selective area tuning of their electronic shell structure [Dubowski, Allen et al. 2000]. After 20-40 s of laser irradiation in the most extreme case, the shift of the ground state transition of 298 meV was achieved. Authors claim the usefulness of this method for fabrication of advanced microstructures, such as photonics band gap crystals, which could be monolithically integrated with the same semiconductor chip. Dubowski et al. [Dubowski, Feng et al. 2002] have investigated the maskless and selective area CW Nd:YAG laser annealing of III-V QW structures as a possible route towards the fabrication of monolithically integrated photonic circuits. The successful fabrication of multiple wavelength ridge waveguide lasers array has been reported. The investigated structure was composed of five (6-nm-thick) QWs separated by barriers (19nm thick). The 200-nm-thick layer of  $\text{SiO}_2$  was deposited on both sides to protect the material from decomposition during laser irradiation. The processing Nd:YAG ( $\lambda=1064\text{nm}$ ) laser beam of diameter about 3 mm delivered power density of 0.5  $\text{W/mm}^2$ . The monitored temperature of the sample was about 800°C (InGaAs/InGaAsP material system), and the annealing time was 20s. The bandgap of the intermixed material was gradually blue-shifted over a distance of about 2.5 mm along the longer axis of the sample from 1405 nm in the center of the laser irradiated zone, to about 1520nm, which corresponds to the bandgap of the as-grown material. The preliminary results for GaAs/AlGaAs system indicate the feasibility of the Nd:YAG laser annealing for fabricating 40 nm blueshift of the QW PL peak from 832 nm down to 792 nm for linear arrays of IR photodetectors [Dubowski, Song et al. 2004]. An array of 0.8 mm period lines of the band gap shifted material has been written by fast scanning a slightly focused laser beam for the total exposure time of 80 s. The amplitude of the periodically oscillating blueshift was only

10 nm, but authors note that reducing the spot size of the laser-writing beam and introducing back heating of the sample could further increase this amplitude. It remains to be demonstrated to what extent the modified properties of the processed GaAs/AlGaAs QW intermixed photodetector (QWIP) microstructure could be offset by the gain in the increased functionality and integration level of the device fabricated from such material.

The spatially selective IR laser-based semiconductor bandgap engineering showed potential for fabrication and tuning of optical devices on a single substrate and in such a way optimize the performance of fabricated elements of an optical circuit. Carefully prepared design and control of the process would allow for the fabrication of PICs with high reproducibility. Further studies were necessary to fully take advantage of the CW IR laser induced QWI phenomena for development of new devices, e.g., for telecommunication or biomedical applications. To control spectral modification of the band edge across the wafer with better spectral resolution than  $\pm 1$  nm, it is necessary to use one step QWI technique with minimum number of parameters to control. Such a one step QWI technique can be then applied in the iterative manner to perform fine tuning towards the desired emission wavelength. The two major parameters to control are the temperature and time of the annealing process. To this date, no laser-based technique for selective area tuning of emission wavelength in industrial size quantum semiconductor (QS) wafers has been proposed. Development of such a tuning technique would allow the fabrication of monolithically integrated photonic circuits with high yield. This idea was one of the driving forces behind the research undertaken in the frame of this thesis. In the following chapters, I discuss the results of QWI achieved with two-laser RTA technique developed in frame of this thesis. A ceramic hotplate has been replaced with a 980 nm high power laser diode, which allowed to increase easily and rapidly the background temperatures required for carrying out the QWI process without damaging the samples. During the disordering process, the material to be processed is coated with a layer of plasma-deposited silicon dioxide of about 266 nm, which acts both as an anti-reflection coating and as a protective layer against surface reactions with the atmosphere.

---

## Bibliography

- Aimez, V., J. Beauvais, et al. (2002). "Low-energy ion-implantation-induced quantum-well intermixing." Selected Topics in Quantum Electronics, IEEE Journal of **8**(4): 870-879.
- Aimez, V., J. Beauvais, et al. (2001). "Monolithic intracavity laser-modulator device fabrication using postgrowth processing of 1.55  $\mu$  m heterostructures." Applied Physics Letters **79**(22): 3582-3584.
- Aspnes, D. E. and A. A. Studna (1983). "Dielectric functions and optical parameters of Si, Ge, GaP, GaAs, GaSb, InP, InAs, and InSb from 1.5 to 6.0 eV." Physical Review B **27**(2): 985.
- Beaudoin, M., A. J. G. DeVries, et al. (1997). "Optical absorption edge of semi-insulating GaAs and InP at high temperatures." Applied Physics Letters **70**(26): 3540-3542.
- Boon Siew, O., K. McIlvaney, et al. (1997). "Selective quantum-well intermixing in GaAs-AlGaAs structures using impurity-free vacancy diffusion." Quantum Electronics, IEEE Journal of **33**(10): 1784-1793.
- Boon Siew, O., O. Teik Kooi, et al. (2004). "Multiple-wavelength integration in InGaAs-InGaAsP structures using pulsed laser irradiation-induced quantum-well intermixing." Quantum Electronics, IEEE Journal of **40**(5): 481-490.
- Brunner, K., G. Abstreiter, et al. (1992). "Optical characterization of GaAs/AlGaAs nanostructures fabricated by focussed laser beam induced thermal interdiffusion." Surface Science **267**(1-3): 218-222.
- Brunner, K., U. Bockelmann, et al. (1992). "Photoluminescence from a single GaAs/AlGaAs quantum dot." Physical Review Letters **69**(22): 3216.
- Bugajski, M. and W. Lewandowski (1985). "Concentration-dependent absorption and photoluminescence of n-type InP." Journal of Applied Physics **57**(2): 521-530.
- Burkhard, H., H. W. Dinges, et al. (1982). "Optical properties of In<sub>1-x</sub>Ga<sub>x</sub>P<sub>1-y</sub>As<sub>y</sub>, InP, GaAs, and GaP determined by ellipsometry." Journal of Applied Physics **53**(1): 655-662.
- Burton, R. S., T. E. Schlesinger, et al. (1993). "High-performance diffusion disordered Al<sub>x</sub>Ga<sub>1-x</sub>As lasers via a self-aligned process and conventional open-tube annealing." Journal of Applied Physics **73**(4): 2015-2018.
- Casey, J. H. C., D. D. Sell, et al. (1975). "Concentration dependence of the absorption coefficient for n- and p - type GaAs between 1.3 and 1.6 eV." Journal of Applied Physics **46**(1): 250-257.
- Choi, W. J. (2000). Dependence of Dielectric Cap Quantum Well Disorder on the Characteristics of Dielectric Capping Film. Semiconductor Quantum Well Intermixing. E. H. Li. Amsterdam, Gordon and Breach. **8**.
- Cibert, J., P. M. Petroff, et al. (1986). "Kinetics of implantation enhanced interdiffusion of Ga and Al at GaAs-Ga<sub>x</sub>Al<sub>1-x</sub>As interfaces." Applied Physics Letters **49**(4): 223-225.
- COMSOL, I. COMSOL. Burlington.
- Cusumano, P., B. S. Ooi, et al. (1997). "Suppression of quantum well intermixing in GaAs/AlGaAs laser structures using phosphorus-doped SiO<sub>2</sub> encapsulant layer." Journal of Applied Physics **81**(5): 2445-2447.
- Dubowski, #160, et al. (1997). "A comparative study of laser- and ion implantation-induced quantum well intermixing in GaInAsP/InP microstructures." **2991**: IX, 294 p.

- Dubowski, J. J. (1999). "Semiconductor laser array fabricated by Nd:YAG laser-induced quantum well intermixing." Proc. of SPIE **1618**: 191.
- Dubowski, J. J. (2003). Laser-induced bandgap shifting for photonic device integration. USA. **6,670,644**.
- Dubowski, J. J. (2009). Laser-based Bandgap Engineering of Quantum Semiconductor Wafers.
- Dubowski, J. J., C. N. Allen, et al. (2000). "Laser-induced InAs/GaAs quantum dot intermixing." Applied Physics Letters **77**(22): 3583-3585.
- Dubowski, J. J., Y. Feng, et al. (2002). "Monolithic multiple wavelength ridge waveguide laser array fabricated by Nd:YAG laser-induced quantum well intermixing." Journal of Vacuum Science & Technology A: Vacuum, Surfaces, and Films **20**(4): 1426-1429.
- Dubowski, J. J., P. J. Poole, et al. (1999). "Enhanced quantum-well photoluminescence in InGaAs/InGaAsP heterostructures following excimer-laser-assisted surface processing." Applied Physics A: Materials Science & Processing **69**(0): S299-S303.
- Dubowski, J. J., C. Y. Song, et al. (2004). "Laser-induced selective area tuning of GaAs/AlGaAs quantum well microstructures for two-color IR detector operation." Journal of Vacuum Science & Technology A: Vacuum, Surfaces, and Films **22**(3): 887-890.
- Epler, J. E., R. D. Burnham, et al. (1986). "Laser induced disordering of GaAs-AlGaAs superlattice and incorporation of Si impurity." Applied Physics Letters **49**(21): 1447-1449.
- Fleming, R. M., D. B. McWhan, et al. (1980). "X-ray diffraction study of interdiffusion and growth in (GaAs)<sub>n</sub>(AlAs)<sub>m</sub> multilayers." Journal of Applied Physics **51**(1): 357-363.
- Genest, J., R. Beal, et al. (2008). "ArF laser-based quantum well intermixing in InGaAs/InGaAsP heterostructures." Applied Physics Letters **93**(7): 071106-3.
- Genest, J., J. J. Dubowski, et al. (2004). UV-laser-based process for quantum well intermixing of III-V heterostructures. Integrated Optics and Photonic Integrated Circuits, Strasbourg, France, SPIE.
- Genest, J. and et al. (2007). "UV laser controlled quantum well intermixing in InAlGaAs/GaAs heterostructures." Journal of Physics: Conference Series **59**(1): 605.
- Glassbrenner, C. J. and G. A. Slack (1964). "Thermal Conductivity of Silicon and Germanium from 3°K to the Melting Point." Physical Review **134**(4A): A1058.
- H H Tan, S. Y., M. Gal, and C. Jagadish (2000). Optoelectronic properties of semiconductors and superlattices. Semiconductor Quantum Well Intermixing. E. H. Li. Amsterdam, Gordon and Breach. **8**.
- H. H. Tan, S. Y., M. Gal, and C. Jagadish (2000). Optoelectronic properties of semiconductors and superlattices. Semiconductor Quantum Well Intermixing. E. H. Li. Amsterdam, Gordon and Breach: 307.
- Helmy, A. S., J. S. Aitchison, et al. (1998). "Quantitative model for the kinetics of compositional intermixing in GaAs-AlGaAs quantum-confined heterostructures." Selected Topics in Quantum Electronics, IEEE Journal of **4**(4): 653-660.
- Hirayama, Y., S. Tarucha, et al. (1988). "Fabrication of a GaAs quantum-well-wire structure by Ga focused-ion-beam implantation and its optical properties." Physical Review B **37**(5): 2774.
- Holonyak, N. (1981). "IR-red GaAs-AlAs superlattice laser monolithically integrated in a yellow-gap cavity." Appl. Phys. Lett. **39**: 102.

- Holonyak, N., Jr. (1998). "Impurity-induced layer disordering of quantum-well heterostructures: discovery and prospects." Selected Topics in Quantum Electronics, IEEE Journal of **4**(4): 584-594.
- Ioffe, O.-T. I. from <http://www.ioffe.rssi.ru/SVA/NSM/Semicond>.
- Jagadish, H. H. T. Y. G. (2000). Semiconductor Quantum Well Intermixing. Amsterdam.
- Jellison, J. G. E. and F. A. Modine (1982). "Optical absorption of silicon between 1.6 and 4.7 eV at elevated temperatures." Applied Physics Letters **41**(2): 180-182.
- Johnson, S. R. and T. Tiedje (1995). "Temperature dependence of the Urbach edge in GaAs." Journal of Applied Physics **78**(9): 5609-5613.
- Kapon, E., N. G. Stoffel, et al. (1988). "BIREFRINGENT CHANNEL WAVE-GUIDES DEFINED BY IMPURITY-INDUCED SUPERLATTICE DISORDERING." Applied Physics Letters **52**(5): 351-353.
- Katayama, M., Y. Tokuda, et al. (1989). "X-ray photoelectron spectroscopic study of rapid thermal processing on SiO<sub>2</sub>/GaAs." Applied Physics Letters **54**(25): 2559-2561.
- Kelly, M. K., C. E. Nebel, et al. (1996). "Lateral structuring of III-V quantum well systems with pulsed-laser-induced transient thermal gratings." Applied Physics Letters **68**(14): 1984-1986.
- Laruelle, F., A. Bagchi, et al. (1990). "Focused ion beam channeling effects and ultimate sizes of GaAlAs/GaAs nanostructures." Applied Physics Letters **56**(16): 1561-1563.
- Liu, X. F., B. C. Qiu, et al. (2000). "Control of multiple bandgap shifts in InGaAs-AlInGaAs multiple-quantum-well material using different thicknesses of PECVD SiO<sub>2</sub> protection layers." Photonics Technology Letters, IEEE **12**(9): 1141-1143.
- Macfarlane, G. G., T. P. McLean, et al. (1959). "Exciton and phonon effects in the absorption spectra of germanium and silicon." Journal of Physics and Chemistry of Solids **8**: 388-392.
- Marsh, J. H. (1993). "Quantum well intermixing." Semiconductor Science and Technology(6): 1136.
- Marsh, J. H. (2000). Impurity-Free Vacancy Disordering of GaAs/AlGaAs Quantum Well Structures. Semiconductor Quantum Well Intermixing. E. H. Li. Amsterdam, Gordon and Breach. **8**.
- Marsh, J. H. (2005). Multiple anneal induced disordering. **WO/2005/057638**.
- Marsh, J. H., S. I. Hansen, et al. (1991). "Applications of neutral impurity disordering in fabricating low-loss optical waveguides and integrated waveguide devices." Optical and Quantum Electronics **23**(7): S941-S957.
- McKee, A., C. McLean, et al. (1997). "Monolithic integration in InGaAs-InGaAsP multiple-quantum-well structures using laser intermixing." IEEE Journal of Quantum Electronics **33**(1): 45-55.
- Miller, S. E. (1969). "Integrated optics: an introduction." Bell Syst. Tech. J. **48**: 205969.
- Nie, D., T. Mei, et al. (2006). "Argon plasma exposure enhanced intermixing in an undoped InGaAsP/InP quantum-well structure." Journal of Applied Physics **100**(4): 046103-3.
- O. C. Zienkiewicz, R. L. T. (1996). The Finite Element Method. San Diego, Academic Press.
- Oleksandr Voznyy, R. S., Jan J. Dubowski (2006). "Multibandgap quantum well wafers by IR laser quantum well intermixing: simulation of the lateral resolution of the process." JLMN-Journal of Laser Micro/Nanoengineering **1**(1): 48-53.

- Ong, T. K. (1999). High spatial resolution quantum well intermixing process in GaInAs/GaInAsP laser structures. rd Pacific Rim conference on lasers and electro-optics. C. P. Rim'99. Seoul, Korea: 193.
- Palankovski, V., R. Schultheis, et al. (2001). "Simulation of power heterojunction bipolar transistors on gallium arsenide." Electron Devices, IEEE Transactions on **48**(6): 1264-1269.
- Pépin (2000). Selective Interdiffusion of GaAs/AlGaAs Quantum Wells through SiO<sub>2</sub> Encapsulation - Comparison with the Ion Implantation Approach. Semiconductor Quantum Well Intermixing. E. H. Li. Amsterdam, Gordon and Breach. **8**.
- Pépin, A., C. Vieu, et al. (1995). "Fabrication of quantum wires by selective intermixing induced in GaAs/AlGaAs quantum well heterostructures by SiO<sub>2</sub> capping and subsequent annealing." Superlattices and Microstructures **18**(3): 229-229.
- Petroff, P. M. (1977). "Transmission electron microscopy of interfaces in III-V compound semiconductors." Journal of Vacuum Science and Technology **14**(4): 973-978.
- Petroff, P. M., Y. J. Li, et al. (1991). "Nanostructures processing by focused ion beam implantation." Journal of Vacuum Science & Technology B: Microelectronics and Nanometer Structures **9**(6): 3074-3078.
- Prins, F. E., G. Lehr, et al. (1993). "Intermixed GaAs/AlGaAs quantum wires and the influence of implantation species on the steepness of the lateral potential." Journal of Applied Physics **73**(5): 2376-2380.
- Qiu, B. C., A. C. Bryce, et al. (1998). "Monolithic integration in InGaAs-InGaAsP multi-quantum-well structure using laser processing." Photonics Technology Letters, IEEE **10**(6): 769-771.
- Radoslaw Stanowski, O. V., Jan J. Dubowski (2006). "Finite element model calculations of temperature profiles in Nd:YAG laser annealed GaAs/AlGaAs quantum well microstructures." JLMN-Journal of Laser Micro/Nanoengineering **1**(1): 17-22.
- Ralston, J., G. W. Wicks, et al. (1986). "DEFECT STRUCTURE AND INTERMIXING OF ION-IMPLANTED ALXGA1-XAS/GAAS SUPERLATTICES." Journal of Applied Physics **59**(1): 120-123.
- Ralston, J. D., S. O'Brien, et al. (1988). "Room-temperature exciton transitions in partially intermixed GaAs/AlGaAs superlattices." Applied Physics Letters **52**(18): 1511-1513.
- Rastelli, A., A. Ulhaq, et al. (2007). "In situ laser microprocessing of single self-assembled quantum dots and optical microcavities." Applied Physics Letters **90**(7): 073120-3.
- Ravindra, N. M., S. Abedrabbo, et al. (1998). "Temperature-dependent emissivity of silicon-related materials and structures." Semiconductor Manufacturing, IEEE Transactions on **11**(1): 30-39.
- Ravindra, N. M., P. Ganapathy, et al. (2007). "Energy gap-refractive index relations in semiconductors - An overview." Infrared Physics & Technology **50**(1): 21-29.
- Stanowski, R., S. Bouaziz, et al. (2008). Selective area bandgap engineering of InGaAsP/InP quantum well microstructures with an infrared laser rapid thermal annealing technique. Photon Processing in Microelectronics and Photonics VII, San Jose, CA, USA, SPIE.
- Stanowski, R. and J. J. Dubowski (2009). "Laser rapid thermal annealing of quantum semiconductor wafers: a one step bandgap engineering technique." Applied Physics A-Materials Science & Processing **94**(3): 667-674.
- Stanowski, R., M. Martin, et al. (2009). "Iterative bandgap engineering at selected areas of quantum semiconductor wafers." Optics Express **17**(22): 19842-19847.



- Stanowski, R., Voznyy O., Dubowski J.J. (2005). Modelling of temperature profiles in Nd:YAG laser annealed GaAs/AlGaAs quantum well microstructures. Laser Applications in Microelectronic and Optoelectronic Manufacturing X. San Jose, SPIE.
- Stanowski, V., Dubowski (2006). "Finite element model calculations of temperature profiles in Nd:YAG laser annealed GaAs/AlGaAs quantum well microstructures." JLMN-Journal of Laser Micro/Nanoengineering **1**(1): 17-22.
- Steen, M. W. (1998). Laser Material Processing. Berlin, Springer.
- Sturge, M. D. (1962). "Optical Absorption of Gallium Arsenide between 0.6 and 2.75 eV." Physical Review **127**(3): 768.
- Sze, S. M. (1981). Physics of Semiconductor Devices. New York, Wiley.
- TIEMEIJER, J. J. M. B. P. J. A. T. T. v. D. E. J. J. A. A. M. T. S. G. N. v. d. H. L. F. (1997). "Characterization of Butt-Joint InGaAsP Waveguides and Their Application to 1310 nm DBR-Type MQW Gain-Clamped Semiconductor Optical Amplifiers." IEICE TRANSACTIONS on Electronics **E80-C**(5): 675.
- Timans, P. J. (1992). "The experimental determination of the temperature dependence of the total emissivity of GaAs using a new temperature measurement technique." Journal of Applied Physics **72**(2): 660-670.
- Trivedi, D. A. and N. G. Anderson (1996). "Modeling the near-gap refractive index properties of semiconductor multiple quantum wells and superlattices." Selected Topics in Quantum Electronics, IEEE Journal of **2**(2): 197-209.
- Turner, W. J., W. E. Reese, et al. (1964). "Exciton Absorption and Emission in InP." Physical Review **136**(5A): A1467.
- Vieu, C., M. Schneider, et al. (1991). "Optical characterization of selectively intermixed GaAs/GaAlAs quantum wires by Ga[<sup>sup</sup> + ] masked implantation." Journal of Applied Physics **70**(3): 1444-1450.
- Voznyy, S., Dubowski (2006). "Multibandgap quantum well wafers by IR laser quantum well intermixing: simulation of the lateral resolution of the process." JLMN-Journal of Laser Micro/Nanoengineering **1**(1): 48-53.
- Wallin, J., G. Landgren, et al. (1992). "Selective area regrowth of butt-joint coupled waveguides in multi-section DBR lasers." Journal of Crystal Growth **124**(1-4): 741-746.

## **Chapter 2**

# **Process design for CW IR Laser – RTA of QS wafers**

In this chapter I discuss the results of calculated temporal temperature profiles induced with CW IR laser in GaAs and InP based QS wafers. The calculations are based on 3D finite element method (FEM) and take into account semiconductor wafer parameters such heat conductivity, emissivity and optical absorption as well as the operating lasers beams parameters such as wavelength and energy intensity distribution profiles.

### **2.1 Selective area heat generation in Si, GaAs and InP wafers induced with CW 980 and 1064 nm laser beams**

Control of selective area QWI process induced with both CW  $\lambda=980$  nm and  $\lambda=1064$  nm laser beams requires good understanding of the laser radiation induced heat generation mechanisms within the irradiated semiconductor crystal. Although the laser beam parameters remain constant during the irradiation process, the parameters of the irradiated material change significantly in the range of 23 up to 1000 °C. Therefore, to properly design the Laser – RTA processing technique, I have performed modeling of the temporal temperature profiles behaviour using the commercially available 3D FEM solver [COMSOL] taking into account temperature dependent heat conductivity, emissivity and optical absorption coefficients. Other material parameters, such as density and heat capacity were assumed temperature independent. In this chapter, I discuss temperature profiles in GaAs and InP based QW wafers induced with both stationary CW GaAs/AlGaAs laser diode ( $\lambda=980$  nm) and stationary or moving CW Nd:YAG ( $\lambda=1064$  nm) laser beams.

### 2.1.1 Photon's energies at 980 and 1064 nm wavelengths

The employed lasers photons' energies correspond to theirs represented radiation wavelengths according to the Max Planck's equation 2.1:

$$E = h\nu = \frac{hc}{\lambda} \quad (2.1)$$

where  $h$  = Planck's constant =  $6.63 \cdot 10^{-34} \text{ J} \cdot \text{s}$

$c$  = speed of light =  $2.99 \cdot 10^8 \frac{\text{m}}{\text{s}}$  ;  $\lambda$  = represented light wavelength

$$E_{980nm} = h\nu = \frac{hc}{\lambda} = 2.026 \cdot 10^{-19} \text{ J} = 1.265 \text{ eV}$$

$$E_{1064nm} = h\nu = \frac{hc}{\lambda} = 1.866 \cdot 10^{-19} \text{ J} = 1.165 \text{ eV}$$

### 2.1.2 Laser light interaction with the semiconductor wafer microstructure

The incident laser light radiation on the semiconductor material surface might be reflected, absorbed or transmitted as presented in figure 2.1.1.

$$I = R + A + T \quad (2.2)$$

$I$  – incident beam power density [ $\text{J}/\text{cm}^2$ ];  $R$  – reflected power density [ $\text{J}/\text{cm}^2$ ];  
 $A$  – absorbed power density [ $\text{J}/\text{cm}^2$ ];  $T$  – transmitted power density [ $\text{J}/\text{cm}^2$ ].

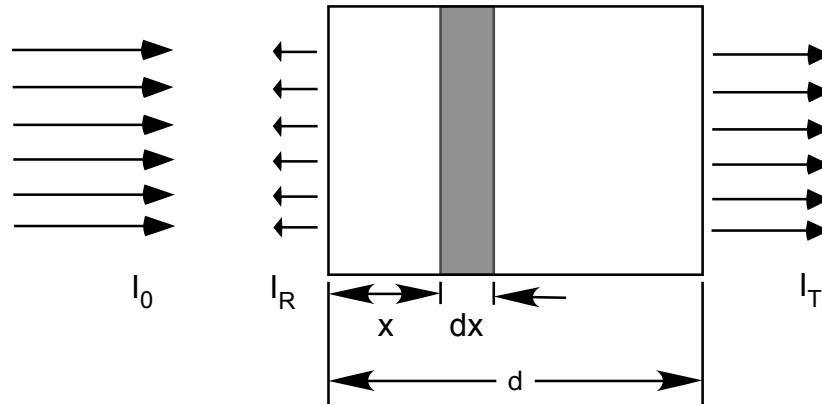


**Figure 2.1.1 Absorption of light in a semiconductor material**

Reflection coefficient  $R = I_R/I_0$ , describes the percentage of the reflected light intensity  $I_R$

Therefore the incident part is:

$$I(0) = I_0 - I_R = I_0(1 - R). \quad (2.3)$$

The intensity 'I' of light passing through the layer of thickness 'dx' will be decreased by 'dI' due to absorption of this layer.

$$dI = -\alpha \cdot I \cdot dx \quad (2.4)$$

The coefficient ' $\alpha$ ' describes the proportion between the light's intensity 'I' decrease to the thickness of the layer 'dx'.

Solving the integral:

$$\int_{I(0)}^{I(x)} \frac{dI}{I} = -\int_0^x \alpha \cdot dx \quad (2.5)$$

leads to the Beer-Lambert equation:

$$I = I_0 \cdot (1 - R) \cdot \exp(-\alpha \cdot x) \quad (2.6)$$

which describes the change of 'I' intensity of light after passing through a layer of thickness 'x'.

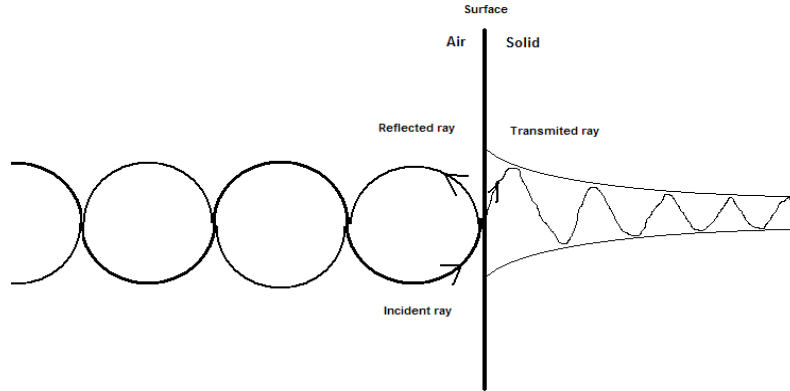


**Figure 2.1.2 The schematic of incident laser beam on the semiconductor surface [Steen 1998]**

The intensity 'I' of light is proportional to the square of electromagnetic wave vector amplitude  $E^2$ . Therefore it is possible to describe absorption with E:

$$E(r, t) = E(0) \exp[-i(\vec{k} \cdot \vec{r} - \omega t)], \quad (2.7)$$

where  $\vec{k} = \frac{2\pi}{\lambda}$  - wave vector parallel to the direction of wave propagation;

$\vec{r}$  - is a point radius vector;  $\lambda$  - wavelength of the incident radiation.

The wave phase velocity  $v_f = \frac{r}{t} = \frac{\omega}{k}$  equals  $v_f = \frac{c}{n}$ .

The semiconductor wafer material is characterized by complex index of refraction:

$$N = n - i\kappa; \quad n = \frac{c}{v}$$

where:  $\kappa$  - extinction coefficient responsible for material's absorption (figure 2.1.2),  
 $c$  - speed of light

Therefore :

$$E(x, t) = E(0) \exp[-i\omega(n \cdot \frac{x}{c} - t) - \omega\kappa \frac{x}{c}]$$

$$E(x)^2 = E(0)^2 \exp[-2\omega\kappa \frac{x}{c}]$$

$$I(x) = I(0) \exp[-\alpha x]$$

where  $\alpha = \frac{2\omega\kappa}{c} = 4\pi\kappa / \lambda$ . This equation combines the absorption coefficient with extinction coefficient and the incident radiation wavelength.

### 2.1.3 Absorption of laser light radiation by Si, GaAs and InP wafers.

Semiconductor crystals absorb most efficiently photons that carry energies greater than energy bandgap and sufficient to excite electrons from the valence band to the conduction band. Semiconductor crystals have direct or in-direct energy bandgap as presented in the figure 2.1.3.

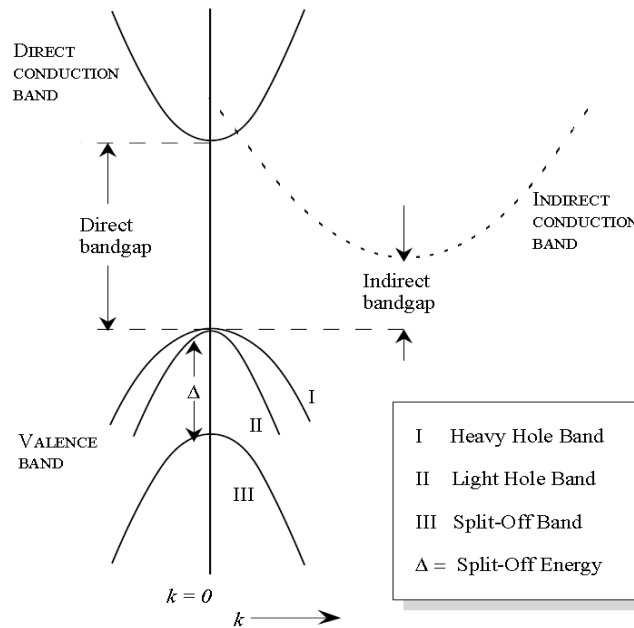


**Figure 2.1.3 Schematic of the valence band, direct and indirect bandgap conduction bands. The curves I, II and III in the valence band are called heavy hole, light hole, and split-off hole states respectively [Singh, 2000].**

When the maximum of the valence band and minimum of the conduction band are at the same point of the Brillouin zone, e.g., at  $k=0$ , the semiconductor has a direct energy bandgap as presented in figure 2.1.3 (solid lines). Direct electron transitions take place with the conservation of the wave vector. Consequently, when the minimum of the conduction band is shifted in the Brillouin zone against the maximum of the valence band, the semiconductor has an indirect energy bandgap for  $k>0$  as presented in figure 2.1.3 (dashed line). In this case, the photon absorption leads to the excitation of an electron from the valence band to the conduction accompanied with a change of its momentum. The electron later interacts with a vibration of a lattice, which results in a further change in the momentum of the electron

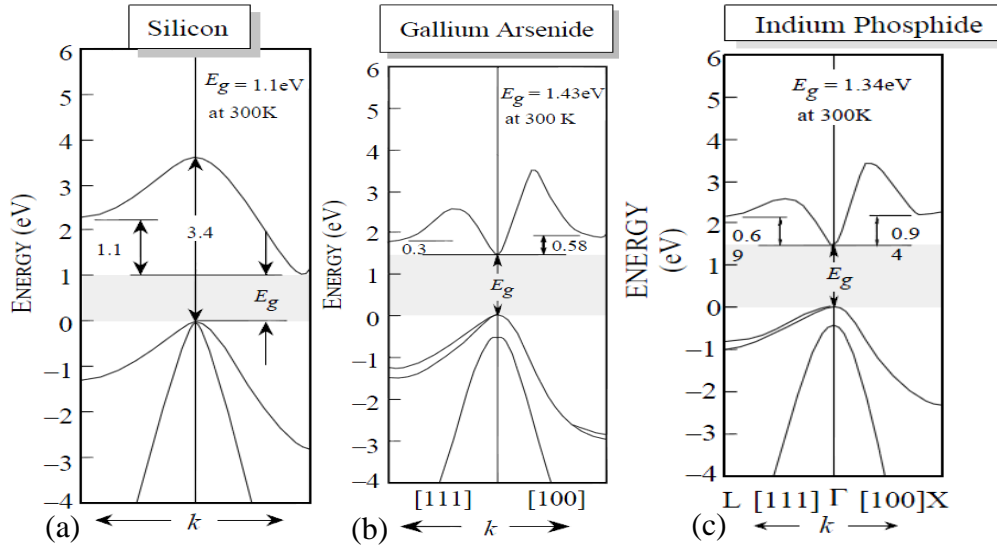


**Figure 2.1.4** Schematic of the indirect energy bandgap for Si (a) and the direct energy bandgaps of GaAs (b) and InP (c) [Singh, 2000].

and the wave vector of the lattice vibration (phonon). The GaAs and InP crystals have direct energy bandgaps while the Si crystal has an indirect energy bandgap, as presented in figure 2.1.4. There are multiple effects responsible for the perturbation of the regularity of a semiconductor's crystal lattice, which leads to local variation of the energy bandgap. Therefore photons of energies smaller than the semiconductor's energy bandgap might be also weakly absorbed. Energy bands deformation might stem from inherent elastic deformations (tensile or compressive) of the crystal lattice as presented in figure 2.1.5 (a) or electrostatically caused by interior electric fields as presented in figure 2.1.5 (b). In both cases, absorption of photons of  $\hbar\omega < E_g$  is possible. Elastic deformations locally shrink the  $E_g$ . The electrostatic deformations allow optical transitions through tunnelling effects. This phenomenon is called the Franz-Keldysh effect. Another mechanism of light absorption takes advantage of 2-stage transitions with participation of shallow donors or acceptors inter-bandgap energy levels as presented in figure 2.1.6 (a).

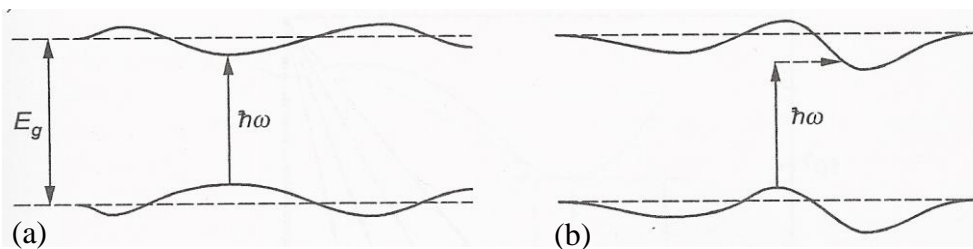


**Figure 2.1.5** Energy badgap deformation: elastic (a) and electrostatic (b) [Bacewicz 1995].

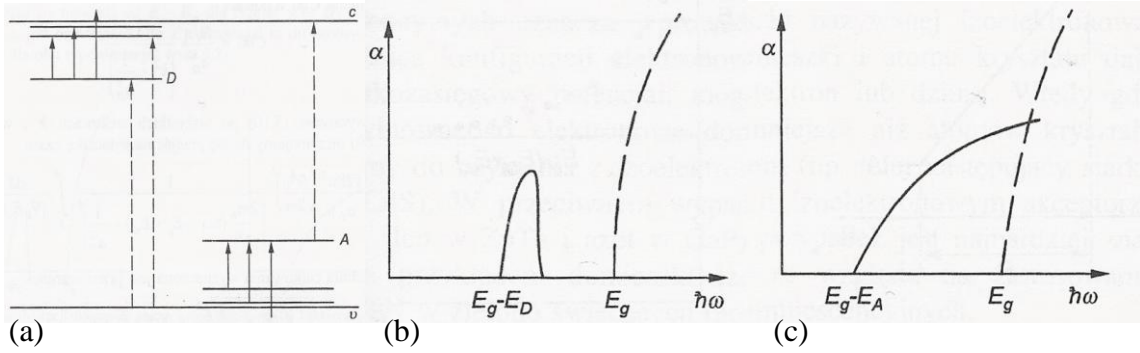


**Figure 2.1.6 Optical transitions with participation of shallow donors (a) Absorption spectra for donors (b) and acceptors (c). Dashed line on (b) and (c) corresponds to interband absorption [Bacewicz 1995].**

The first stage relies on photo-ionization of a donor or acceptor. The second stage involves an optical transition between the dopant energy level and the opposite band level: donor – valence band and acceptor – conduction band. These absorption mechanisms become apparent close to the absorption edge as presented in figure 2.1.6 (b) and (c). Semiconductor materials that contain both types of dopants may demonstrate the acceptor - donor absorption mechanism presented in figure 2.1.7 (a). This mechanism is described by eq. 2.8 [Bacewicz 1995] and plotted in figure 2.1.7 (b):

$$\hbar\omega = E_g - (E_A + E_D) + \frac{e^2}{4\pi\epsilon_0\epsilon_S R} \quad (2.8)$$

where  $R$  - acceptor – donor distance ;  $\epsilon_S$  - low frequency permittivity.

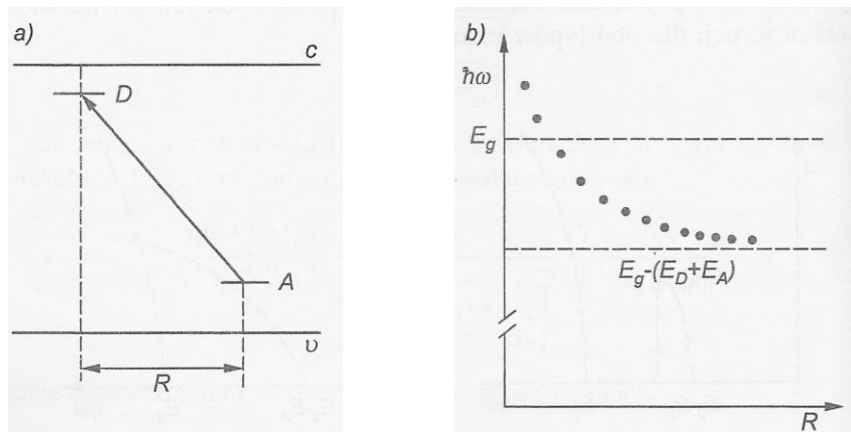


**Figure 2.1.7 Transitions acceptor - donor (a), acceptor – donor transition energy dependence on acceptor – donor distance [Bacewicz 1995].**



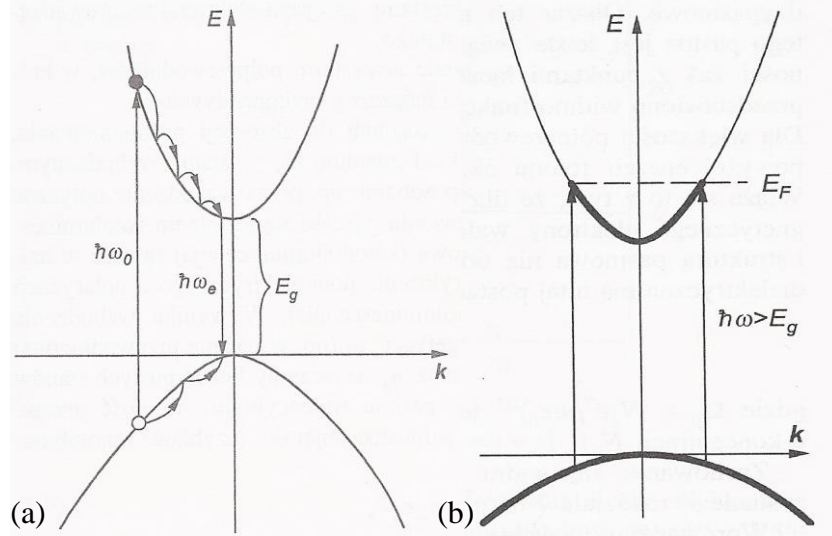


**Figure 2.1.8 Thermalisation of excited electrons ( $\hbar\omega_0$  – absorbed photon energy,  $\hbar\omega_e$  emitted photon energy) (a) and influence of occupied states in conduction band on optical transitions. Burstein-Moss effect.  $E_F$  - Fermi energy (b) [Bacewicz 1995].**

Theoretically the optical emission transitions are possible at all energies at which optical absorption is possible, however the process of light emission takes advantage of the carriers from the proximity of the bottom of the conduction band and the valley of the valance band. Excited electrons with  $\hbar\omega_0$  transfer their energy to the lattice vibrations – creating series of phonons in the thermalisation process as shown in figure 2.1.8. Then, they reach the minimum of the conduction band and they may recombine with a hole from the valence band emitting a photon of energy  $\hbar\omega_e$ . Irradiation with high laser intensities of the n doped semiconductor crystals increases the density of electron states at the minimum of the conduction band. This phenomenon shifts slightly the absorption edge towards higher energies and is called the Burstein-Moss effect which is presented schematically in figure 2.1.8 (b). In Si, GaAs and InP semiconductor crystals the bandgap energy is inversely proportional to the temperature increase. It is illustrated in eq. 2.9, 2.10 and 2.11 respectively and in figure 2.1.9. At room temperature the  $E_g$  of Si material is lower than the photons energies of both LD and Nd:YAG lasers respectively. Therefore the Si wafer can efficiently absorb radiation from both laser sources.

$$E_{g(Si)}(T) = 1.17 - 4.73 \cdot 10^{-4} \cdot \frac{T^2}{T + 636} (eV) , \text{ where } T \text{ is in degrees K} \quad (2.9)$$

$$E_{g(GaAs)}(T) = 1.519 - 5.405 \cdot 10^{-4} \cdot \frac{T^2}{T + 204} (eV) \quad \text{where } (0 \text{ K} < T < 10^3 \text{ K}) \quad (2.10)$$

$$E_{g(InP)}(T) = 1.421 - 4.9 \cdot 10^{-4} \cdot \frac{T^2}{T + 327} (eV) , \text{ where } (0 \text{ K} < T < 800 \text{ K}) \quad (2.11)$$

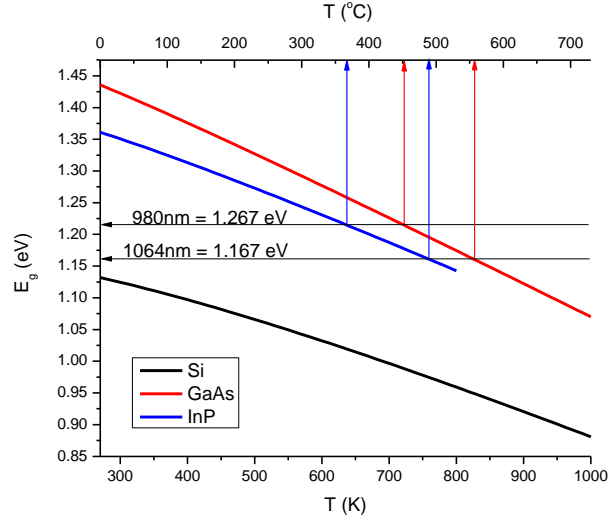


**Figure 2.1.9** Calculated dependence of the  $E_g$  for Si, GaAs and InP semiconductor materials according to the temperature. Vertical lines indicate temperatures at which  $E_g$  of GaAs and InP equals the photons energies of the LD or Nd:YAG lasers respectively.

However, the room temperature  $E_g$  of GaAs and InP crystals are greater than both the LD and Nd:YAG lasers' photons energies. This causes the intrinsic GaAs and InP wafers at room ambient to absorb not more than 5% of the LD or Nd:YAG lasers irradiation energy. Optical absorption of Si, GaAs and InP semiconductors increases exponentially around the Urbach edge region -  $E_g$  according to the equation 2.12 [Beaudoin, DeVries et al. 1997].

$$\alpha(\hbar\omega) = \alpha_g \exp\left(\frac{\hbar\omega - E_g}{E_0}\right), \quad (2.12)$$

where  $\alpha_g$  – optical absorption coefficient at the bandgap energy,  $E_0$  – characteristic energy of the Urbach edge,  $E_g$  – extrapolated bandgap energy.

Although the exponential absorption edge is commonly seen in semiconductor materials, there is no universal model of this dependency. To explain this phenomenon, various models take into account derogations of the real semiconductor crystal lattice from its ideal structure such as structural defects and influence of dopants, which may have energy levels within the  $E_g$  and be responsible for band tail formation. Moreover, the amplitudes of lattice vibrations are proportional to the local temperature generated by the laser beam in the crystal and constitute a major factor of optical absorption edge formation called also as Urbach absorption edge.

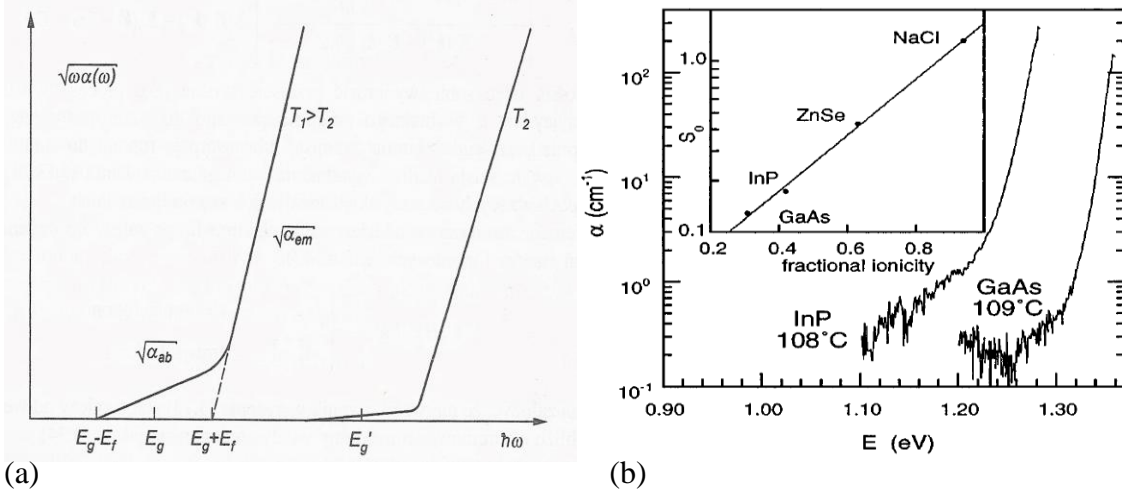


**Figure 2.1.10 Absorption edge of silicon at two different temperatures [Bacewicz 1995] (a) and of GaAs at 109 °C and InP at 108 °C [Beaudoin, DeVries et al. 1997] (b).**

The temperature dependence of the optical absorption of a semiconductor with an indirect bandgap is demonstrated in figure 2.1.10 (a). It shows transition of the absorption curve towards lower photon energies for elevated semiconductor temperatures. Typical absorption spectra for semi-insulating GaAs and InP materials are shown on figure 2.1.10 (b). The insert demonstrates the exponential relationship between the coupling parameter  $S_0$  for the Urbach slope and the fractional ionicity of representative binary compounds [Beaudoin, DeVries et al. 1997]. When the semiconductor material is irradiated with photons of energy lower than  $E_g$ , the material is weakly heated due to low absorption of  $0.1 - 10 \text{ cm}^{-1}$ . Although irradiation of near transparent GaAs or InP based wafers with high power 980 nm LD allows to elevate their temperature, the GaAs and InP wafers become suddenly opaque after their  $E_g$  become smaller than the operating laser photons energies. This may induce high thermal stress and, depending on the ratio between the sample and the operating LD beam diameters, could result in the sample damage. Therefore I have introduced a Si wafer as a holder for GaAs and InP based samples to facilitate heating up these microstructures to their background temperatures at which both the LD and Nd:YAG lasers photons energies are higher than  $E_g$  of GaAs or InP based microstructures. The temperature dependence of the Si, GaAs and InP intrinsic absorption coefficient plots are presented in figures 2.1.11.-2.1.13.

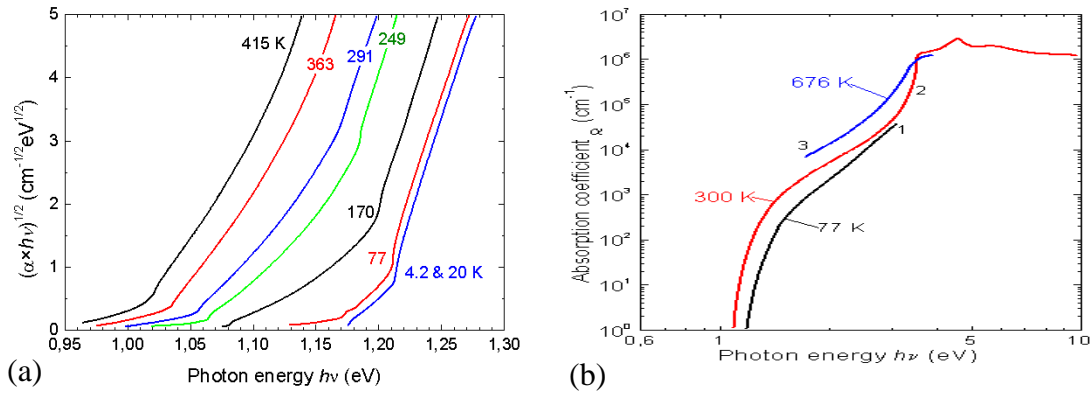


Figure 2.1.11 Low-level absorption spectrum of high purity Si at various temperatures (a) [Macfarlane, McLean et al. 1959] and absorption coefficient vs. photon energy at different temperatures (b) [Sze 1981; Jellison and Modine 1982].

Absorption of semiconductor material increases by orders of magnitude following its crystal lattice temperature elevation. It is important to notice that absorption of doped materials is much higher than that of intrinsic semiconductors and increases proportionally to the doping concentration [Burkhard, Dinges et al. 1982; Bugajski and Lewandowski 1985]. Absorption increases also by orders of magnitude for higher energy photons due to the multiple absorption mechanisms that are involved. When  $E_{\text{photon}}$  is higher than  $E_g$  there is an avalanche generation of free carriers, which heat up the material by thermalisation mechanism. The excited electrons are called hot carriers due to

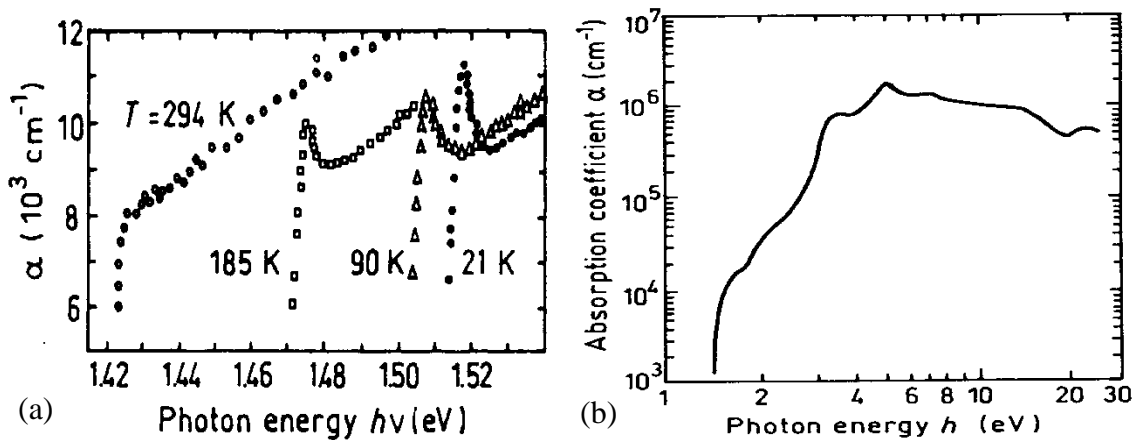
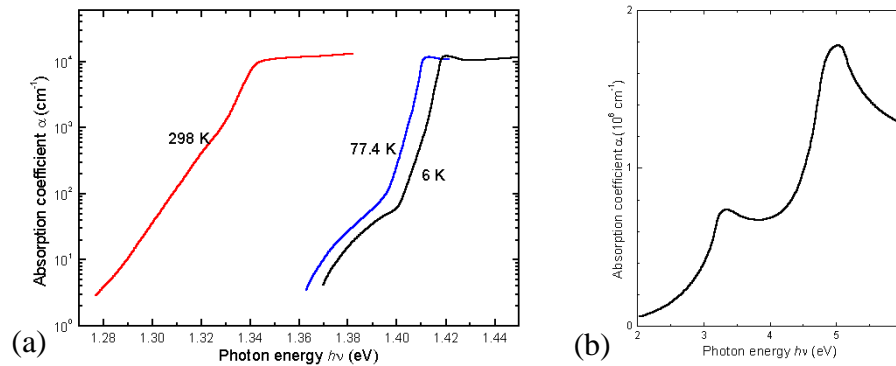
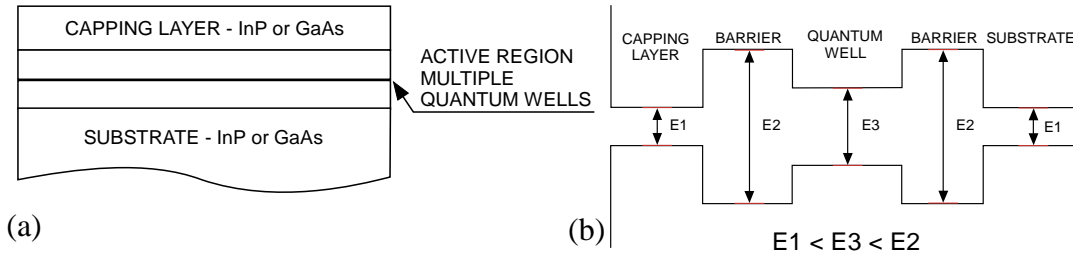


Figure 2.1.12 GaAs intrinsic absorption coefficient near the intrinsic absorption edge for different temperatures (a) [Sturge 1962] and absorption coefficient versus photon energy (b) [Casey, Sell et al. 1975].



**Figure 2.1.13 InP intrinsic absorption coefficient near the intrinsic absorption edge for different temperatures (a) [Turner, Reese et al. 1964] and absorption coefficient vs. photon energy (b) [Aspnès and Studna 1983].**

Auger recombination process that may heat up the material system. This is a three-carrier recombination process, involving either two electrons and one hole or two holes and one electron. The laser light absorption by semiconductor material e.g. Si, GaAs and InP depends on various laser beam parameters: the incident light's wavelength, intensity, angle of incidence and as well as wafer's material parameters: wafer's reflectivity, opacity, thickness, surface roughness and temperature. Primarily, the material is heated through a few non-radiative recombination centers with high power laser beam. After the first few layers achieve high temperature, over the Urbach edge absorption grows up for few orders of magnitude [Johnson and Tiedje 1995] and the material is heated more homogeneously. If the QW material is capped with same material as chosen for QW region then the energy bandgap in the QW would be higher than that of capping layer. Light absorption and also heat generation would take place mostly in the capping layer as presented in figure 2.1.14. I have estimated that the overall absorption of e.g. the InP cap and a 375- $\mu\text{m}$ -thick substrate at room temperature is over 300 times greater than that of the active region [Stanowski and Dubowski 2009]. Furthermore, only 0.05% of the 980 nm radiation was measured to be absorbed at this temperature by the investigated heterostructures [Stanowski and Dubowski 2009]. After preheating the surface region to temperatures at which the semiconductor bandgap is comparable or smaller than the laser photon energy (approximately 360 °C for InP), absorption  $\alpha$  will become non-negligible.



**Figure 2.1.14 Structure of Laser - RTA processed QS wafer (a) and energy band structure of active region (b).**

The InP absorption increases exponentially to  $9 \times 10^5$  and  $2.3 \times 10^6 \text{ cm}^{-1}$  at 550 and 750 °C, respectively. Thus, it is reasonable to assume that the heating of the investigated microstructures occurs primarily due to absorption of the laser radiation in InP capping and substrate layers. The same situation occurs in the GaAs/AlGaAs quantum microstructures because the absorption of capping and substrate layers is much stronger than the absorption of the QW active region due to both smaller bandgap energy and significantly smaller thickness as shown in figure 2.2.14(a). At 300K for GaAs and all Al compositions in  $\text{Al}_x\text{GaAs}_{1-x}$ , the bandgap energy  $E_g$  is higher than energy of photons of the Nd:YAG 1064nm laser. Generation of heat in the wafer structure takes place due to the following factors: the heat is generated just beneath the surface because of the many defects and impurities, which may cause heat generation centers. Secondly heat is generated in the Si doped  $10^{18}$  GaAs capping and substrate layers. For temperatures higher than 500 °C the bulk absorption of GaAs and InP reaches  $10^4$ - $10^5 \text{ cm}^{-1}$  [GaAs, APA, APA], which for the Nd:YAG laser corresponds to the absorption depth of 1.0 - 0.1  $\mu\text{m}$ . To model the Laser-RTA temperature profiles induced in InGaAsP/InP sample, I have carried out calculations for a  $\text{SiO}_2$  coated InP wafer ( $\epsilon = 0.7$ ). Such an approximation is quite reasonable given that the thickness of this wafer (375  $\mu\text{m}$ ) significantly exceeds that of the QW-barrier active region (~ 70 nm).

### **2.1.4 Antireflection layer of SiO<sub>2</sub>**

The laser – RTA technique processing times and related transient heat generation gradients in QS microstructures depend strongly on optical absorption efficacy of both the 980 nm and 1064 nm lasers radiation wavelengths. The absorption of laser radiation in both GaAs and InP based QS wafers may be increased by deposition of single layer of SiO<sub>2</sub> anti-reflection coating. The thickness of this film layer should be equal to a quarter of the incident radiation wavelength, so for  $\lambda=1064$  nm the coating's thickness should be of 266 nm. The PECVD deposited 270 nm SiO<sub>2</sub> coating layer reduced reflection of Nd:YAG 1064 nm wavelength from 34 % to 10 %. The refractive index of the anti-reflection coating layer ( $n_{\text{SiO}_2} = 1.53413$  at  $T=23^\circ\text{C}$  [Palik 1998]) should be also smaller than that of the semiconductor wafer ( $n_{\text{GaAs}} = 3.478$  at  $T=23^\circ\text{C}$  [Palik 1998];  $n_{\text{InP}} = 3.290$  at  $T=23^\circ\text{C}$  [Adachi 1987]).

## **2.2 Finite element method of modeling temperature profiles in GaAs and InP semiconductors**

### **2.2.1 Calculation of the heat transfer**

A finite element method (FEM) [O. C. Zienkiewicz 1996] was implemented for solving the heat transfer Partially Differential Equations (PDE) and to determine the temporal and spatial temperature profiles induced in InP and GaAs semiconductor wafers by the LD and Nd:YAG lasers. The calculations were carried out using the commercial COMSOL software. The FEM approach takes advantage of the finite element discretization of the calculated model's geometry into mesh elements. The properties of adjacent elements in the nodes of the generated net are shared during progressive iteration steps, so the energy flux phenomena could be calculated, e.g., for diffusion or heat transfer. The FEM method allows generating mesh elements of various sizes and shapes, depending on the modeled physical process. The size of mesh elements is a critical factor for accuracy of the calculated results, but it also influences the total time of calculations. The heat balance

according to the heat transfer PDE, for every differential element, is based on the following relation:

Heat in – Heat out = Heat accumulated + Heat generated [Steen 1998], which could be expressed by the following equation 2.13:

$$Q - \nabla(k\nabla T) = \rho C_p(\partial T/\partial t) \quad (2.13)$$

The formula for  $Q$  describes the heat source and takes into account the optical reflectivity, the laser beam power density, the beam shape and optical absorption of the irradiated wafer. The boundary equation 2.14 is given by:

$$q_0 - h(T_{inf} - T) + \varepsilon \cdot \sigma \cdot (T_{amb}^4 - T^4) = k\nabla T \quad (2.14)$$

The definition of the symbols describing eq. 2.13 and 2.14 and their values used in the calculations are gathered in Table I. By solving eqs 2.13 and 2.14, it is possible to describe the temporal and spatial temperature profiles induced by both the LD and Nd:YAG lasers at any point of the wafer. The 3D FEM model includes the background heating provided by the LD source and describes the effect of the laser beam on achievable maximum temperatures. This model has been tested also for Si wafer of 2 inch in diameter and the calculated temperature temporal behaviour is in good agreement with temperature gradients monitored experimentally. Various laser irradiation conditions have been investigated. Separated influences of  $k$ –thermal conductivity,  $\alpha$ –optical absorption and  $\varepsilon$ –emissivity, assumed constant or temperature dependent, on calculated temperature temporal behaviour in the middle of laser irradiated zone are presented. Other parameters:  $C_p$ –specific heat,  $\rho$ –density were assumed as temperature independent. The density of InP varies by less than 3% in the temperature range between 23 and 800 °C, so we assumed it to be constant. Although the specific heat  $C_p$  is temperature dependent, its weak temperature dependence (it changes from 410 J/kg·K at 300 K to 455 J/kg·K at 1000 K [Palankovski, Schultheis et al. 2001]) indicates that such dependence has a negligible effect on the accuracy of our calculations. The simulations showed the importance of using the temperature dependent thermal conductivity coefficient,  $k$ . Its value at 1000 K is 3.6 times smaller than at room temperature [Palankovski, Schultheis et al. 2001]. This results in slower heat dissipation at elevated temperatures and, consequently, in faster rates of temperature increase induced by the laser beam.



**Table 1. Experimental parameters used for modeling [Stanowski 2005; Stanowski 2006; Voznyy 2006; Stanowski, Bouaziz et al. 2008; Stanowski and Dubowski 2009; Stanowski, Martin et al. 2009].**

Symbol	Definition	Value
Q	Laser generated heat	$(1-R) \cdot I \cdot A \cdot \alpha \cdot \exp(-\alpha \cdot z)$ [W/m <sup>3</sup> ]
I	Laser beam intensity	$1064\_Power / (\pi \cdot 1064\_radius^2)$ [W/m <sup>2</sup> ]
A	Laser beam shape function	$\exp(-(x^2+y^2)/(2 \cdot 1064\_radius^2))$
q <sub>0</sub>	Laser energy inward flux	$I \cdot A \cdot (1-R)$ [W/m <sup>2</sup> ]
T	Wafer temperature	calculated [K]
z	Laser radiation penetration depth	calculated [m]
σ	Stefan Boltzman's constant	$5.67 \cdot 10^{-8}$ [W/m <sup>2</sup> ·K <sup>4</sup> ]
T <sub>inf</sub>	Temperature above surface	T-50[K]
T <sub>amb</sub>	Ambient temperature	296 [K]

	Si	InP	GaAs
R	10%	3%	10%
$\alpha$	1 [cm <sup>-1</sup> ] @T>77K 2.3 [cm <sup>-1</sup> ] @T>300K 2·10 <sup>3</sup> [cm <sup>-1</sup> ] @T>676K [Sze 1981]	1·10 <sup>-7</sup> [cm <sup>-1</sup> ] @T>300K 2.3 [cm <sup>-1</sup> ] @T>530K 1.5·10 <sup>5</sup> [cm <sup>-1</sup> ] @T>775K 7.8·10 <sup>7</sup> [cm <sup>-1</sup> ] @T>975K [Beaudoin, DeVries et al. 1997]	3, 10, 100, 1000, 20000 or -735907+2487T[m <sup>-1</sup> ]
Cp	703[J/(kg·K)]@300K [Ioffe]	410[J/(kg·K)] @300K [Sze 1981] 455 [J/(kg·K)] @1000K [Palankovski, Schultheis et al. 2001]	325 [J/(kg·K)] [Ioffe]
k	605·exp(-T/205)+27 200 K < T < 1200 K [W/(m·K)] [Glassbrenner and Slack 1964]	259·exp(-T/182)+15 200 K < T < 1200 K [W/(m·K)] [Palankovski, Schultheis et al. 2001]	56 or 16280/T [W/(m·K)]
$\rho$	2329 [kg/m <sup>3</sup> ] [Ioffe]	4810 [kg/m <sup>3</sup> ] [Ioffe]	5317 [kg/m <sup>3</sup> ] [Ioffe]
h	20 [W/m <sup>2</sup> ·K]	20 [W/m <sup>2</sup> ·K]	20 [W/m <sup>2</sup> ·K]
$\varepsilon$	0.7 [Ravindra, Abedrabbo et al. 1998]	0.7 [Timans 1992]	1, 0.8, 0.6, 0.4

R - Reflectivity at 1064nm,

$\alpha$  - Absorption of 1064nm

Cp - Specific heat,

k - Thermal conductivity

$\rho$  – Density

h - Convective heat transfer

$\varepsilon$  - Emissivity

## 2.2.2 Transient temperature profiles

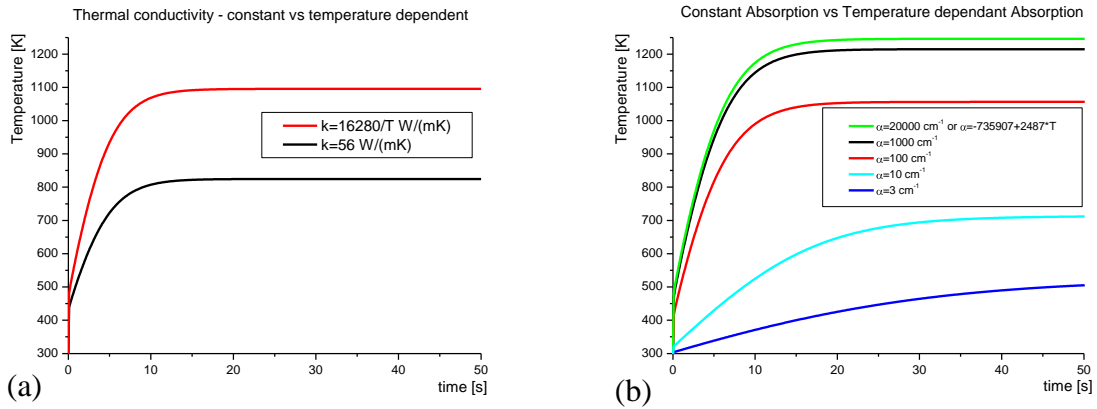


**Figure 2.2.1 Thermal conductivity dependence on temperature -  $k(T)$  (a) and optical absorption dependence on temperature -  $\alpha(T)$  (b) [Stanowski 2005].**

Figure 2.2.1 (a) presents the difference between calculated maximum transient temperatures in the middle of laser irradiated zone for constant and temperature dependent  $k$ -thermal conductivity of GaAs wafer. This graph explains that the thermal conductivity is strongly temperature dependent parameter and its value decreases when the temperature of the heated specimen increases. The difference between the maximum temperatures reached is about 300K. Figure 2.2.1 (b) shows the influence of different constant optical absorption values on the heating rate of the semiconductor wafer. For higher optical absorption values the smaller volume of the irradiated material is directly heated, so the temperature increases significantly faster at laser-irradiated areas. Consequently, the temperature gradients in the irradiated wafer microstructure become much sharper. Calculated temperature transient profiles for temperature dependent optical absorption equals the calculated profiles for constant absorption values higher than  $5000 \text{ cm}^{-1}$ . The possible source of error in determining laser-induced temperature is related to the use of a single color pyrometer and the unknown emissivity of the wafer. Temperature in the middle of the laser irradiated zone was measured with optical pyrometer with 50mm focal length lens from area of about  $2\text{mm}^2$ . The pyrometer monitored the temporal temperature behaviour with time step of 0.1s.

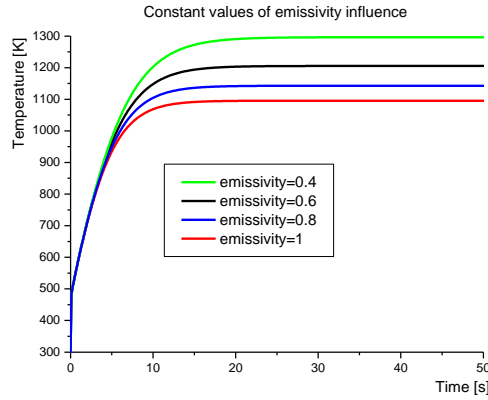


**Figure 2.2.2 Emissivity dependence on maximum temperature [Stanowski 2005].**

Figure 2.2.2 shows transient temperatures in the GaAs wafer, calculated for  $k=16280/T$  and  $\alpha=-7492.5+24.985T \text{ cm}^{-1}$  and various emissivity coefficients ( $\epsilon = 0.4 ; 0.6 ; 0.8 ; 1$ ). Assumption of the ideal case of the black body surface ( $\epsilon = 1$ ) results in an underestimation of the temperature. A difference of 166 K in the saturation temperature is expected if the surface of GaAs has emissivity reduced to  $\epsilon = 0.4$ . The relation between the one-color pyrometer measured and real temperature is described by eq. 2.15 [Kucharski D. , 2009].

$$T_{real} = T_{measured} \cdot \sqrt[4]{\frac{1}{\epsilon}} \quad (2.15)$$

Figures 2.2.3 and 2.2.4 compare the measured and calculated temperature values for, GaAs and Si wafers irradiated with LD and with LD combined with Nd:YAG laser.

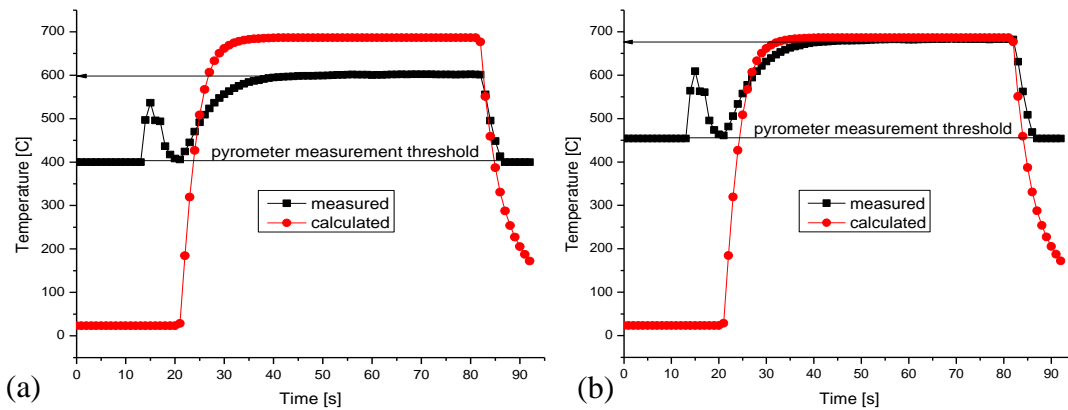


**Figure 2.2.3 Calculated vs measured ( $\epsilon = 1$ ) transient point GaAs wafer temperature induced with 980 nm LD (a) emissivity corrected ( $\epsilon = 0.7$ ) (b).**

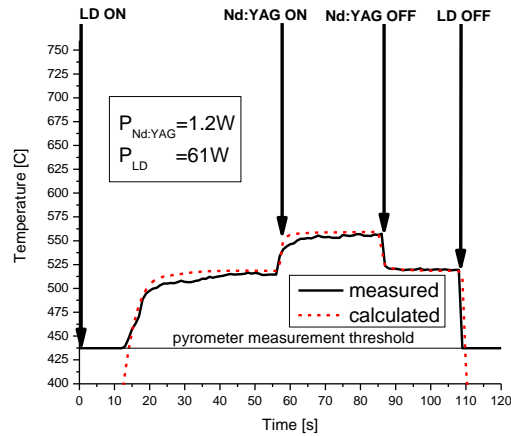


**Figure 2.2.4** Calculated vs measured ( $\epsilon = 0.7$ ) transient point Si wafer temperature induced with 980 nm LD and 1064 nm Nd:YAG lasers [Stanowski and Dubowski 2009].

A reasonable fit has been obtained for Si, AlGaAs/GaAs (AX04-182) and InGaAsP/InP (RA30360). Backside irradiation of the Si wafer with 61 W LD, as shown by the experimental results (solid line) allows to achieve a steady temperature of about 515 °C within approximately 25 s from the on-set of the irradiation. Additional irradiation with the 1.2W Nd:YAG laser at the 58<sup>th</sup> second of the experiment results in a rapid increase of the temperature to 555 °C. This temperature transition is achieved in about 5 s. Conversely, the rate at which wafer temperature decreases, following the switching off the Nd:YAG laser, is less than 1 s. These fast heating cooling rates are achievable due to the method of direct heating of the wafer with the laser, and they likely represent the ultimate rates achievable with any RTA technique. The calculated transient temperature (broken line) describes reasonably well the dynamics of the process. The absolute values of calculated temperatures depend on the emissivity value ( $\epsilon$ ) of the wafer. For the case discussed in figures 2.2.4 and 2.2.5, I used  $\epsilon = 0.7$ , in agreement with reported data for Si at this temperature range [Ravindra, Abedrabbo et al. 1998]. Further verification of the accuracy of FEM-based modelling was provided by studying the Laser-RTA of GaAs and InP wafers. In these cases I used  $\epsilon = 0.7$ , which is greater than the emissivity of bulk GaAs or InP materials reported in literature [Timans 1992]. Such an assumption, however, seems justified, given the

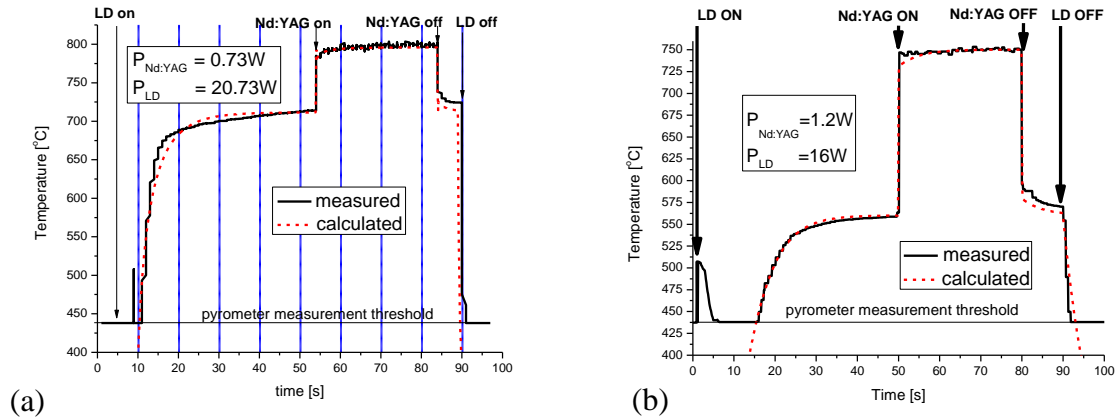


**Figure 2.2.5** Calculated vs measured ( $\epsilon = 0.7$ ) transient point GaAs (a) and InP (b) wafers temperature induced with 980 nm LD and 1064 nm Nd:YAG lasers [Stanowski and Dubowski 2009].

observed drastic reduction of the reflected power from InGaAsP/InP wafer following its coating with the  $\text{SiO}_2$  layer. Note that achieving the same background temperature of the AlGaAs/GaAs and InGaAsP/InP wafers as that of the Si wafer required only 20.73 W and 16 W of the LD power respectively. Experimental results (solid line) show that this temperature is reached LD approximately 45 and 35 s from the onset of the irradiation for GaAs and InP based microstructures. Additional irradiation with 0.73 W and 1.2 W Nd:YAG laser, at the 54<sup>th</sup> and 50<sup>th</sup> second of the experiment, resulted in a rapid increase of the temperature to 800°C and 750°C, as shown in Fig. 2.3.5 (a) and (b), respectively. This temperature transition is achieved in less than 1 s, which is primarily due to the lower heat conductivity (dissipation) of GaAs and InP in comparison to that of Si. The contribution of the  $\text{SiO}_2$  layer to this behaviour is marginal as its heat conductivity is significantly smaller than that of the GaAs or InP wafers. The rapid temperature decrease (less than 1.5 s) that is observed in this case, is comparable to the cooling rate of Si wafer. It can be seen that the FEM model (broken line) provides a reasonable description of measured transient temperatures. For all Si, AlGaAs/GaAs and InGaAsP/InP wafers, the measured background temperatures stabilize at slightly slower rates than those predicted by the calculations. The likely reason for this discrepancy is the insufficient thermal isolation of wafers. However, it is clear that our model describes quite well the dynamics of the laser heating and cooling processes in semiconductor wafers.

### 2.2.3 Lateral and in-depth temperature profiles

The FEM model has been used to calculate the spatial temperature profiles of wafers irradiated with a CW 980nm LD and CW 1064nm Nd:YAG lasers beams. The eight graphs in figures 2.2.6 and 2.2.9 show comparisons of lateral (a) and in-depth (b) temperature profiles induced with both 700 $\mu\text{m}$  and 100 $\mu\text{m}$  irradiating Nd:YAG laser beam diameters. In figures 2.2.6 and 2.2.7 the heat transfer was calculated for various convection conditions: in vacuum, at room ambient and when the specimen was cooled by a forced gas flow. The results demonstrate that achieving the same process temperature at cooling conditions requires doubling the laser beam intensity in comparison to irradiation in vacuum. Excessive thermal stress could result in damage of the surface.

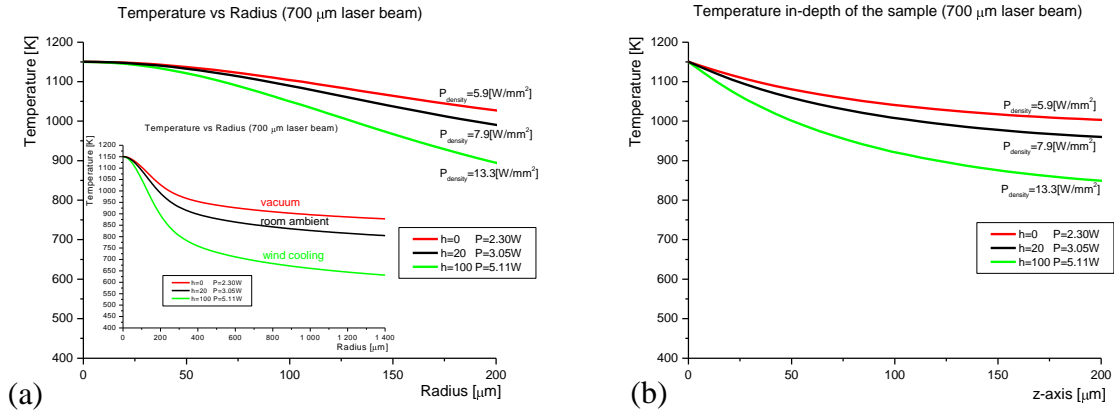


**Figure 2.2.6 Lateral (a) and in-depth (b) temperature profiles induced with 700  $\mu\text{m}$  in diameter Nd:YAG laser beam for various convection ( $h=0$  ; 20 ; 100) coefficients [Stanowski 2005].**

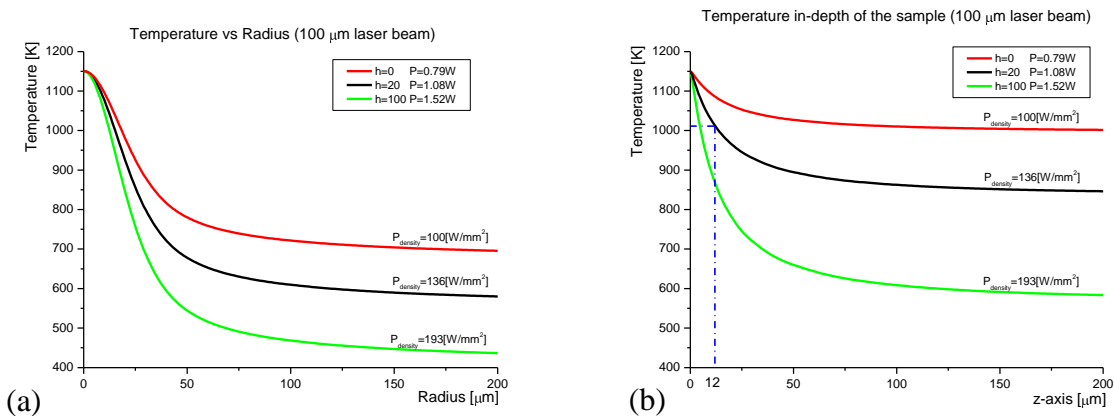


**Figure 2.2.7 Lateral (a) and in-depth (b) temperature profiles induced with 100  $\mu\text{m}$  in diameter Nd:YAG laser beam [Stanowski 2005].**

Therefore, it is necessary to preheat the sample's process area to background temperature - below the intermixing threshold temperature. It could be done with a second laser beam of larger diameter, which induces heat in a more localized processing volume, so the depth at which QW is located is an important parameter in achieving high spatial resolution QWI. In figures 2.2.8 and 2.2.9, the heat transfer was calculated for various background temperatures: 300, 773 and 973 K. The additional background heating to 973 K allows decreasing the processing laser beam intensity by factors of 3 and 5 times for 700  $\mu\text{m}$  and 100  $\mu\text{m}$  laser beams respectively, comparing to processing at 300 K. The results show that to perform direct QWI and prevent from the surface damage the background heating is inevitable for processing with 100  $\mu\text{m}$  laser beam diameters and smaller.

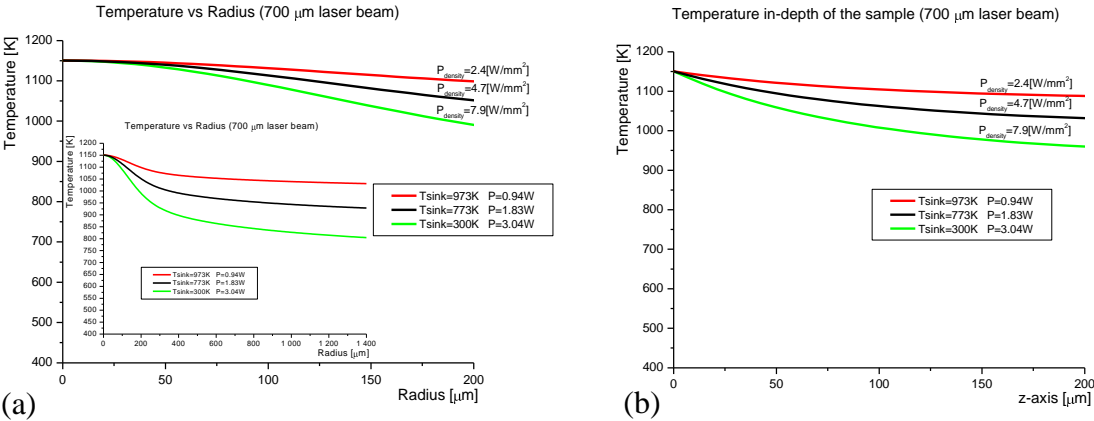


Figure 2.2.8 Lateral (a) and in-depth (b) temperature profiles induced with 700  $\mu\text{m}$  in diameter Nd:YAG laser beam [Stanowski 2005].

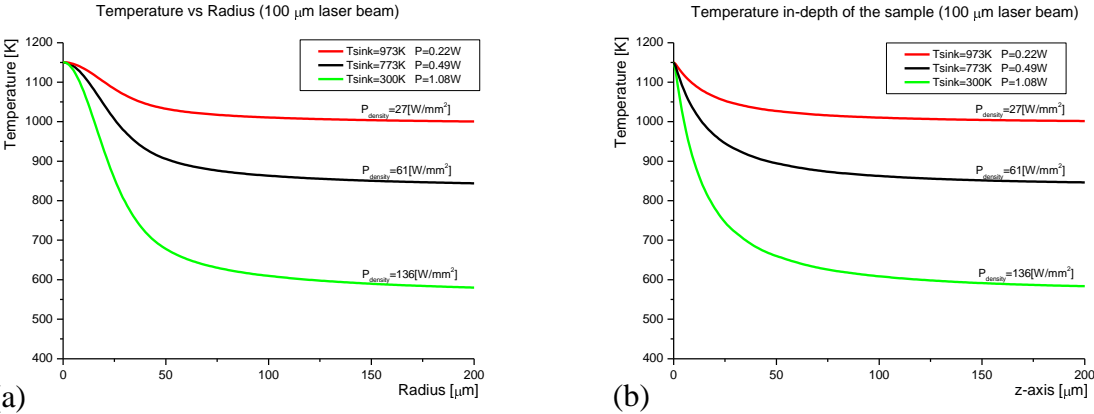
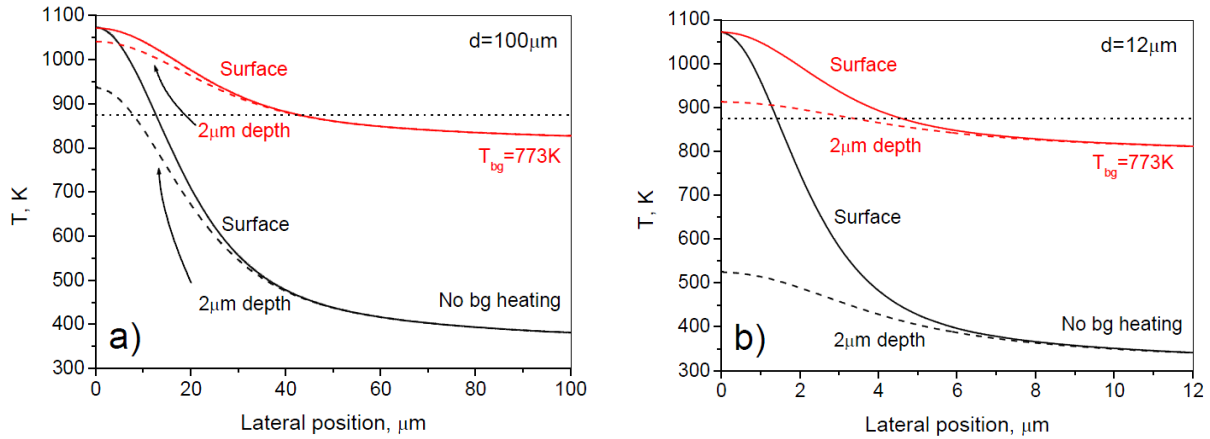


Figure 2.2.9 Lateral (a) and in-depth (b) temperature profiles induced with 100  $\mu\text{m}$  in diameter Nd:YAG laser beam [Stanowski 2005].





**Figure 2.2.10** Calculated temperature profiles on the surface and 2  $\mu\text{m}$  below the surface for InP wafer irradiated by laser beams of 100  $\mu\text{m}$  (a) and 12  $\mu\text{m}$  (b) diameters. Horizontal, dotted line indicates the threshold temperature for which a 90 s RTA includes no significant PL shift [Voznyy 2006]

Additional background heating could also improve the crystal lattice optical properties by the annealing of its structural defects. To maintain the laser beam power density value below surface damage threshold for AlGaAs/GaAs microstructures, background heating has to be introduced. The developed FEM model allowed to calculate the temperature profiles induced in InP-based semiconductor microstructures in processing with smaller Nd:YAG beam diameters [Voznyy 2006]. Figure 2.2.10 (a) and (b) shows calculated temperature profiles for 100  $\mu\text{m}$  and 12  $\mu\text{m}$  beam diameters respectively and different background temperatures. It can be seen in figure 2.2.10 (b) that for 12  $\mu\text{m}$  beam the temperature at 2  $\mu\text{m}$  below the surface is much lower than needed for the intermixing. Background heating can significantly increase the temperature below the surface for the 100  $\mu\text{m}$  beam, but for 12  $\mu\text{m}$  beam diameter, even with background heating, the temperature induced at a depth greater than 2  $\mu\text{m}$  would not be sufficient to induce QWI [Voznyy 2006]. Thus, the diameter of the heating laser beam has to be adjusted depending on the depth at which the QW is located and required resolution of the Laser – RTA QWI process. .

## 2.3 Processing with moving Nd:YAG laser beam

The developed 3D geometry FEM model allows calculating temperature temporal behaviour for rapidly moving laser beam across the wafer's specimen. Solving this problem was not trivial as no proper functions were available in the commercial Comsol Inc. software libraries. To simulate movement of the laser beam I have introduced a time dependent parameter to the equation describing the Gaussian-shape and position of the laser beam. This corresponding equation 2.16 takes the following form:

$$beam\_Gauss = \frac{\exp(-((A/2 + x - A * \text{mod}(B/A*t,1))^2 + y^2))}{C^2 * 20} \quad (2.16)$$

where: A – distance of laser beam scan; B – velocity of the laser beam; C – laser beam diameter; x, y are space coordinates; mod(velocity/dist\*t,1) – modulo function presented in figure 2.3.1.

This solution has been appreciated by COMSOL Inc. and incorporated to their libraries of suggested functions.

Figure 2.3.1 shows the temporal pattern of the laser beam used in the calculations. Resolution of the process is dependent on laser beam diameter, optical power density, movement speed, thermal conduction of the irradiated semiconductor microstructure and the efficiency of heat radiation and convection.

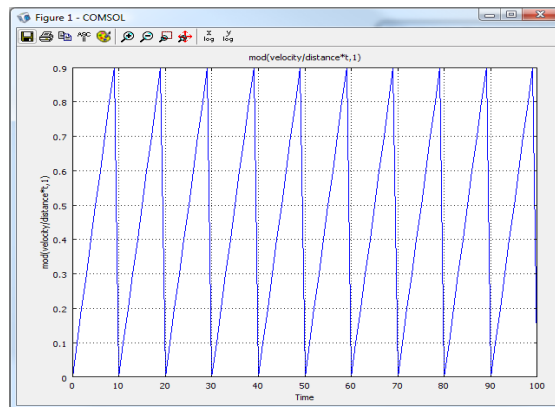
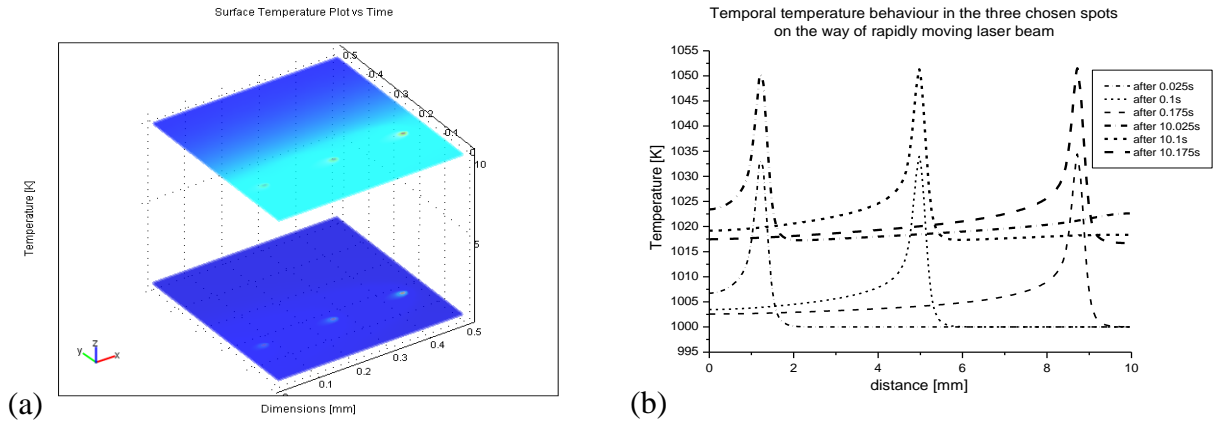


Figure 2.3.1 Modulo function implemented to the equation 2.3.1 for modeling of the moving laser beam.



**Figure 2.3.2 Surface temperature plot for 3 chosen moments of irradiation by rapidly moving laser beam (a) and corresponding lateral temporal temperature (b) [Stanowski 2005].**

For the illustration purpose, I present in Fig. 2.3.2 the results of FEM calculations of temperature profiles generated by a laser beam moving at 5 cm/s. While the temperature of the whole wafer's area which is maintained by additional background heating stays below QWI temperature threshold, the rapidly moving Nd:YAG laser beam writes lines in selected areas of the wafer.

It is due to the QWI temperature threshold that the width of the line/spot of the intermixed material could be even smaller than the diameter of the operating laser beam. Temperature profiles along the longer axis of the InP sample induced with a 41 W LD and a moving spot (500  $\mu\text{m}$ ) of the 1.2 W Nd:YAG laser beam are presented in figure 2.3.3.

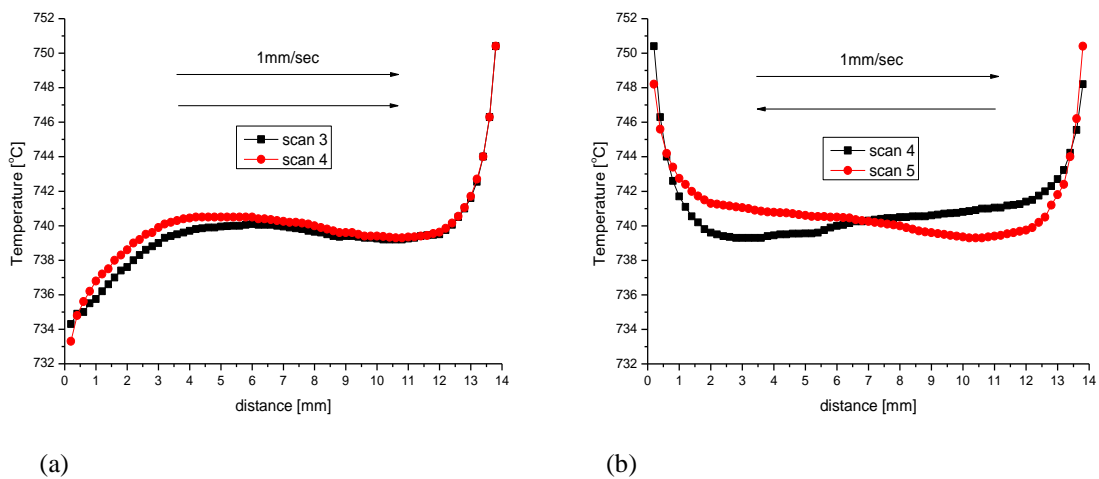


**Figure 2.3.3 Temperature profiles along the center of an InP sample induced with 41W 980 nm LD (24 mm diameter spot) and a spot (500  $\mu\text{m}$ ) of the 1.2 W Nd:YAG laser moving in one direction (a) and in two directions (b) [Stanowski 2005].**

The results have been plotted for scans repeated in one direction (figure 2.3.3 (a)) and two directions (figure 2.3.3 (b)). A one-direction scan indicates that one of the sample edges will be underheated, while the other overheated. Scanning in two directions will result in a more uniform average temperature in the center of the sample. Therefore, the studies case indicates that the two-direction scan mode is preferable for writing uniform lines of the QWI InGaAsP/InP material.

## 2.4 Conclusions

FEM calculations have been carried out to determine the temperature profiles in CW 980 nm LD and CW 1064 nm Nd:YAG lasers annealed AlGaAs/GaAs and InGaAsP/InP QW microstructures. Heat convection appeared to be a very important parameter. In vacuum conditions, sample loses its thermal energy only due to radiation. Thus, greater amounts of thermal energy are accumulated inside the semiconductor microstructure and the achieved temperatures are higher than those, when the sample is irradiated at room ambient conditions or when the heat flux-convection process is increased by using additional controlled gas flow cooling. Increasing thermal convection of the laser heated wafer leads to narrower temperature profiles, but higher power densities have to be used. The simulations have indicated that for high convection conditions, the laser beam power densities could be maintained below the surface damage threshold value [Stanowski 2006] when additional background heating of the whole wafer's body up to high temperature value (500°C – 700°C) is incorporated. Processing with decreasing laser beam diameter can lead to sharper temperature profiles. At low temperatures (about 300K) both GaAs and InP are almost transparent to Nd:YAG 1064 nm laser irradiation. But, at temperatures exceeding 800 K, the optical absorption of these material becomes significant, and almost all delivered laser beam power is absorbed within the thin layer of the material. Therefore, I have introduced to the setup a Si wafer to support the QWI samples. Si wafer is opaque at room temperature to high power 980 nm LD beam radiation and moreover has higher thermal conduction coefficient which helps to homogenize the background temperature distribution profile induced with multimode laser beam. Shallow temperature propagation has been observed for small laser beam diameters, thus depth at which QW is located is an important parameter to achieve high spatial resolution of QWI.

## Bibliography

- Adachi, S. (1987). "Model dielectric constants of GaP, GaAs, GaSb, InP, InAs, and InSb." Phys. Rev. B **35**(14): 7454-7463.
- Aimez, V., J. Beauvais, et al. (2002). "Low-energy ion-implantation-induced quantum-well intermixing." Selected Topics in Quantum Electronics, IEEE Journal of **8**(4): 870-879.
- Aimez, V., J. Beauvais, et al. (2001). "Monolithic intracavity laser-modulator device fabrication using postgrowth processing of 1.55  $\mu$ m heterostructures." Applied Physics Letters **79**(22): 3582-3584.
- Aspnes, D. E. and A. A. Studna (1983). "Dielectric functions and optical parameters of Si, Ge, GaP, GaAs, GaSb, InP, InAs, and InSb from 1.5 to 6.0 eV." Physical Review B **27**(2): 985.
- Bacewicz, R. (1995). Optyka ciała stałego. Wybrane zagadnienia. Warszawa.
- Beaudoin, M., A. J. G. DeVries, et al. (1997). "Optical absorption edge of semi-insulating GaAs and InP at high temperatures." Applied Physics Letters **70**(26): 3540-3542.
- Boon Siew, O., K. McIlvaney, et al. (1997). "Selective quantum-well intermixing in GaAs-AlGaAs structures using impurity-free vacancy diffusion." Quantum Electronics, IEEE Journal of **33**(10): 1784-1793.
- Boon Siew, O., O. Teik Kooi, et al. (2004). "Multiple-wavelength integration in InGaAs-InGaAsP structures using pulsed laser irradiation-induced quantum-well intermixing." Quantum Electronics, IEEE Journal of **40**(5): 481-490.
- Brunner, K., G. Abstreiter, et al. (1992). "Optical characterization of GaAs/AlGaAs nanostructures fabricated by focussed laser beam induced thermal interdiffusion." Surface Science **267**(1-3): 218-222.
- Brunner, K., U. Bockelmann, et al. (1992). "Photoluminescence from a single GaAs/AlGaAs quantum dot." Physical Review Letters **69**(22): 3216.
- Bugajski, M. and W. Lewandowski (1985). "Concentration-dependent absorption and photoluminescence of n-type InP." Journal of Applied Physics **57**(2): 521-530.
- Burkhard, H., H. W. Dinges, et al. (1982). "Optical properties of In<sub>1-x</sub>Ga<sub>x</sub>P<sub>1-y</sub>As<sub>y</sub>, InP, GaAs, and GaP determined by ellipsometry." Journal of Applied Physics **53**(1): 655-662.
- Burton, R. S., T. E. Schlesinger, et al. (1993). "High-performance diffusion disordered Al<sub>x</sub>Ga<sub>1-x</sub>As lasers via a self-aligned process and conventional open-tube annealing." Journal of Applied Physics **73**(4): 2015-2018.
- Casey, J. H. C., D. D. Sell, et al. (1975). "Concentration dependence of the absorption coefficient for n- and p - type GaAs between 1.3 and 1.6 eV." Journal of Applied Physics **46**(1): 250-257.
- Choi, W. J. (2000). Dependence of Dielectric Cap Quantum Well Disorder on the Characteristics of Dielectric Capping Film. Semiconductor Quantum Well Intermixing. E. H. Li. Amsterdam, Gordon and Breach. **8**.
- Cibert, J., P. M. Petroff, et al. (1986). "Kinetics of implantation enhanced interdiffusion of Ga and Al at GaAs-Ga<sub>x</sub>Al<sub>1-x</sub>As interfaces." Applied Physics Letters **49**(4): 223-225.
- COMSOL, I. COMSOL. Burlington.

- Cusumano, P., B. S. Ooi, et al. (1997). "Suppression of quantum well intermixing in GaAs/AlGaAs laser structures using phosphorus-doped SiO<sub>2</sub> encapsulant layer." Journal of Applied Physics **81**(5): 2445-2447.
- Dubowski, #160, et al. (1997). "A comparative study of laser- and ion implantation-induced quantum well intermixing in GaInAsP/InP microstructures." **1991**: IX, 294 p.
- Dubowski, J. J. (1999). "Semiconductor laser array fabricated by Nd:YAG laser-induced quantum well intermixing." Proc. of SPIE **1618**: 191.
- Dubowski, J. J. (2003). Laser-induced bandgap shifting for photonic device integration. USA. **6,670,644**.
- Dubowski, J. J. (2009). Laser-based Bandgap Engineering of Quantum Semiconductor Wafers.
- Dubowski, J. J., C. N. Allen, et al. (2000). "Laser-induced InAs/GaAs quantum dot intermixing." Applied Physics Letters **77**(22): 3583-3585.
- Dubowski, J. J., Y. Feng, et al. (2002). "Monolithic multiple wavelength ridge waveguide laser array fabricated by Nd:YAG laser-induced quantum well intermixing." Journal of Vacuum Science & Technology A: Vacuum, Surfaces, and Films **20**(4): 1426-1429.
- Dubowski, J. J., P. J. Poole, et al. (1999). "Enhanced quantum-well photoluminescence in InGaAs/InGaAsP heterostructures following excimer-laser-assisted surface processing." Applied Physics A: Materials Science & Processing **69**(0): S299-S303.
- Dubowski, J. J., C. Y. Song, et al. (2004). "Laser-induced selective area tuning of GaAs/AlGaAs quantum well microstructures for two-color IR detector operation." Journal of Vacuum Science & Technology A: Vacuum, Surfaces, and Films **22**(3): 887-890.
- Epler, J. E., R. D. Burnham, et al. (1986). "Laser induced disordering of GaAs-AlGaAs superlattice and incorporation of Si impurity." Applied Physics Letters **49**(21): 1447-1449.
- Fleming, R. M., D. B. McWhan, et al. (1980). "X-ray diffraction study of interdiffusion and growth in (GaAs)<sub>n</sub>(AlAs)<sub>m</sub> multilayers." Journal of Applied Physics **51**(1): 357-363.
- Genest, J., R. Beal, et al. (2008). "ArF laser-based quantum well intermixing in InGaAs/InGaAsP heterostructures." Applied Physics Letters **93**(7): 071106-3.
- Genest, J., J. J. Dubowski, et al. (2004). UV-laser-based process for quantum well intermixing of III-V heterostructures. Integrated Optics and Photonic Integrated Circuits, Strasbourg, France, SPIE.
- Genest, J. and et al. (2007). "UV laser controlled quantum well intermixing in InAlGaAs/GaAs heterostructures." Journal of Physics: Conference Series **59**(1): 605.
- Glassbrenner, C. J. and G. A. Slack (1964). "Thermal Conductivity of Silicon and Germanium from 3°K to the Melting Point." Physical Review **134**(4A): A1058.
- H H Tan, S. Y., M. Gal, and C. Jagadish (2000). Optoelectronic properties of semiconductors and superlattices. Semiconductor Quantum Well Intermixing. E. H. Li. Amsterdam, Gordon and Breach. **8**.
- H. H. Tan, S. Y., M. Gal, and C. Jagadish (2000). Optoelectronic properties of semiconductors and superlattices. Semiconductor Quantum Well Intermixing. E. H. Li. Amsterdam, Gordon and Breach: 307.
- Helmy, A. S., J. S. Aitchison, et al. (1998). "Quantitative model for the kinetics of compositional intermixing in GaAs-AlGaAs quantum-confined heterostructures." Selected Topics in Quantum Electronics, IEEE Journal of **4**(4): 653-660.

- Hirayama, Y., S. Tarucha, et al. (1988). "Fabrication of a GaAs quantum-well-wire structure by Ga focused-ion-beam implantation and its optical properties." Physical Review B **37**(5): 2774.
- Holonyak, N. (1981). "IR-red GaAs-AlAs superlattice laser monolithically integrated in a yellow-gap cavity." Appl. Phys. Lett. **39**: 102.
- Holonyak, N., Jr. (1998). "Impurity-induced layer disordering of quantum-well heterostructures: discovery and prospects." Selected Topics in Quantum Electronics, IEEE Journal of **4**(4): 584-594.
- Ioffe, O.-T. I. from <http://www.ioffe.rssi.ru/SVA/NSM/Semicond>.
- Jagadish, H. H. T. Y. G. (2000). Semiconductor Quantum Well Intermixing. Amsterdam.
- Jellison, J. G. E. and F. A. Modine (1982). "Optical absorption of silicon between 1.6 and 4.7 eV at elevated temperatures." Applied Physics Letters **41**(2): 180-182.
- Johnson, S. R. and T. Tiedje (1995). "Temperature dependence of the Urbach edge in GaAs." Journal of Applied Physics **78**(9): 5609-5613.
- Kapon, E., N. G. Stoffel, et al. (1988). "BIREFRINGENT CHANNEL WAVE-GUIDES DEFINED BY IMPURITY-INDUCED SUPERLATTICE DISORDERING." Applied Physics Letters **52**(5): 351-353.
- Katayama, M., Y. Tokuda, et al. (1989). "X-ray photoelectron spectroscopic study of rapid thermal processing on SiO<sub>2</sub>/GaAs." Applied Physics Letters **54**(25): 2559-2561.
- Kelly, M. K., C. E. Nebel, et al. (1996). "Lateral structuring of III-V quantum well systems with pulsed-laser-induced transient thermal gratings." Applied Physics Letters **68**(14): 1984-1986.
- Laruelle, F., A. Bagchi, et al. (1990). "Focused ion beam channeling effects and ultimate sizes of GaAlAs/GaAs nanostructures." Applied Physics Letters **56**(16): 1561-1563.
- Liu, X. F., B. C. Qiu, et al. (2000). "Control of multiple bandgap shifts in InGaAs-AlInGaAs multiple-quantum-well material using different thicknesses of PECVD SiO<sub>2</sub> protection layers." Photonics Technology Letters, IEEE **12**(9): 1141-1143.
- Macfarlane, G. G., T. P. McLean, et al. (1959). "Exciton and phonon effects in the absorption spectra of germanium and silicon." Journal of Physics and Chemistry of Solids **8**: 388-392.
- Marsh, J. H. (1993). "Quantum well intermixing." Semiconductor Science and Technology(6): 1136.
- Marsh, J. H. (2000). Impurity-Free Vacancy Disordering of GaAs/AlGaAs Quantum Well Structures. Semiconductor Quantum Well Intermixing. E. H. Li. Amsterdam, Gordon and Breach. **8**.
- Marsh, J. H. (2005). Multiple anneal induced disordering. **WO/2005/057638**.
- Marsh, J. H., S. I. Hansen, et al. (1991). "Applications of neutral impurity disordering in fabricating low-loss optical waveguides and integrated waveguide devices." Optical and Quantum Electronics **23**(7): S941-S957.
- McKee, A., C. McLean, et al. (1997). "Monolithic integration in InGaAs-InGaAsP multiple-quantum-well structures using laser intermixing." IEEE Journal of Quantum Electronics **33**(1): 45-55.
- Miller, S. E. (1969). "Integrated optics: an introduction." Bell Syst. Tech. J. **48**: 205969.
- Nie, D., T. Mei, et al. (2006). "Argon plasma exposure enhanced intermixing in an undoped InGaAsP/InP quantum-well structure." Journal of Applied Physics **100**(4): 046103-3.
- O. C. Zienkiewicz, R. L. T. (1996). The Finite Element Method. San Diego, Academic Press.

- Oleksandr Voznyy, R. S., Jan J. Dubowski (2006). "Multibandgap quantum well wafers by IR laser quantum well intermixing: simulation of the lateral resolution of the process." JLMN-Journal of Laser Micro/Nanoengineering **1**(1): 48-53.
- Ong, T. K. (1999). High spatial resolution quantum well intermixing process in GaInAs/GaInAsP laser structures. rd Pacific Rim conference on lasers and electro-optics. C. P. Rim"99. Seoul, Korea: 193.
- Palankovski, V., R. Schultheis, et al. (2001). "Simulation of power heterojunction bipolar transistors on gallium arsenide." Electron Devices, IEEE Transactions on **48**(6): 1264-1269.
- Palik, E. D. (1998). Handbook of Optical Constants of Solids.
- Pépin (2000). Selective Interdiffusion of GaAs/AlGaAs Quantum Wells through SiO<sub>2</sub> Encapsulation - Comparison with the Ion Implantation Approach. Semiconductor Quantum Well Intermixing. E. H. Li. Amsterdam, Gordon and Breach. **8**.
- Pépin, A., C. Vieu, et al. (1995). "Fabrication of quantum wires by selective intermixing induced in GaAs/AlGaAs quantum well heterostructures by SiO<sub>2</sub> capping and subsequent annealing." Superlattices and Microstructures **18**(3): 229-229.
- Petroff, P. M. (1977). "Transmission electron microscopy of interfaces in III-V compound semiconductors." Journal of Vacuum Science and Technology **14**(4): 973-978.
- Petroff, P. M., Y. J. Li, et al. (1991). "Nanostructures processing by focused ion beam implantation." Journal of Vacuum Science & Technology B: Microelectronics and Nanometer Structures **9**(6): 3074-3078.
- Prins, F. E., G. Lehr, et al. (1993). "Intermixed GaAs/AlGaAs quantum wires and the influence of implantation species on the steepness of the lateral potential." Journal of Applied Physics **73**(5): 2376-2380.
- Qiu, B. C., A. C. Bryce, et al. (1998). "Monolithic integration in InGaAs-InGaAsP multiquantum-well structure using laser processing." Photonics Technology Letters, IEEE **10**(6): 769-771.
- Radoslaw Stanowski, O. V., Jan J. Dubowski (2006). "Finite element model calculations of temperature profiles in Nd:YAG laser annealed GaAs/AlGaAs quantum well microstructures." JLMN-Journal of Laser Micro/Nanoengineering **1**(1): 17-22.
- Ralston, J., G. W. Wicks, et al. (1986). "DEFECT STRUCTURE AND INTERMIXING OF ION-IMPLANTED ALXGA1-XAS/GAAS SUPERLATTICES." Journal of Applied Physics **59**(1): 120-123.
- Ralston, J. D., S. O'Brien, et al. (1988). "Room-temperature exciton transitions in partially intermixed GaAs/AlGaAs superlattices." Applied Physics Letters **52**(18): 1511-1513.
- Rastelli, A., A. Ulhaq, et al. (2007). "In situ laser microprocessing of single self-assembled quantum dots and optical microcavities." Applied Physics Letters **90**(7): 073120-3.
- Ravindra, N. M., S. Abedrabbo, et al. (1998). "Temperature-dependent emissivity of silicon-related materials and structures." Semiconductor Manufacturing, IEEE Transactions on **11**(1): 30-39.
- Ravindra, N. M., P. Ganapathy, et al. (2007). "Energy gap-refractive index relations in semiconductors - An overview." Infrared Physics & Technology **50**(1): 21-29.
- Stanowski, R., S. Bouaziz, et al. (2008). Selective area bandgap engineering of InGaAsP/InP quantum well microstructures with an infrared laser rapid thermal annealing technique. Photon Processing in Microelectronics and Photonics VII, San Jose, CA, USA, SPIE.



- Stanowski, R. and J. J. Dubowski (2009). "Laser rapid thermal annealing of quantum semiconductor wafers: a one step bandgap engineering technique." Applied Physics A-Materials Science & Processing **94**(3): 667-674.
- Stanowski, R., M. Martin, et al. (2009). "Iterative bandgap engineering at selected areas of quantum semiconductor wafers." Optics Express **17**(22): 19842-19847.
- Stanowski, R., Voznyy O., Dubowski J.J. (2005). Modelling of temperature profiles in Nd:YAG laser annealed GaAs/AlGaAs quantum well microstructures. Laser Applications in Microelectronic and Optoelectronic Manufacturing X. San Jose, SPIE.
- Stanowski, V., Dubowski (2006). "Finite element model calculations of temperature profiles in Nd:YAG laser annealed GaAs/AlGaAs quantum well microstructures." JLMN-Journal of Laser Micro/Nanoengineering **1**(1): 17-22.
- Steen, M. W. (1998). Laser Material Processing. Berlin, Springer.
- Sturge, M. D. (1962). "Optical Absorption of Gallium Arsenide between 0.6 and 2.75 eV." Physical Review **127**(3): 768.
- Sze, S. M. (1981). Physics of Semiconductor Devices. New York, Wiley.
- TIEMEIJER, J. J. M. B. P. J. A. T. T. v. D. E. J. J. A. A. M. T. S. G. N. v. d. H. L. F. (1997). "Characterization of Butt-Joint InGaAsP Waveguides and Their Application to 1310 nm DBR-Type MQW Gain-Clamped Semiconductor Optical Amplifiers." IEICE TRANSACTIONS on Electronics **E80-C**(5): 675.
- Timans, P. J. (1992). "The experimental determination of the temperature dependence of the total emissivity of GaAs using a new temperature measurement technique." Journal of Applied Physics **72**(2): 660-670.
- Trivedi, D. A. and N. G. Anderson (1996). "Modeling the near-gap refractive index properties of semiconductor multiple quantum wells and superlattices." Selected Topics in Quantum Electronics, IEEE Journal of **2**(2): 197-209.
- Turner, W. J., W. E. Reese, et al. (1964). "Exciton Absorption and Emission in InP." Physical Review **136**(5A): A1467.
- Vieu, C., M. Schneider, et al. (1991). "Optical characterization of selectively intermixed GaAs/GaAlAs quantum wires by Ga[<sup>+</sup>] masked implantation." Journal of Applied Physics **70**(3): 1444-1450.
- Voznyy, S., Dubowski (2006). "Multibandgap quantum well wafers by IR laser quantum well intermixing: simulation of the lateral resolution of the process." JLMN-Journal of Laser Micro/Nanoengineering **1**(1): 48-53.
- Wallin, J., G. Landgren, et al. (1992). "Selective area regrowth of butt-joint coupled waveguides in multi-section DBR lasers." Journal of Crystal Growth **124**(1-4): 741-746.

# Chapter 3

## Infrared Laser Rapid Thermal Annealing Experimental Details

In this chapter I describe both the studied QS wafers and the Infrared (IR) continuous wave (CW) laser rapid thermal annealing (Laser-RTA) setup that has been designed to carry out selective area annealing and QWI of the QS wafers.

### 3.1 QS microstructures

#### 3.1.1 AX04-182

The AX04-182 QW microstructure presented in figure 3.1.1 was received from prof. C. Jagadish group from University of Canberra. AX04-182 contains two shallow QWs in about 50 nm and 75 nm distances from its surface. The wafer has been grown by molecular beam epitaxy (MBE) technique. The slab diagram is presented in figure 3.1.1 (a). The deeper 7 nm thick GaAs QW was confined between 10 nm and 100 nm thick  $\text{Al}_{0.5}\text{Ga}_{0.5}\text{As}$  barriers. The other, 3 nm thick GaAs QW with 10 nm  $\text{Al}_{0.5}\text{Ga}_{0.5}\text{As}$  barriers was located above and capped with a 50 nm thick GaAs layer. The investigated material included a 200 nm GaAs buffer layer and was 371  $\mu\text{m}$  thick in total. The PL spectrum of as-grown material is presented in figure 3.1.1 (b). It demonstrates that the PL signal from the 3 nm thick shallow QW ( $\lambda = 780 \text{ nm}$ ) was not detectable at room ambient conditions. This suggests that the majority of the photo-excited electrons in the 3 nm thick QW were tunnelling through the 10 nm AlGaAs barrier and trapped by the 7 nm thick QW where they recombined ( $\lambda=819 \text{ nm}$ ).

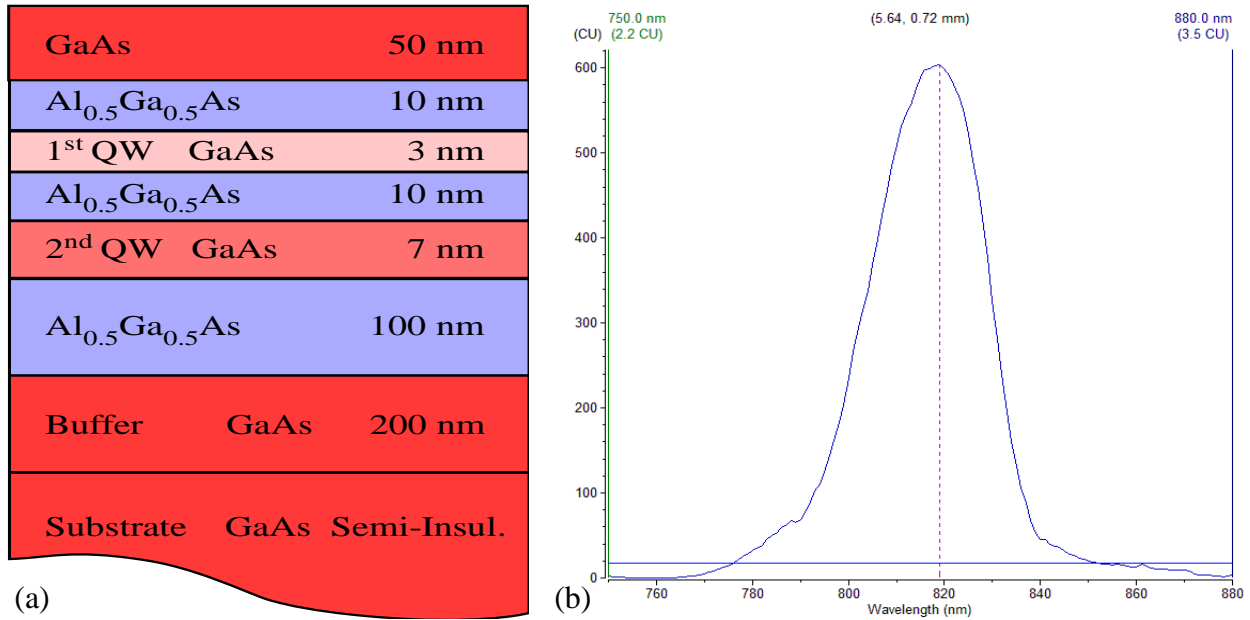


Figure 3.1.1 Slab diagram of AX04-182 wafer microstructure (a) and its PL spectrum in range 750 – 880 nm (b).

### 3.1.2 RA30360

RA30360 is an InP-based QWs microstructure presented in figure 3.1.2. The QW wafer was received from Richard Arès' group from University of Sherbrooke. The InGaAs/InGaAsP microstructure consisted of 5 QWs (6 nm thick InGaAs) and 4 barriers (10 nm thick InGaAsP) material. The topmost QW was coated with approximately 10 nm thick barrier material of InGaAsP and a 70 nm thick InP cap. Both the QWs and barriers were n-type (Si doped at  $8 \times 10^{17} \text{ cm}^{-3}$ ). The microstructure was grown on a 0.375 mm thick InP wafer. The InGaAsP/InP samples used for determination of the transient temperature behavior and that were used for writing an array of parallel lines of the QWI material had dimensions of 10 mm x 14 mm x 0.375 mm. Samples were capped with PECVD 270 nm thick SiO<sub>2</sub> layers on the polished (front) side, and with 740 nm SiO<sub>2</sub> on the back side. Optical reflection measurements carried out for InGaAsP/InP wafer at 1064 nm have shown that the reflected power decreased from 37 % for a bare wafer down to 10 % for the InGaAsP/InP wafer coated with 264 nm thick SiO<sub>2</sub> layer.

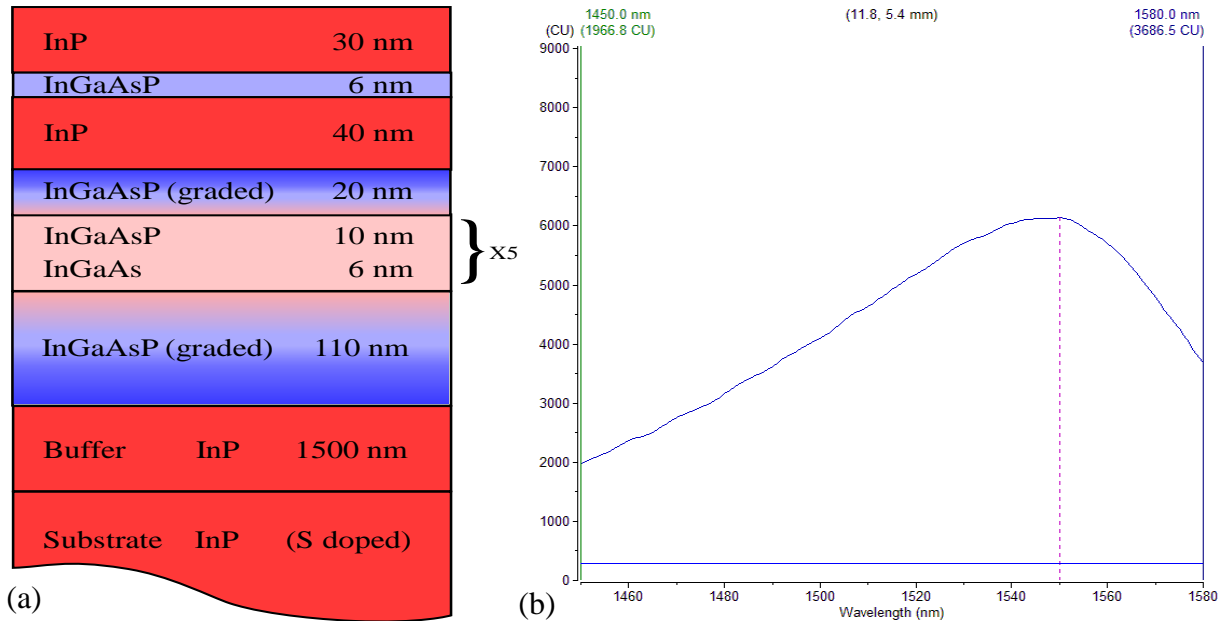


Figure 3.1.2 Slab diagram of RA30360 wafer microstructure (a) and its PL spectrum in range 1450 – 1580 nm (b).

### 3.1.3 02-161

02-161 is an InP-based QDs microstructure received from Philip Poole at the National Research Council Canada in Ottawa. The microstructure has been grown by chemical beam epitaxy (CBE) technique at 510°C and pressure of 5e-6 Torr. The source materials were trimethyl-indium (TMI) for the indium source. For the group V source we use arsine (AsH<sub>3</sub>) and phosphine (PH<sub>3</sub>) that are precracked in a high temperature gas cell as they enter the growth chamber to produce As<sub>2</sub> and P<sub>2</sub>. The dot size is typically 30 nm in diameter. The dot density is approximately 320/um<sup>2</sup>. This is the surface dot density, and the assumption is that the buried layer is the same. The undoped structure has been grown on 001 oriented InP substrate, so the InAs 3.3ML layers were slightly strained up to -3.1% to InP layers. The PL peak position of the as-grown material was measured at 1500 nm in a Philips PLM-150 industrial PL mapper. The dimensions of the processed sample were 200 x 10 x 0.4 mm. For the Laser – RTA process carried out at room ambient sample was capped with 500 nm SiO<sub>2</sub> on the back side ( unpolished ) and with the 50 nm SiO<sub>2</sub> cap on the top side ( polished ) to prevent decomposition of the sample during the annealing process and as well to promote the quantum dot intermixing process.

### 3.2 Conventional – RTA QWI

The thermal stability of AX04-182 microstructure has been tested in a commercial Jipelec rapid thermal processor furnace. Test samples had 5 x 5 mm dimensions. I have executed several series of RTA treatments for various processing times and temperatures. The corresponding results are presented in figure 3.2.1. During the processing the as-grown AX04-182 samples were placed on the 4" Si wafer-holder with their polished sides down – in contact with the Si wafer. Their tops (unpolished sides) were capped with small fragments (6 x 6 mm) of Si wafer. The RTA chamber was flushed with nitrogen during the processing. The studied QWs material system proved to be thermally stable up to 900 °C. Processing at 750, 800 and even 850 °C resulted in negligible shift of emission wavelength peak position. The efficient intermixing took place in samples tested at 900 and 950 °C and processing times longer than 20 s. The AX04-182 material proved difficult to intermix in the conventional RTA processor. Processing at 950 °C for times longer than 160 s could damage the thermocouple sensor installed in RTA chamber that was responsible for the RTA process temperature control.

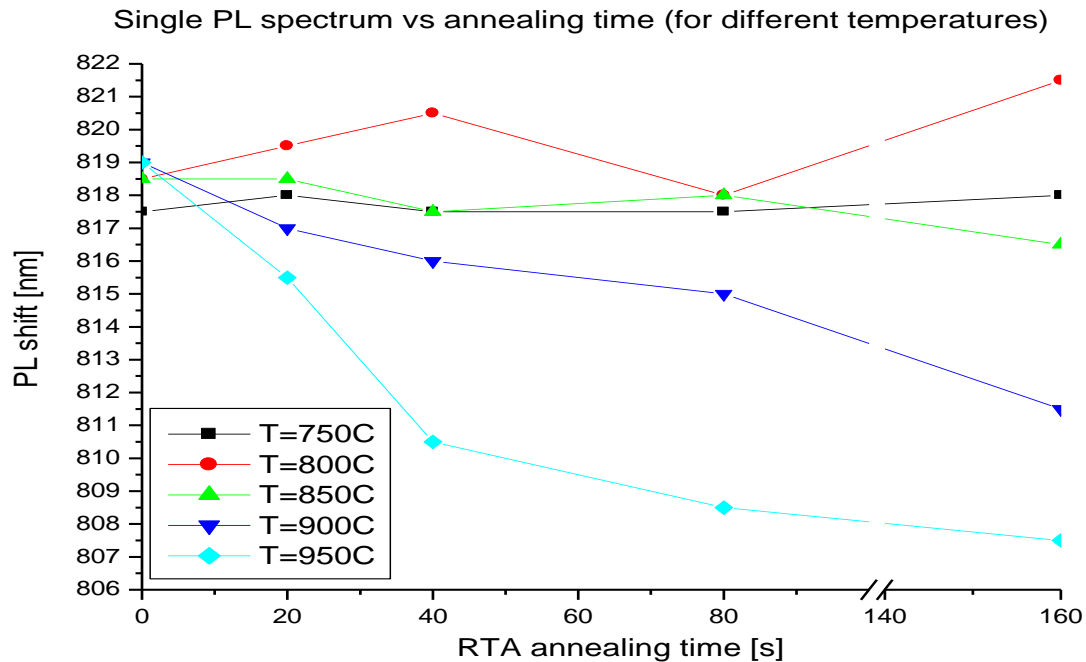
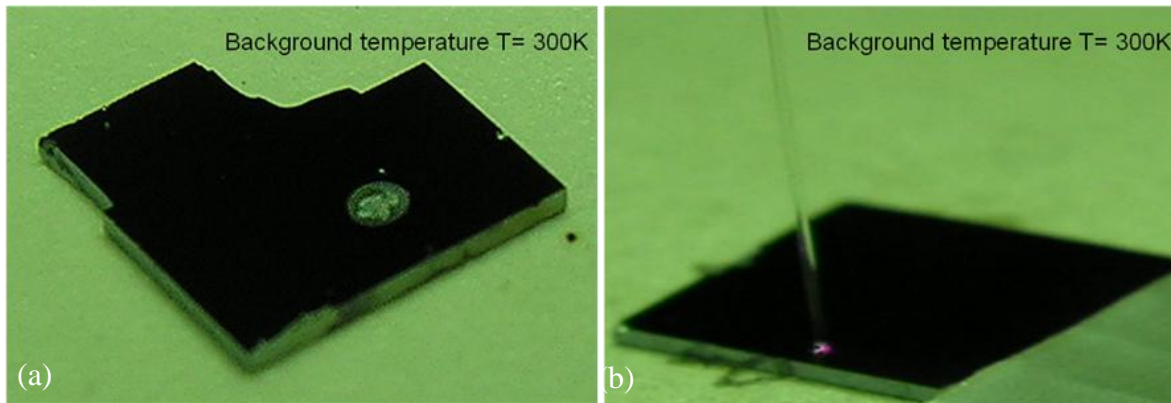


Figure 3.2.1 Conventional rapid thermal annealing of AX04-182 induced QWI corresponding shift of the PL peak position.

### 3.3 Laser – RTA Surface Damage Test



**Figure 3.3.1 Laser - RTA test of surface damage threshold**

I have studied the surface damage conditions on AX04-182 microstructure coated with SiO<sub>2</sub> on both top and bottom surfaces. Samples were irradiated with various laser beam diameters, power densities and background temperatures. The results are gathered in the table 3.3.1. Wafers were irradiated through optical fibers of 0.05, 0.7 and 1 mm core diameters. The results indicate that the surface damage does not depend on the delivered laser power density but strongly depends on the total laser power delivered. This could be explained by the efficiency of heat conduction of the irradiated material e.g. the density of 7.003 W/mm<sup>2</sup> delivered to the 0.785 mm<sup>2</sup> surface caused the surface damage presented in figure 3.3.1 (a) while the tiny laser spot of the 0.002 mm<sup>2</sup> surface could withstand the 152.8 W/mm<sup>2</sup> laser power without observed surface damage presented in figure 3.3.1 (b).

**Tableau 3.3.1 Results of the Laser - RTA induced surface damage threshold**

Background temperature	300K	300K	700K	700K	300K	300K
Fiber diameter [mm]	1	0.365	1	0.365	0.05	0.05
Fiber core Surface [mm <sup>2</sup> ]	0.785	0.104	0.785	0.104	0.002	0.002
Delivered Laser Power [W]	5.5	2	4	2	0.3	4
Delivered Laser Power Density [W/mm <sup>2</sup> ]	7.003	19.11	5.09	19.12	152.8	2038
SURFACE EFFECT	Burn	Burn	Burn	Burn	No burn	Brun

### 3.4 Setup description

A schematic diagram of the Laser-RTA setup is shown in figure 3.4.1. It consists of a sample holder, two high power (class IV) IR laser irradiation sources, temperature diagnostics and process monitoring units.

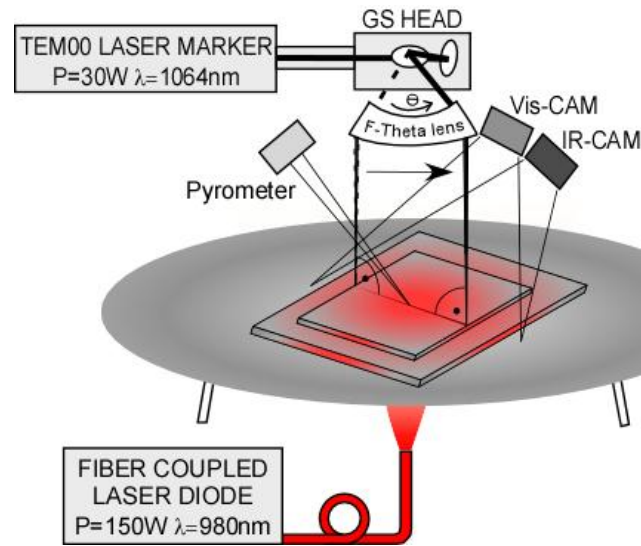
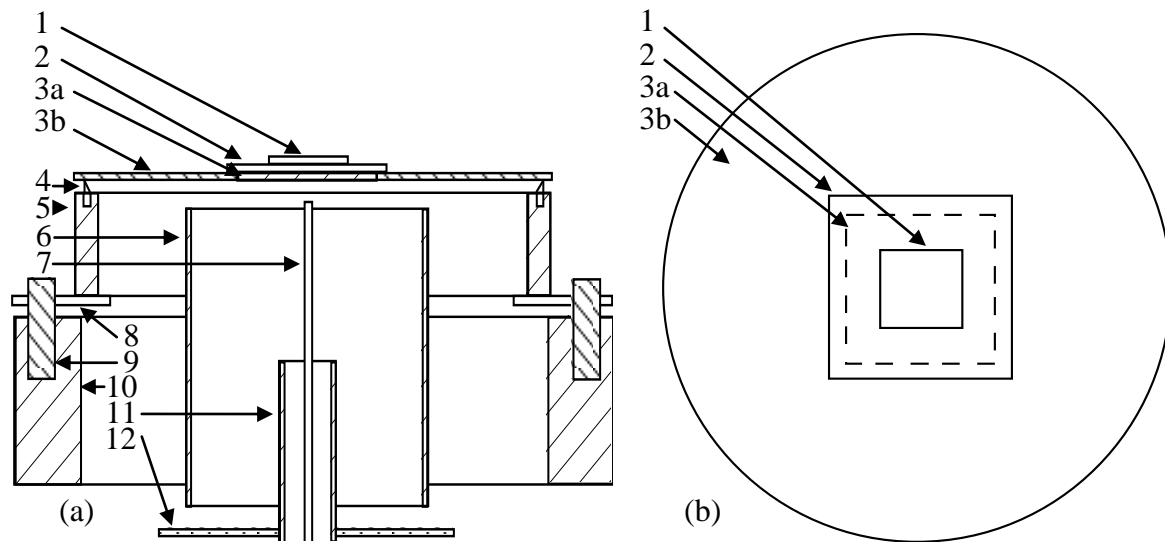


Figure 3.4.1 Schematic diagram of the infrared laser rapid thermal annealing experimental setup

#### 3.4.1 Sample holder

The sample holder was used to isolate the processed sample from ambient temperature. Typically, during the Laser – RTA processing, the InP and GaAs based wafers have to be heated up to 700 and 900 C, respectively, while the temperature of the setup must be maintained at near 25 °C. Therefore it has been necessary to design a sample holder that could withstand these extreme temperature gradients, last for many processing cycles and allow for in-situ temperature diagnostics with the infrared pyrometer and custom made camera. One of the requirements of the sample holder was to allow for processing of samples of various dimensions, from 5 mm x 5 mm, to full size wafers of minimum 50 mm in diameter. The schematic cross-section of the sample holder is presented in figure 3.2.2. The sample (1) with its polished side up is located on a 20 mm x 20 mm x 0.375 mm Si wafer (2) that is situated with its unpolished side up. This is to assure a strong optical contrast against the surface of processed wafers. The Si wafer is directly irradiated with the LD beam and serves as a hot-plate for the processed samples.



**Figure 3.4.2 Cross-section (a) and top view (b) of the sample holder 1 – sample; 2 – Si wafer; 3a – opening in a graphite plate; 3b – graphite plate; 4 – fused silica spacer; 5 – Al 2'' ring; 6 – stainless steel ring; 7 – laser diode fiber; 8 – fused silica rod holder; 9 – Al support pin; 10 – Theta circular motor; 11 – fiber housing; 12 graphite ring beam stopper**

The energy from the LD beam is fully absorbed and homogenized within the silicon substrate. The silicon wafer is situated on top of a 2 inch in diameter graphite plate (3b) with a 10 mm x 10 mm opening (3a). For high temperature processing, it is important to isolate the processed sample from ambient to assure that the laser induced temperature temporal behaviour will depend on the sample's material thermal properties such as absorption, emissivity, heat capacity and heat conduction. Proper thermal isolation from ambient has been achieved by two sets of fused silica spacers (4) and (8) providing two efficient thermal isolation stages with convection air flow cooling system. This allows observing experimentally the predicted in FEM model calculations temporal temperature behaviour in the middle of laser irradiated spot. The precision of estimation of the required processing time and temperature components dictates the spectral emission wavelength tuning accuracy. A top view of the graphite plate with opening, the silicon sample holder and the sample are shown in figure 3.4.2b. The silicon wafer that supports directly the processed sample and itself is positioned on a graphite plate with an opening for LD radiation access. The sample holder provides an excellent temperature blocking efficiency. For instance, during processing of GaAs wafers for the period of 5 min. at 900 C, the temperature of theta circular motor increased from 23.8 to 24.2 C.



### 3.4.2 CW laser diode

Figure 3.4.3 presents the picture of the Apollo Instruments Inc. LD unit employed in the Laser – RTA setup. A fiber pigtailed ( 1 mm core, NA = 0.22, 2 m long) CW GaAs / AlGaAs laser diode ( LD ) unit operates at 980 nm and delivers regulated power of up to 150 W. The spot diameter on the sample can be regulated between 2 and 25 mm by changing the distance of the fiber tip from the irradiated surface. The role of LD is to increase the wafer background temperature to near the QWI threshold. This turnkey laser system is water-cooled in closed circulation and delivers lasing intensity that is stable over time. Its power can be regulated using its front panel buttons, however I have developed a LabVIEW based remote interface to control its lasing power using a computer. Additionally for the Laser – RTA fully automated processing I have developed a feedback loop routine allowing to maintain the processing temperature at desired levels. The lasing power is automatically adjusted in respect to the setup pyrometer’s temperature value readout. In the Laser – RTA setup the LD fiber is situated underneath the silicon wafer as demonstrated in figure 3.4.2 (7, 11) at normal angle to the silicon wafer to maintain the symmetrical beam density distribution at the projected spot.



Figure 3.4.3 Apollo Instruments Inc. CW,  $\lambda=980$  nm, fiber pigtailed laser diode [Apollo\_Instruments\_Inc,].

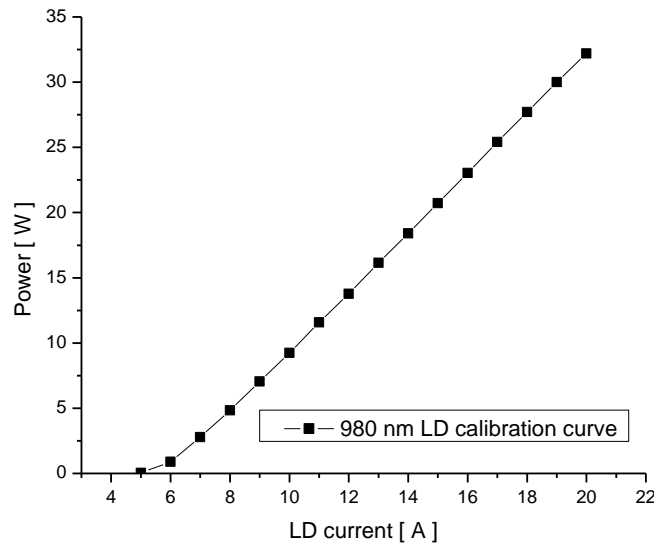


**Figure 3.4.4** The GaAs/AlGaAs  $\lambda=980$  nm CW LD output power [W] vs power supply current [A] dependence curve.

Figure 3.4.4 shows the output power of the LD in function of the diode driving current [A]. It demonstrates linear dependence between the power supply current and the lasing output power for the power supply current values in range between 7 – 22 A. This unit is able to deliver 150 W of optical power for what it requires 40 A of power supply current, however for the Laser – RTA processing of QW wafers we have been using LD power of up to 35 W.

### 3.4.3 Quantronics Q-Mark Condor system

The second laser source is a Quantronics Q-Mark Condor CW, Nd:YAG, TEM00 laser operating at  $\lambda=1064$  nm and delivering regulated power of up to 20 W to a spot of 100  $\mu\text{m}$  in diameter (see figure 3.4.5). The Nd:YAG laser spot diameter can be increased by increasing the distance between the sample and the focal plane. This unit is capable to carry out metallic surfaces marking, scribing and engraving, requiring much higher power intensities than these used for selective area heating without introducing a surface damage of the semiconductor wafers. To obtain stable output power values in the range of 0.8 – 1.6 W, I have adjusted the working point of the system by introducing a 50/50 % beam splitter.



**Figure 3.4.5 Quantronix Condor Nd:YAG laser marker processing unit [Quantronix]**

The beam splitter and a thermally isolated graphite plate for absorbing the splitted portion of the beam were installed behind the lasing mirror inside the main laser chassis. The presented laser marker system equipped in a galvanometric scanner (GS) can raster the Nd:YAG laser beam over the sample with a controlled velocity of 1 – 4000 mm/s.

The position of the 1064nm Nd:YAG beam could be indicated with a low power 632 nm pilot laser diode installed inside the galvo-scanner (GS) head. The dependence of the Nd:YAG laser optical output power [W] on the power supply current [A] is presented in figure 3.4.6.

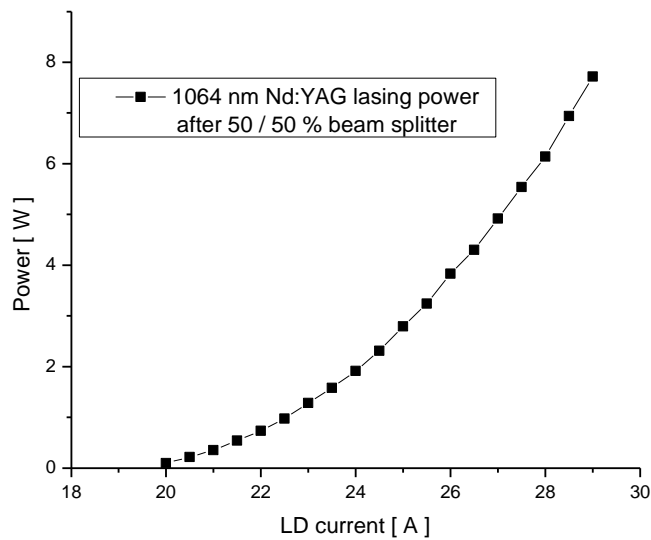


**Figure 3.4.6 Nd:YAG 1064 nm CW laser output power after 50/50 % beam splitter [W] vs power supply current [A] dependence curve.**

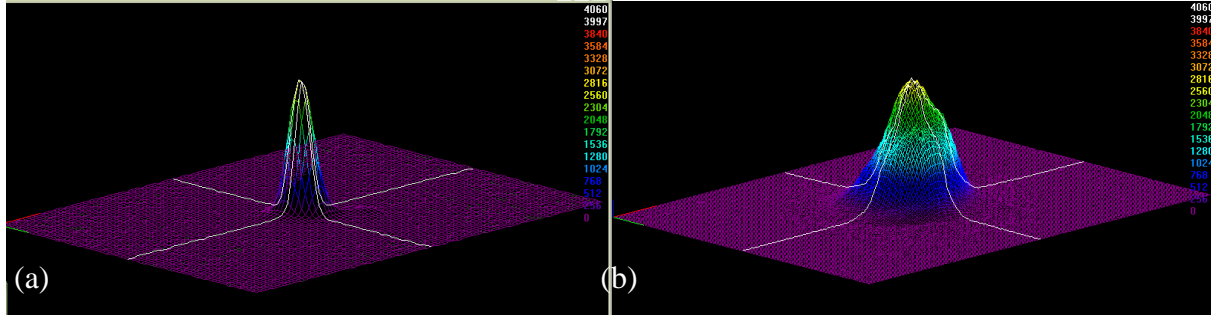


**Figure 3.4.7 The 100  $\mu\text{m}$  (a) and 500  $\mu\text{m}$  (b) according to  $4\sigma$  criterion Nd:YAG laser beam profiles measured with LBA-FW Ophir - Spiricon Inc. beam profiler.**

An F-Theta lens installed at the output of the GS head allows to deliver same intensity profile laser spots to any site of 2 inch diameter wafers placed at the focal distance of that lens. Examples of the intensity profiles for 100 and 500  $\mu\text{m}$  spots are shown in figure 3.4.7. The Nd:YAG laser beam intensity profiles have been investigated with an Ophir-Spiricon profiler (Model LBA-FW). It is clearly visible that the 500  $\mu\text{m}$  beam is deformed from a TEM00 mode towards a multimode beam with slightly off-center peak position of the maximum intensity values. For the automated Laser – RTA precise processing dwell times accuracy control I have developed a LabVIEW interface to command the GS mirrors position.

The Laser-RTA setup has been situated on an optical table equipped with air based vibrations reductions system presented in figure 3.4.8. This system can be used in two processing modes:

1. Processing of samples with a moving Nd:YAG laser beam,

A galvanometric scanner (GS) can raster the Nd:YAG laser beam over the sample with a controlled velocity of 1–4000 mm/s. An F-Theta lens mounted at the output of the GS head assures that a beam with the same profile is delivered to any site of the wafer surface.

2. Processing with a steady Nd:YAG beam of samples installed in an XY table that allows changing their position against the laser beam.

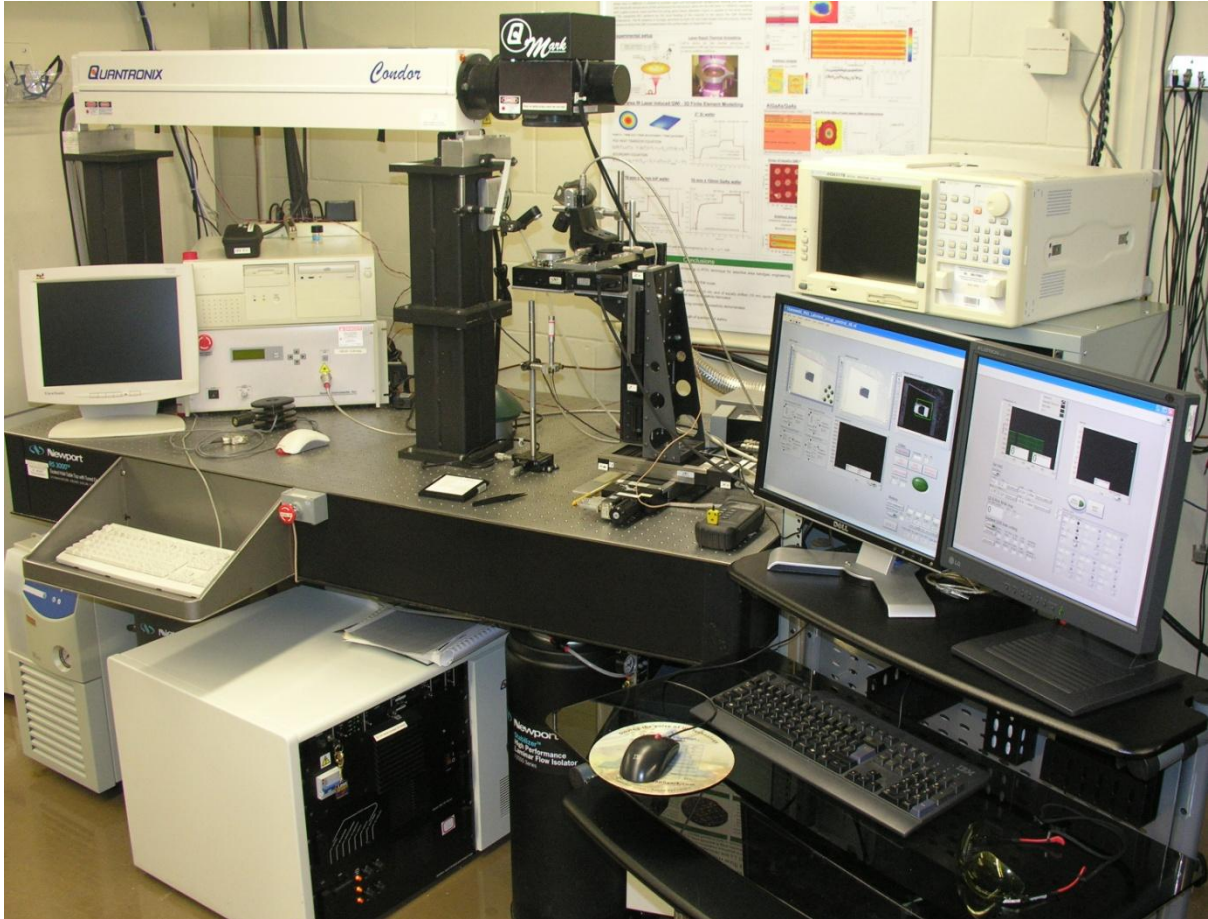


**Figure 3.4.8 Photo of the developed Laser - RTA setup**

The sample holder has been positioned on three commercially available Newport Inc. linear X, Y and Z motorized stages that offer 250 mm traveling distance in X and Y directions and 150 mm in Z direction with a 1  $\mu\text{m}$  resolution while traveling over a certain distance and one Theta motor that can rotate the sample's position with a 0.0005 deg resolution. The movement of these four motors has been controlled with the custom designed LabVIEW based interface and Newport Universal Motor Driver UniDrive6000 controller

### 3.4.4 MIKRON M680 pyrometer

The temperature of the sample was monitored with a MIKRON M680 single color pyrometer. The pyrometer assembly parts are presented in figure 3.4.9. It consists of the infrared sensor unit, fused silica, multimode (1 mm core) optical fiber that transmits the blackbody radiation focused with a lens assembly. The pyrometer sensor is equipped with two channels working at  $\lambda = 900$  nm and  $\lambda = 980$  nm respectively. It is capable of collecting radiation from circular areas of 0.4 and 0.7 mm in diameter and focal distances of 45 and 55 mm respectively from channel 1 and 2 respectively. Transient temperature behaviour at selected spots irradiated with the laser was carried out at the rate of 10 Hz. The minimum temperature that could be monitored with the pyrometer is about 435°C.

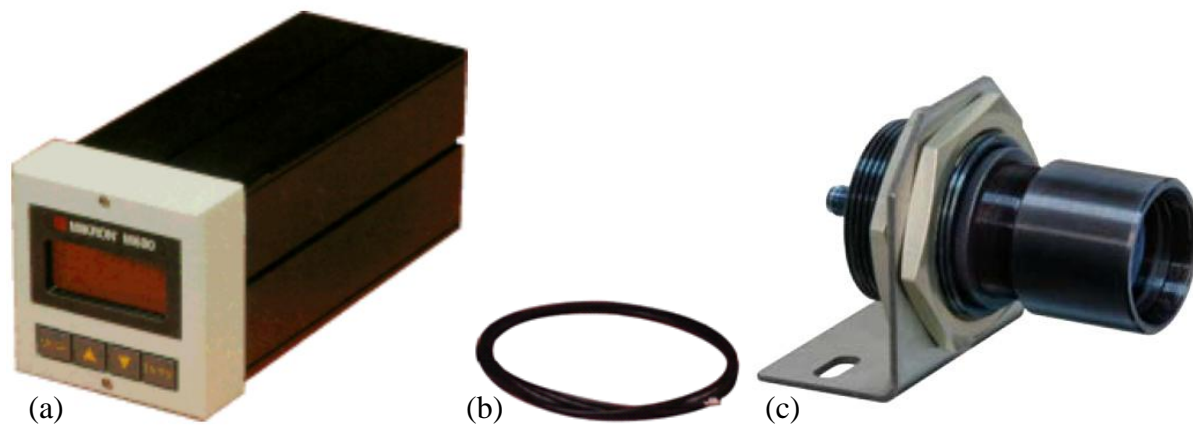


**Figure 3.4.9** Mikron pyrometer set. Infrared sensor unit (a), connecting optical fiber (b), lens assembly (c) [Mikron\_Infrared\_Inc].

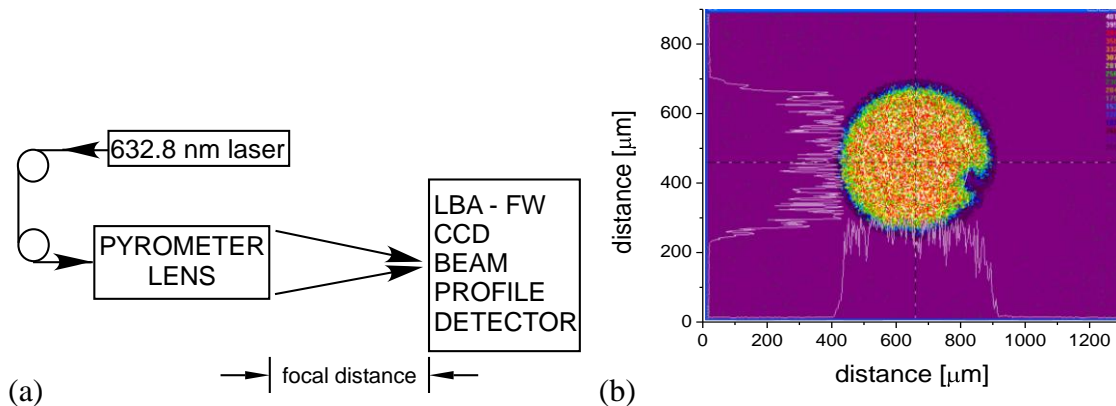


**Figure 3.4.10 Mikron M680 radiation collection spot. Measurement setup (a). Measured profile (b).**

The diameter of the collecting spot was determined with the Ophir - Spiricon Inc. LBA – FW system equipped with a 1.5 m collecting fiber and a CCD camera. A schematic idea of the spot characterization setup and the result obtained for HeNe laser spot are presented in figure 3.4.10 (a) and (b) respectively. The 632.8 nm laser radiation has been sent through the pyrometer’s optical radiation collection fiber and lens assembly ( $f = 45 \text{ mm}$ ), and its focused spot has been directly projected on the CCD camera at normal angle. The measured profile shows flat intensity distribution over the circular area of  $453 \text{ }\mu\text{m}$  in diameter. This indicates that during the temperature measurement the information about the pyrometer collected sample’s temperature distribution is averaged in the pyrometer’s optical fiber due to multiple internal reflections. The pyrometer detects the average energy from the spot, without resolving the information about temperature variation within the monitored spot. To take advantage of the temperature measurements provided by this pyrometer, dedicated experiments had to be carried out with the  $500 \text{ }\mu\text{m}$  spot of the Nd:YAG laser. During the Laser – RTA processing the pyrometer’s head is installed at  $40 \text{ deg}$  angle to the normal of the sample. This results in elongation of the pyrometer’s measuring spot to the ellipsoidal shape of about  $450 \text{ }\mu\text{m}$  by  $600 \text{ }\mu\text{m}$ . To achieve reproducible QWI results, it has been necessary to assure uniform and controlled background temperature distribution across the processed sample induced with LD laser before projection of the Nd:YAG processing laser beam.

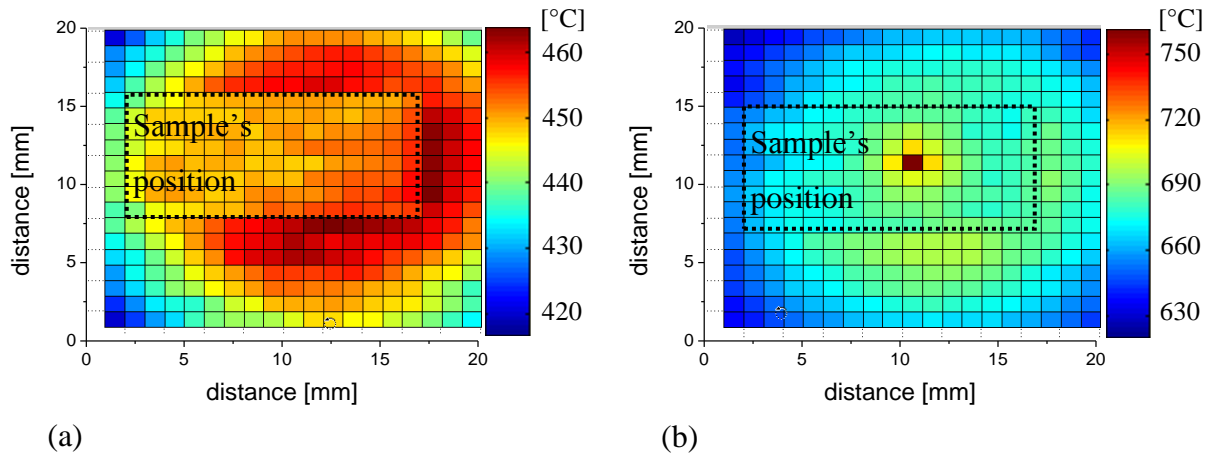


**Figure 3.4.11 Temperature maps of the Laser – RTA processed AX04-182 wafer irradiated with (a) LD only and (b) LD and Nd:YAG laser beams.**

Examples of the temperature distribution maps of 25 mm x 25 mm Si wafer supporting a 8 mm x 15 mm AX04-182 sample, irradiated with LD only and LD combined with Nd:YAG laser beams, are presented in figure 3.4.11 (a) and (b), respectively. The maps were collected using the pyrometer lens assembly installed on a motorized X, Y stage. The location of the sample is indicated by dashed-line rectangles. The temperature map has been collected with 1 mm step-resolution. It can be seen that a non-symmetric position of the LD spot with respect to the center of the sample, has resulted in non-uniform temperature distribution across the sample, ranging, left-edge to the right-edge, from 443 to 454 °C. Such temperature distribution, clearly dependent on the position of the sample on the supporting Si wafer, was responsible for the difficulty of obtaining same processing temperature at various areas of different samples. The temperature mapping using the single spot pyrometer approach, although not attractive for practical applications due to the extended collection times (typically, it took 10 min to collect either of the maps shown in figure 3.4.11). This indicates the importance of a diagnostic tool capable of rapid collection of temperature maps that would be useful for real-time adjustment of sample's position.



### 3.4.5 Custom designed infrared camera (IR-CAM)

I have modified a webcam camera (Pine, Model: PC-30C 6028 [4]) for collecting thermal maps of laser heated wafers (IR-CAM). The modification concerned removing an infrared filter from the webcam and installing a narrow band filter (Edmund Scientific, Model: 64326-66227) allowing 45 % transmission in the 820 – 840 nm spectral range. The IR-CAM was situated in the setup at 45 degrees angle to the wafer's substrate. Its field of view covered 70 mm x 10 mm area. This means that at 640 x 480 pixels resolution mode, one pixel could read the black-body radiation from the area of about 0.15 mm x 0.15 mm. With custom LabVIEW code the IR-CAM reads the temperature maps at rates of 10 and 15 frames per second for 640 x 480 and 320 x 240 pixels resolution modes, respectively. The device is shown in figure 3.4.12. The spectral collection window has been increased ten times to 20 nm, comparing to 2 nm of the Mikron M680 pyrometer, because the black-body radiation signal collection area measured by a single IR-CAM pixel is of 150 x 150  $\mu\text{m}$  and has been decreased by 7 times comparing to 450  $\mu\text{m}$  in diameter area measured by Mikron M680 pyrometer.

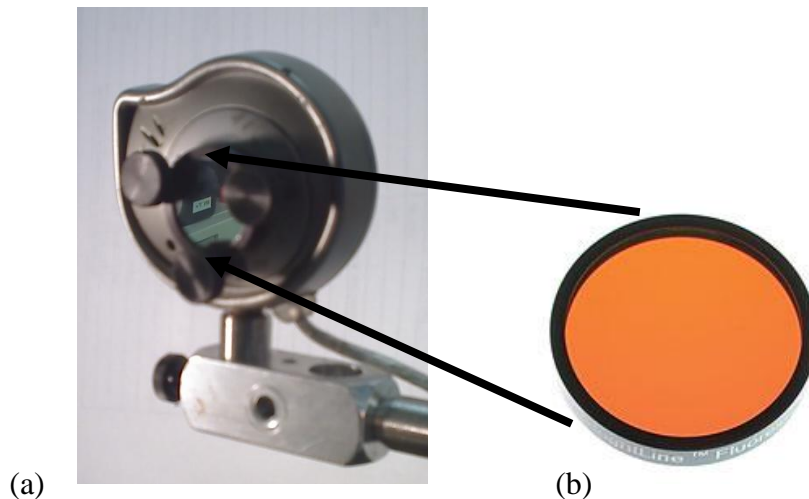


**Figure 3.4.12 Custom designed IR-CAM assembly elements. Standard USB interfaced 'Pine' webcam (a) and 820 – 840 nm infrared bandpass filter (b) [Pine].**

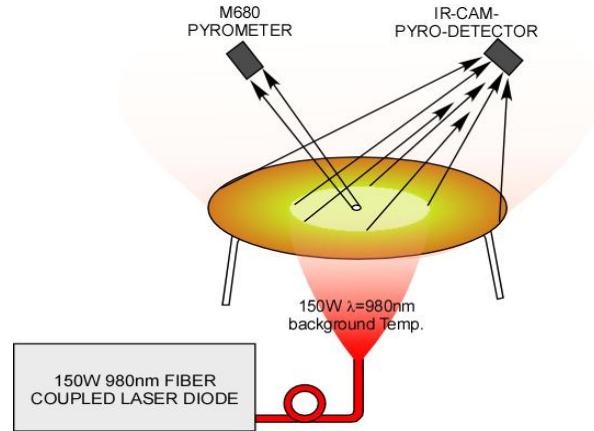


**Figure 3.4.13 Schematic diagram of the IR-CAM calibration setup**

The minimum temperature that could be monitored with this instrument was about 380°C. This spectral region excludes the 980 nm and 1064 nm laser sources as well as the InP and GaAs based QW/QD PL signal once they are heated to above 300°C. The IR-CAM band-pass filter eliminates also the influence of the fluorescent light laboratory ambient illumination wavelengths. The schematic diagram presented in figure 3.4.13 presents the IR-CAM calibration setup.

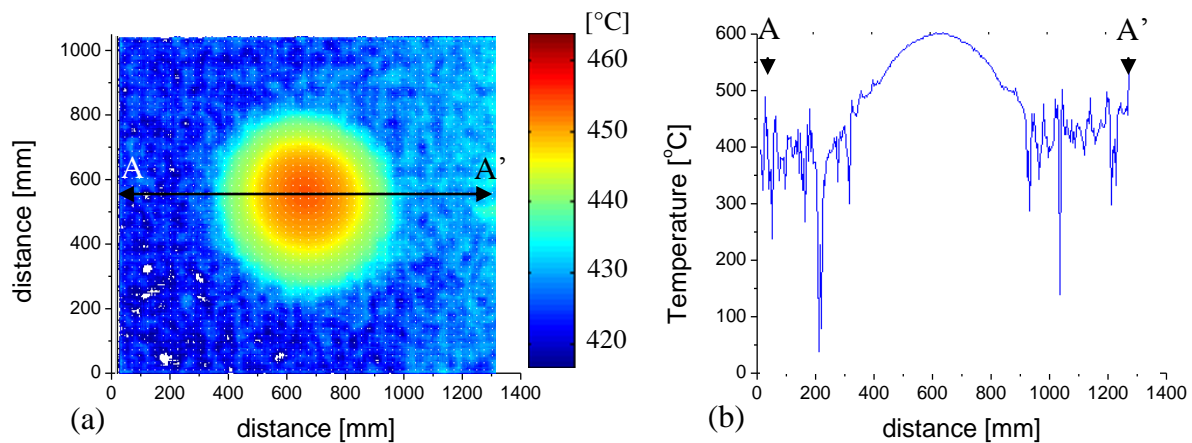


**Figure 3.4.14 IR-CAM temperature distribution map of 2'' Si wafer irradiated with LD 980 nm beam (a) and its cross-section plot (b)**

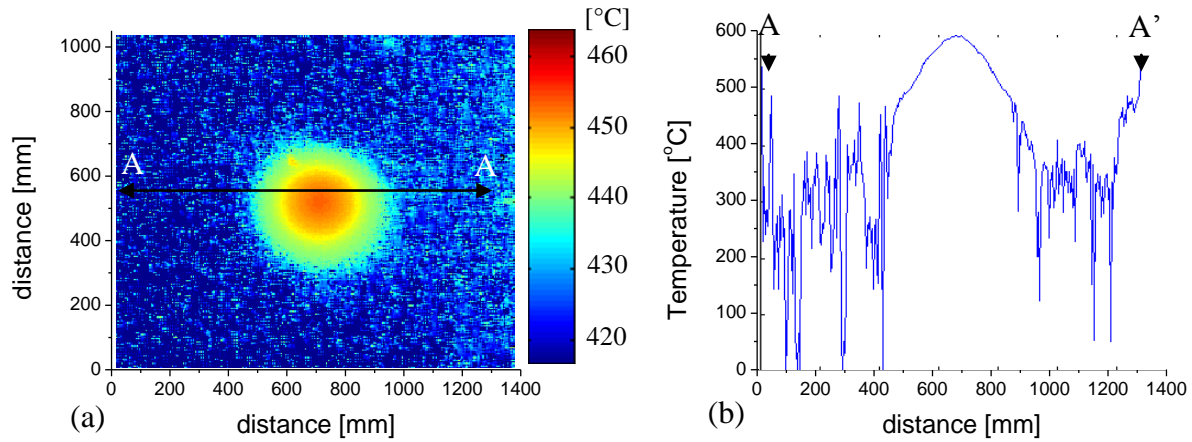


**Figure 3.4.15 IR-CAM temperature distribution map of 2" GaAs wafer irradiated with LD 980 nm beam (a) and its cross-section plot (b)**

This IR-CAM camera temperature values have been calibrated with the M680 pyrometer detecting temperature values during the irradiation of 2" Si and GaAs wafers with a 45 mm diameter LD spot. The example of two background temperature maps are presented in figures 3.2.14 and 3.2.15 for 2" Si and GaAs wafers respectively. The LD beam was used to irradiate the back side (unpolished) of both Si and GaAs wafers. It required 61 and 40 W to achieve the maximum temperature of 600 °C on the Si and GaAs wafer, respectively. In principle, the IR-CAM works as a multichannel pyrometer and it has been designed for quick measurements of the temporal surface temperature profiles behavior on the whole processing area, however at room temperature the IR-CAM can be also used to monitor the low intensity LD 980 nm

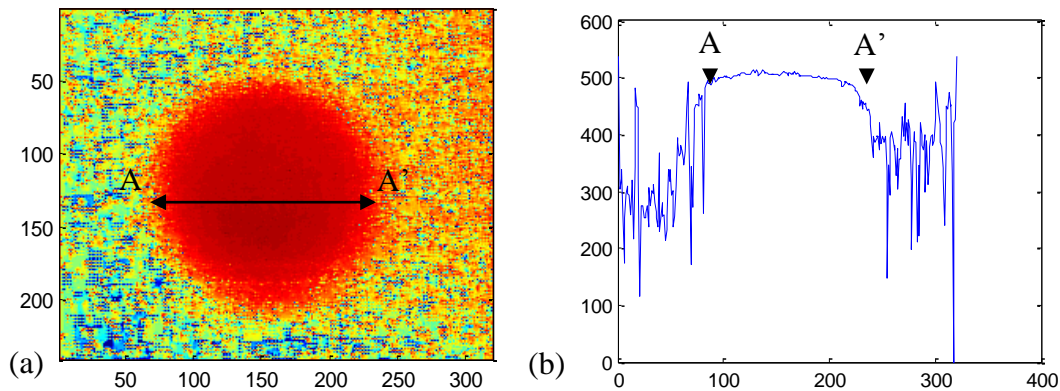


**Figure 3.4.16 LD 980 nm beam transmission intensity through a 2" Si wafer map (a) and cross-section profile (b)**

radiation transmission profile through transparent Si, GaAs or other semiconductor wafers. An example of registered LD laser beam transition profile through the 2" Si wafer is presented in figure 3.4.16. The beam intensity is homogenized by the Si wafer LD (P = 2 W; diameter = 5 cm) beam intensity distribution. The background color corresponds to the noise of the un-cooled IR-CAM CCD detector. The IR-CAM may be used to verify and adjust both the diameter and the position of the LD beam projected on the processed sample. Additionally, the IR-CAM has been used as the infrared laser beam detector during testing of the Laser – RTA setup for verification of presence of any 980 and 1064 nm radiation leaks from the sample's holder installed in the Laser – RTA setup. An inherent noise of the inexpensive webcam CCD detector restricted the usable temperature range of the IR-CAM to 380 - 650°C, which is sufficient to monitor IR LD induced temperature distribution. To measure temperatures above 650°C it is necessary to use an additional OD=1 or higher OD filters.

### **3.4.6 Process monitoring camera**

To monitor the experiment employing two high-power infrared lasers that emit at 980 and 1064 nm wavelengths, which are invisible to the human eye, I have installed a Si based camera (VIS-CAM) that is capable of detecting and monitoring the processing position of the 980 and 1064 nm laser beams. The measurement is based on a commercially available webcam (Rocketfish, Model: RF-WEB2C [5]) presented in figure 3.4.17. It is equipped with 2 MP un-cooled CCD silicon based sensor capturing video stream with resolution up to 1600 x 1200 pixels at rate up to 30 frames per second. The list of the camera video stream collection modes is shown in table 3.4.1.



**Figure 3.4.17** Commercially available 2MP ‘Rocketfish’ webcam used for process monitoring and sample repositioning [Rocketfish].

Its lens has a built-in autofocus mechanism and offers a manual focus adjustment mode. Its software interface offers also 4 times digital zoom function. The remote observation of the Laser – RTA process advancement is of particular importance because it eliminates the risk of operator’s error and offers the laser affected zone monitoring during the experiments with moving Nd:YAG laser beam. Additionally the custom LabVIEW interface can be used for alignment of the LD 980 nm, Nd:YAG 1064 nm infrared lasers versus MIKRON M680 pyrometer’s position. and can also be used for in-situ estimation of the Nd:YAG laser processing spot diameter.

**Table 3.4.1** Vis - CAM video stream collection modes.

Video mode	Camera resolution (pixels)
0	640 x 480
1	800 x 600
2	1600 x 1200
4	320 x 240

### 3.5 Photoluminescence mapping

The PL maps of investigated samples were collected with Philips SPM-200 and PLM-150 industrial PL mappers. The SPM-200 allows for direct access to the sample during the PL map collection. The main difference between the SPM-200 and PLM-150 mappers lie with both the excitation laser beam delivery path and technique of PL signal detection. In the case of SPM-200 the laser beam is projected on the measured sample at normal angle through a lens that serves also for the PL signal collection, contrary to the PLM-150 mapper in which the exciting laser beam is projected at some angle to the sample's surface and the photo-excited radiation is collected by a dedicated lens. Regarding the difference in the PL signal collection technique, the SPM-200 PL signal is detected through a single photodiode on which the resolved spatially PL signal spectrum is projected with 1nm resolution steps by rotation of a diffraction grating. In the case of the PLM-150 mapper the collected and spatially resolved PL signal is projected at once on an array of photodiodes. The difference in the detection technique of the photo-excited sample's response makes in average the PLM-150 mapper system about 15 times faster than the SPM-200 system, however the user has to pay a particular attention to the Z distance adjustment in the PLM-150 mapper since a deviation from the focal position translates into deviation from the calibrated wavelength values, approximately at the rate of 1 nm per 30  $\mu\text{m}$  Z distance change. To avoid this error user should always carefully verify the Z – focal position. The SPM-200 and PLM-150 interface software offers the extraction the peak wavelength position from the collected PL maps, as well as the full width at half maximum and the intensity distribution maps. This interface also allows for the verification of the single spectrum of any measured spot once the PL map has been collected. It offers also the conversion of data files into ASCII format, which I have used to carry out Matlab based data analysis. This allowed combining the sample's spatial intensity distribution maps with the corresponding PL signal peak wavelength position. The open architecture of the SPM-200 mapper allowed me to install a small electric heater for changing the sample temperature and carry out test-study of PL peak position at elevated temperatures.

### 3.6 Laser – RTA processing methodology

The Laser-RTA process flow is schematically shown in figure 3.6.1. It is important to follow the steps indicated by the flow to avoid the errors concerning the functioning of the system.

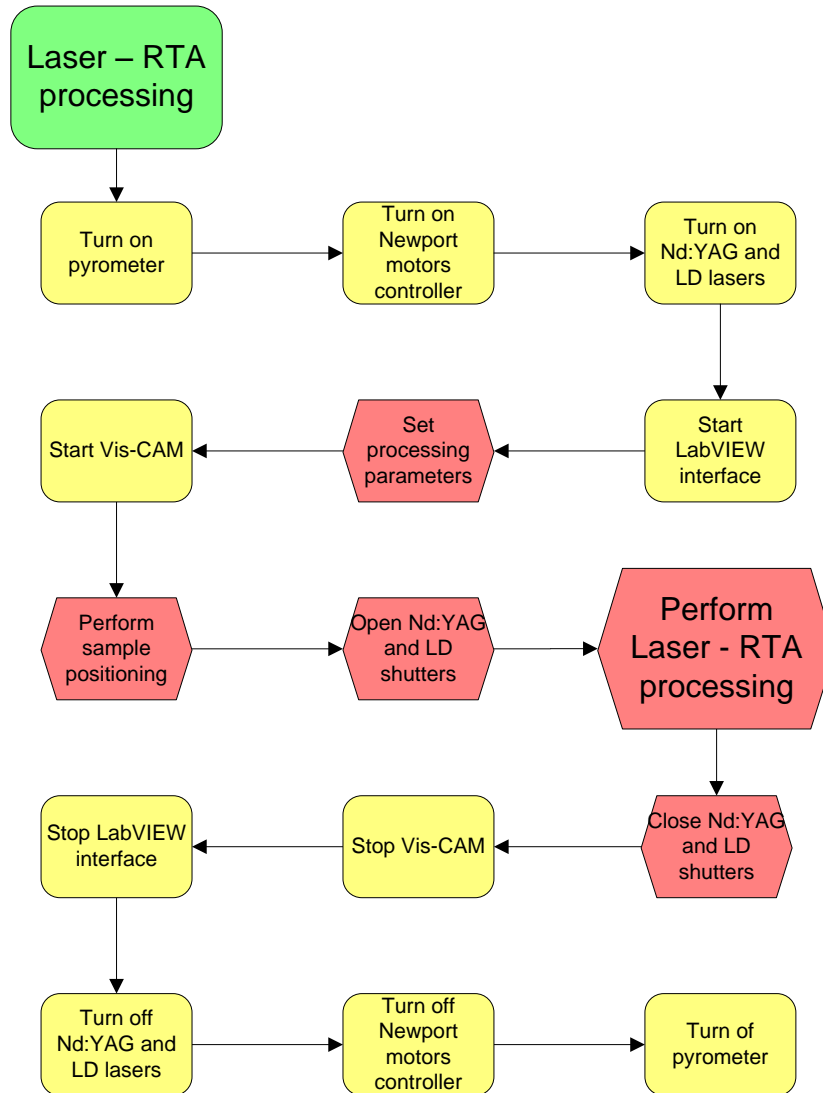
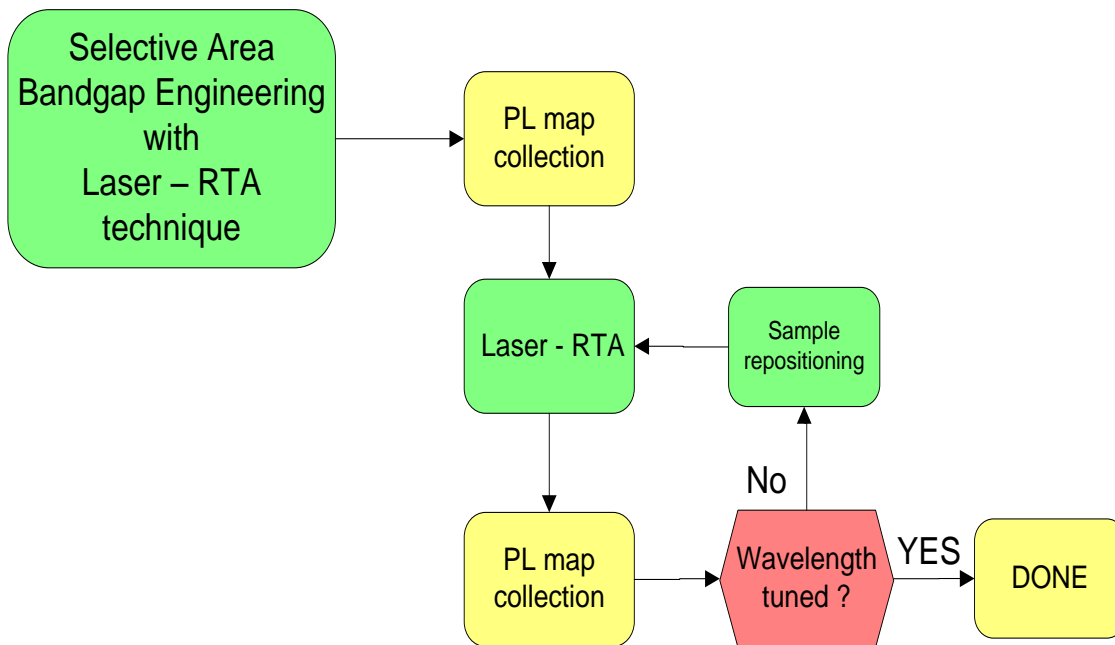


Figure 3.6.1 Block diagram of Laser - RTA process (green – function name; yellow - common steps ; red - specific steps for chosen process).

The Laser – RTA setup allows for selective area QWI in single processing step, or in a series of iterative steps with sample leaving the processing stage for ex-situ diagnostics, e.g., with PL mapping between the steps. A dedicated technique has been developed for the iterative bandgap engineering at selected areas (IBESA) of QWs / QDs semiconductor wafers. The block diagram shown in figure 3.6.2 explains the idea of the IBESA process. After each Laser – RTA processing step, the sample is characterized ex-situ with a PLM-150 mapper. Typically, the amplitude of each bandgap shifting step is chosen between 10 and less than 2 nm. Upon the result meeting the targeted bandgap value the decision is taken about process termination or additional Laser – RTA processing step. It is clear that the success of such an approach strongly depends on the ability to return the sample to its original processing position step after step. The sample repositioning technique and Laser – RTA processing routine take advantage of the LabVIEW based interface I have developed in the frame of this project.



**Figure 3.6.2 Block diagram of the IR Laser – RTA IBESA technique processing steps.**



### **3.7 Conclusions**

The IR Laser IBESA setup is presented. It allows for automated laser rapid thermal annealing of arbitrary size QS wafers, at room ambient for arbitrary emission wavelength tuning at arbitrary areas of monolithically integrated regions. The advantage from the developed IR-CAM is in obtaining the information about both the spatial and temporal temperature profiles. This concerns especially processing with both the LD and Nd:YAG lasers irradiating with constant intensities what results in inducing various processing temperatures at arbitrary areas of the processed wafer. Automated process temperature adjustment relies on the MIKRON M680 pyrometer temperature readout and in a feed-back loop adjusts the LD power to reach desired process temperature. The developed LabVIEW interface allows for monitoring of the stability of the Nd:YAG laser power, control of the Nd:YAG laser beam position by galvo-scanner mirrors, and sample positioning before the Laser – RTA experiment and repositioning to its origin processing site, after returning from off-site characterization experiments, for the purpose of iterative tuning of the emission wavelength of the arbitrary number of spots (each spot X, Y coordinates can be set independently).

# Chapter 4

## Direct Bandgap Engineering at Selected Sites

### 4.1 Introduction

In this chapter I discuss the results of single step Laser – RTA technique application for arbitrary areas bandgap engineering of GaAs and InP based QS wafers. At first I demonstrate results concerning steady laser spot QWI on RA30360 and AX04-182 microstructures followed by determination of the Laser-RTA process resolution. Afterwards, presented are in sequence results of the direct ‘writing’ of uniformly QWI arrays of spots and lines, gradually QWI profiles and arbitrary QWI patterns e.g. letters of QWI material. In this chapter I discuss the consecutive results towards the development of iterative bandgap engineering at selected areas (IBESA) technique that is presented in the previous chapter.

### 4.2 Single spot Laser – RTA QWI

To design the process of direct ‘writing’ of arbitrary patterns of the QWI material I have studied the systematic of steady laser spot irradiation of the RA30360 and AX04-182 microstructures for various processing times and temperatures. Figure 4.2.1 (a) presents the 2-dimensional map of the PL peak position of a single irradiated spot. It has been irradiated simultaneously with LD and Nd:YAG laser beams. The LD delivered 16 W to a 3 mm diameter spot projected on backside of Si wafer while the Nd:YAG 1.2 W to the 500  $\mu\text{m}$  spot projected on top surface of RA36360 microstructure. The sample has been irradiated for 60 s. The resulted intermixed area is of uniform, of circular shape with the greatest blue-shift amplitude at its center. Figure 4.2.1 (b) presents both the resulted PL peak position A-A cross-section plot and 3-dimensional heat diffusion FEM calculated surface temperature profile at its steady state.

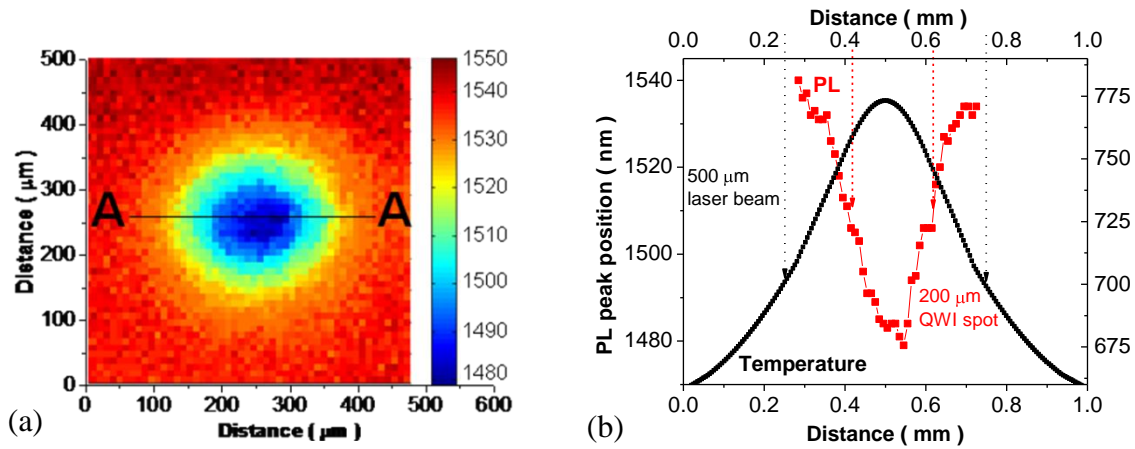


Figure 4.2.1 PL map of a single Laser-RTA irradiated spot (a) and the PL map cross-section profiles of blue-shift amplitude vs. the lasers induced surface temperature (b).

It is visible that the QWI spot diameter is of about 300 μm and corresponds to the RA36360 microstructure's region heated over 700°C. Its transition from as-grown to most-intermixed area follow the Gaussian-like induced temperature profile. It suggests that processing with smaller Nd:YAG laser beam diameters would result in sharper transitions between not intermixed and fully intermixed areas. I have also carried out a systematic study of the QWI amplitude dependance on the Nd:YAG laser power for the constant processing time of 30 s and various Nd:YAG laser beam power. The corresponding results are presented in figure 4.2.2 (a).

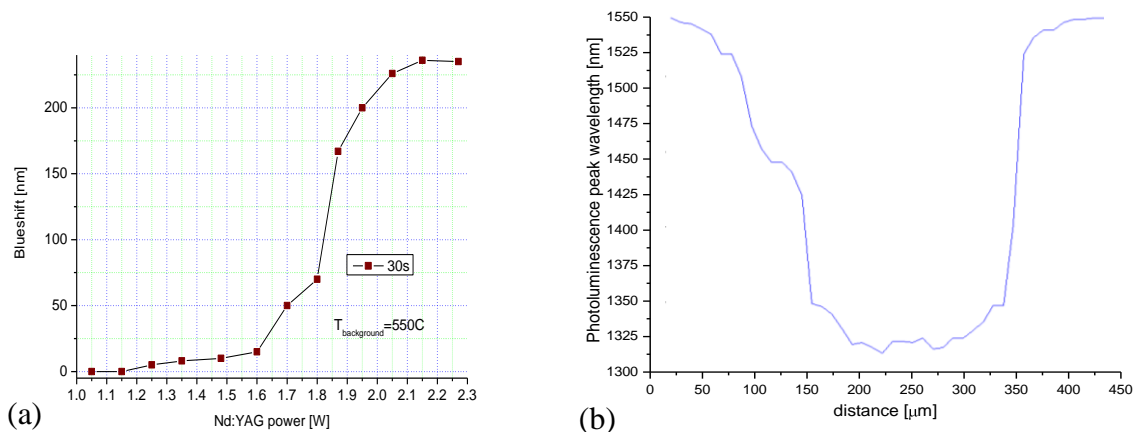
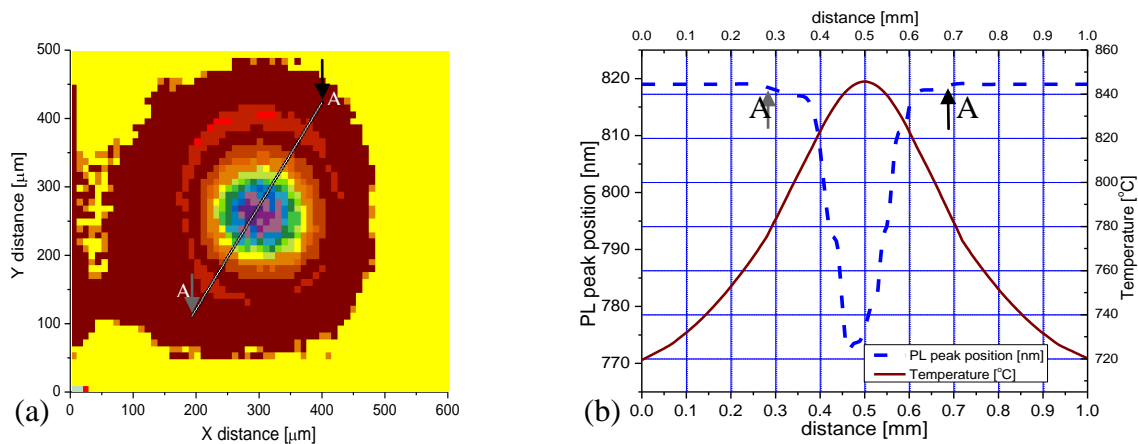


Figure 4.2.2 Blue-shift amplitude vs. the 30 sec irradiation time with variable Nd:YAG laser power (a) and a profile of the QWI site that was blue-shifted by 230 nm (b).

I have obtained an exponential dependence of the induced blue-shift in range up to 170nm versus the applied laser Nd:YAG power in range 1.0 – 2.2 W and with visible saturation region with its plateau around 230 nm. The plot of the PL peak position map cross-section through a 230 nm blue-shifted spot is presented in figure 4.2.2 (b). It is visible that processing with various Nd:YAG applied power would allow to adjust the dwell time in the irradiation process with a moving laser beam and also would affect the spectral accuracy of the Laser – RTA induced bandgap engineering. I have also investigated one-spot irradiation of the GaAs/AlGaAs microstructure using a steady laser beam approach. Figure 4.2.3 (a) presents the PL map of a single spot that has been laser irradiated for 200 sec. The back side of Si wafer was irradiated with the 4 mm spot diameter of 980 nm LD delivering 19 W and the top side with the 500  $\mu$ m Nd:YAG laser beam delivering 1.2 W. This 2-beam irradiation induced the temperature of 800°C, as determined by the pyrometer MIKRON M680. The result demonstrated an uniform circular shape of the intermixed spot with the maximum extend if the QWI amplitude in the center of the spot and gradual transition to its outer part. The A-A cross-section profile of this spot is presented with a dashed line in figure 4.2.3 (b). It presents a symmetric valley-like profile of the QWI spot. The developed 3-dimensional FEM model has been used to calculate the surface temperature profile of the irradiated wafer. The solid line in figure 4.2.3 (b) presents the profile of calculated surface temperature cross-section plot. It is clear that the temperature detected with the Mikron M680 pyrometer has been averaged down to 800 °C only while the middle part of around 280  $\mu$ m in diameter of the irradiated spot has been heated to temperatures higher than 800 °C during the experiment, i.e., above the QWI threshold for this microstructure. Under this temperature the QWI extend is negligible and does not induce change of the as-grown material properties. This demonstrates the ability of selective area processing with the Laser – RTA technique. Figure 4.2.4 demonstrates the dynamics of QWI achieved in such a microstructure for the same background temperature of 720 °C and the processing temperatures of 800, 820 and 840 °C respectively induced with both the LD and Nd:YAG lasers. For instance, it can be seen that the 20-sec irradiation induces bandgap blue-shifts of 7, 14 and 40 nm for processing temperatures of 800, 820 and 840 °C, respectively. Also, the same blueshift can be achieved with various processing times, which is of particular importance for adjustment of the processing speed to achieve desired spectral resolution. For instance a 20nm blueshift can be achieved after 80 sec processing at T = 800 °C or after only 10 sec when processing temperature



**Figure 4.2.3 PL map of a single Laser-RTA irradiated spot (a) and the PL map cross-section profiles of blueshift amplitude vs. the lasers induced surface temperature**

is increased to  $T = 840\text{ }^{\circ}\text{C}$ . Of particular importance for practical applications is that there is no visual surface change or damage even for spot irradiated for 200 sec at  $800^{\circ}\text{C}$ . For all three processing temperatures the relation between Nd:YAG irradiation time and resulting blueshift is linear which indicates that the maximum blueshift has not been reached for this microstructure.

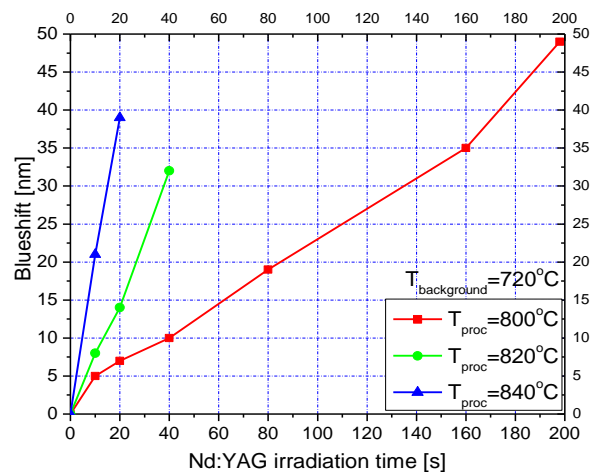


**Figure 4.2.4 Dynamics of bandgap engineering of AX04-182 microstructure induced with Laser-RTA technique.**

### 4.3 Resolution of Laser – RTA QWI technique

The AX04-182 wafer is particularly attractive for the post-growth bandgap engineering due to its QWs system proximity to the wafer's surface. GaAs based microstructures are semi-transparent at room temperatures to both 980 and 1064 nm wavelengths but above 800 °C of the processed wafer's temperature the 1064 nm laser penetration depth is in the order of tens of nanometers and therefore the Laser – RTA processing would concern mostly the surface region of the sample where the QWs are located. I have therefore decided to use the AX04-182 wafer to verify the spatial selectivity of the Laser – RTA process and the possibility of iterative processing that should confirm the direct laser tuning approach of selected areas without affecting the non-processed regions. For that reason I have carried out a two-step Laser – RTA processing experiment. The resulting PL maps measured with the 25  $\mu\text{m}$  measurement grid after the first and second processing steps are presented in figures 4.3.1 (a) and 4.3.2 (a) respectively. At first processing step I have irradiated a set of 4 spots with 40 s, 40 s, 10 s, 10 s processing times. The LD spot has been adjusted to project a spot of 40 mm in diameter while the Nd:YAG spot had diameter of 500  $\mu\text{m}$ . The background temperature was set at 720 °C and processing temperature at 800 °C respectively. The irradiated spots were separated by 800  $\mu\text{m}$  distance between them. It is important to mention that the Nd:YAG laser has been kept continuously turned on to allow its output power to stabilize and I have bring the laser beam to the processing spot area with moving the galvo-scanner mirrors. Otherwise the laser has a warm-up time of about 1.5 s during which the power stabilizes. I have noticed this Nd:YAG laser power behaviour has an impact on the repeatability of the QWI results. Also, before the irradiation of each spot, the sample has been cooled to the background temperature for 10 s. After the collection of the PL map presented in figure 4.3.1 I have manually repositioned the sample back to the Laser – RTA processing stage for the second irradiation step. For that purpose I relied on the markers made on the monitor's screen before the sample left the processing stage for PL map collection. The markers were made at the investigated sample's edges as the reference elements position. Because of the limited accuracy corresponding to the manual sample's repositioning I ran the second processing step in approximately 0.8 mm distance from the previously irradiated spots. I have irradiated the spots with various processing times between 10 s up to 120 s, with 10 seconds interval, maintaining the processing temperature at 820 °C in purpose to exaggerate the

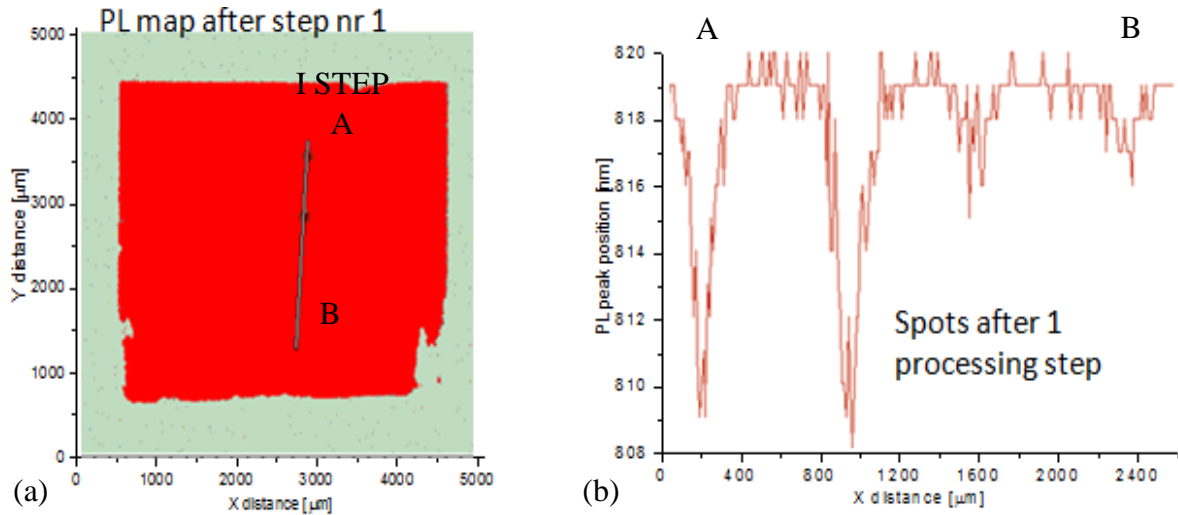


Figure 4.3.1 PLwavelength map of AX04-182 with 4 written spots (a) and their corresponding PL cross-section curve (b).

conditions of the second processing step. The main reason for this experiment was to verify if the second processing step would affect the obtained band-gap blue-shifts in the first processing step. The cross-section plot through the previously processed spots presented on figure 4.3.1 (b) indicates no additional blue-shift induced during the second processing step of other areas however the profile has fewer  $\pm 1$  nm fluctuations. Additionally from the second processing step PL map, it is clearly visible that the heat affected zone increases with increasing irradiation time. For the written spots on a 0.8 mm grid, the processing time should not exceed 80 s otherwise the induced intermixed area would overlap with other processed areas.

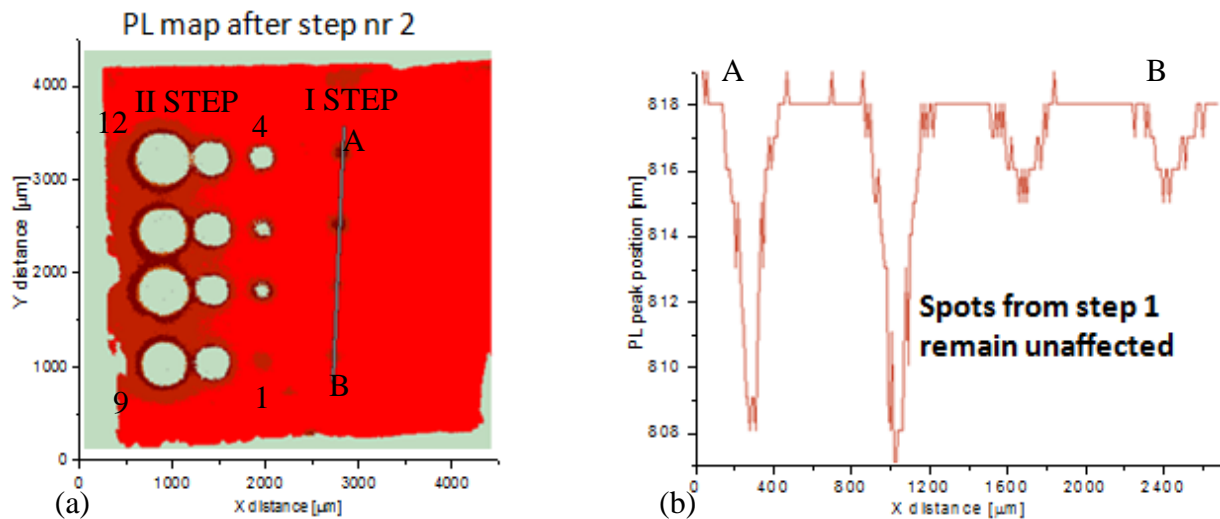


Figure 4.3.2 Selectivity of the Laser – RTA bandgap engineering technique illustrated on PL wavelength map of AX04-182 microstructure.

## 4.4 Uniform QWI profiles

### 4.4.1 Array of QWI spots

To demonstrate the Laser-RTA spatial and spectral processing control of QS microstructures, I have irradiated an array of nine spots in AX04-182 microstructure. The resulting PL map is presented in figure 4.4.1 (a). This experiment has been performed in such a way that I have chosen manually the processing coordinates of each spot. The rest of the processing parameters were computer-controlled with manual control of the processing temperature stability. The spot's background temperature was set at 720 °C by selective irradiation of Si wafer with 980 nm LD delivering 20.73 W to a 3 mm diameter spot. The processing Nd:YAG laser delivered 1.2 W power to a 500 μm diameter spot to the top surface of AX04-182. As a result, the temperature in the center of each spot increased during the processing to above 800 °C (indicated by M680 pyrometer,  $\varepsilon = 1$ ). An array of nine spots of blue-shifted material has been fabricated following 80 sec irradiation at each spot. It is clearly visible that only the selected spots areas were addressed during Laser-RTA processing and it is important to note that apart from the 800 C temperature of the processed spots, the remaining wafer's area was heated up to the background temperature only, below the QWI threshold. Each spot has been irradiated with same processing parameters For the three spots in the second row in figure 4.4.1 (a) an A-A' cross-section line has been extracted and presented in figure 4.4.1 (b). Processed spots were equally spaced on a 450 μm grid. The unprocessed distance between blue-shifted spots was 170 μm indicating some additional possibility of process lateral resolution improvement. It is demonstrated that all three spots were equally blue-shifted by  $16 \pm 1$  nm, which is also the case for all nine processed spots. The diameter of all blue-shifted regions is similar and around  $280 \pm 20$  μm. Afterwards, to demonstrate the spectral selectivity and potential for iterative Laser - RTA technique processing I have performed two consecutive QWI steps experiment. During the first processing step I have 'written' an array of nine equally blue-shifted by 6 nm spots. Then I have collected the PL map presented in figure 4.4.2 (a) and manually repositioned the sample to the processing origin position for the second processing step. In this experiment the processed spots coordinates were also manually controlled. In the second processing step spots 2, 4, 6, and 8 were additionally processed and blue-shifted by 2 nm.



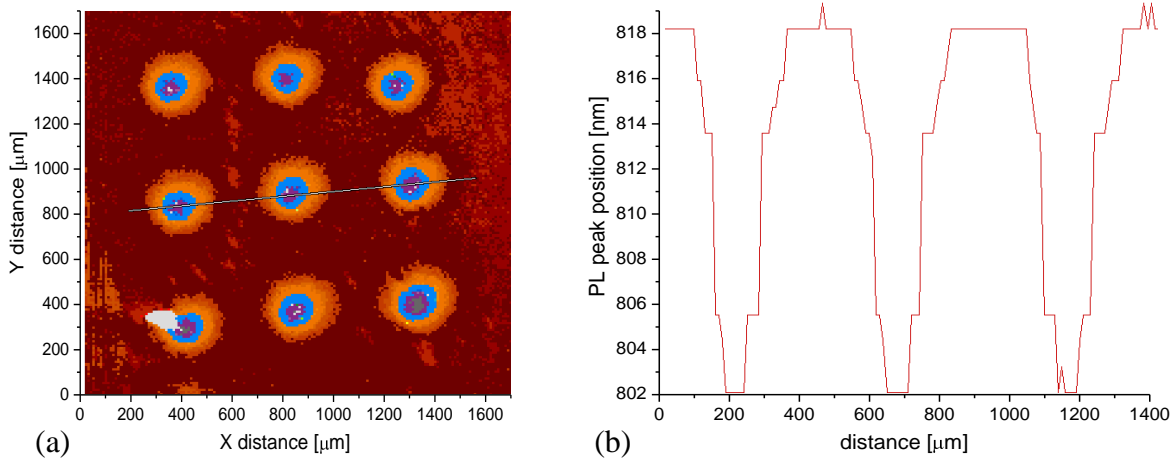


**Figure 4.4.1** PL map of AX04-182 that was irradiated at nominally the same conditions in nine spots (a), and the PL peak position plot along A-A direction (b).

The resulting PL map after the second processing step is presented in figure 4.4.2 (b). In both processing steps the background temperature was set to 720 °C and the LD projected spot was of 3 mm in diameter delivering 20.73 W of power to the back side of Si wafer. The processing temperature was 800 °C induced with 1064nm Nd:YAG laser delivering 1.2 W to 500  $\mu\text{m}$  diameter spot. Each spot was processed for 40 sec during each processing step. It is clearly visible that the non-processed areas remained unchanged. This experiment demonstrated the potential for development of automated iterative bandgap engineering at selected areas (IBESA) technique for direct writing/tuning of PICs.

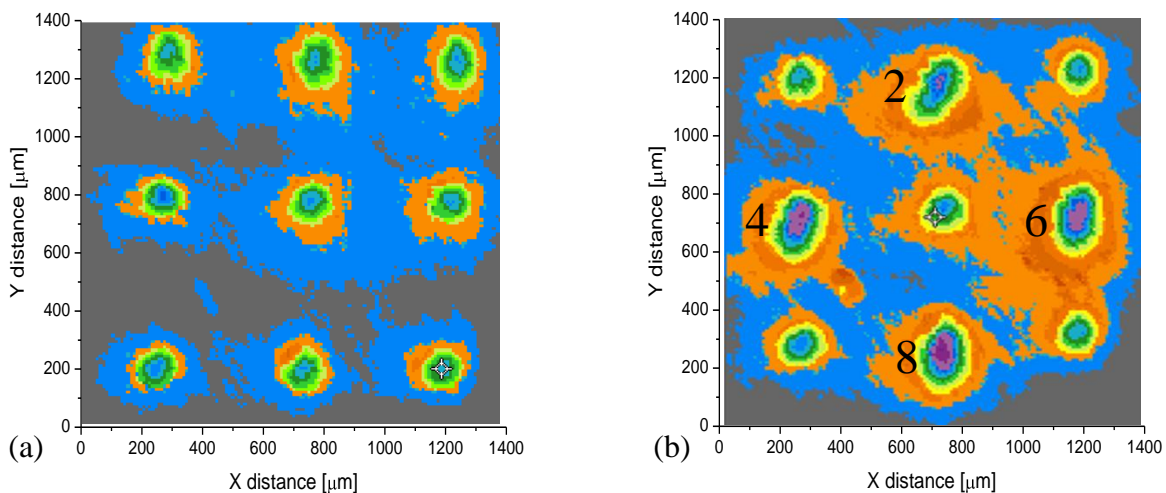
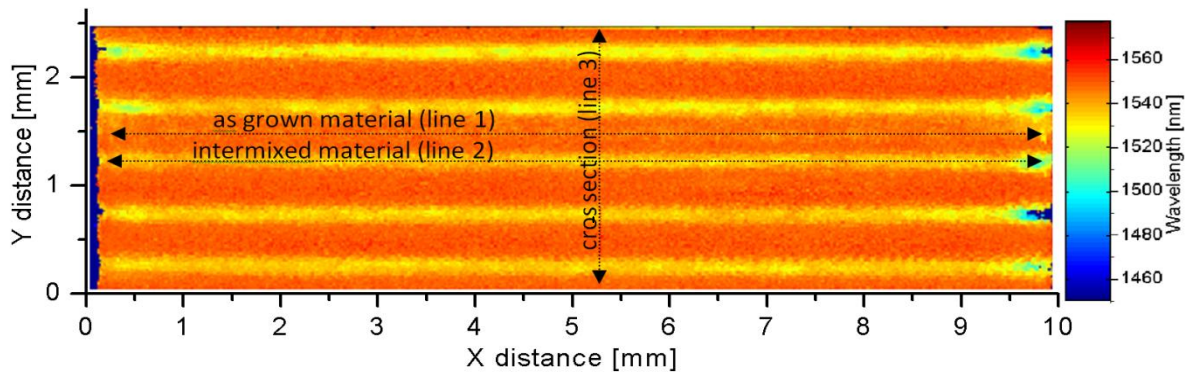


**Figure 4.4.2** PL maps of AX04-182 irradiated under nominally identical conditions in nine spots (a) and after spots 2, 4, 6 and 8 additionally irradiated for 40 sec (b).

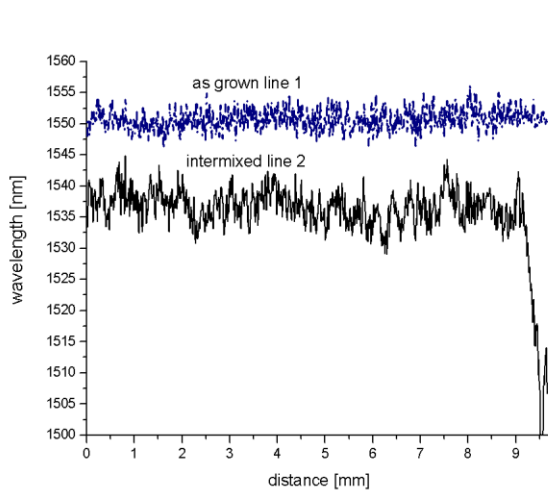
#### 4.4.2 Array of QWI lines

The results discussed in this section have been published in [Stanowski and Dubowski 2009].

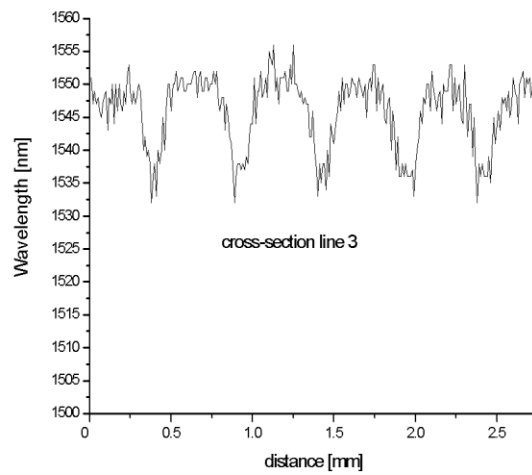
In the fabrication of the photonic integrated circuits the challenge is to develop manufacturing technologies capable of cost-attractive delivery of photon emitters and PICs comprising lasers, modulators, waveguides and other active photonic devices integrated within a single QS wafer. I made an approach to write the uniform and arbitrary lines of QWI material within a single processing step. This is of particular importance to demonstrate both spectral and spatial control when processing with moving Nd:YAG laser beam. For the design of the process I have calculated the heat transfer in the processed microstructure using the custom developed 3-dimensional FEM with simulation of the moving Nd:YAG laser beam and studied the laser induced temperature profiles. The corresponding results are presented in figure 4.4.3. A one-direction scan indicates that one of the sample edges will be underheated, while the other overheated. Scanning in two directions will result in a more uniform average temperature in the center of the sample. Therefore, I have chosen the two-direction scan mode to ‘write’ an array of uniformly QWI lines in the RA30360 material. Figure 4.4.3 presents the results of Laser – RTA performed for RA30360 sample. The sample’s background temperature was maintained at 620 °C with the LD delivering 40 W to a 25 mm diameter spot. Five lines of the QWI material have been written sequentially with the Nd:YAG laser delivering 1.2 W power to a 0.5 mm diameter spot. The scanning speed of the spot was 1 mm/s. A PL map of the 2.5 mm x 10 mm fragment of the processed sample is shown in figure 4.4.3 (a). Five lines of the QWI material, blue-shifted by approximately 15 nm, can easily be distinguished from the background of the as-grown material emitting at 1550 nm. Each line was fabricated following 20 double passes, which approximately corresponds to the dwell time of 20 s. The same magnitude of the blue-shift for this material, if background heated to 550 °C, required approximately a 30 s dwell time. The significantly shorter dwell time in the current experiment indicates greater temperature achieved in the center of the Nd:YAG laser spot. The lines of the QWI material written in this experiment are approximately 300 μm wide, which indicates that only the top portion of the Nd:YAG Gaussian beam induced a temperature exceeding the threshold value for QWI. A comparison between PL peak positions along as-grown material (line 1) and the Laser – RTA produced line (line 2) is shown in figure 4.4.3 (b). The PL peak position in the middle of the QWI line is  $1538 \pm 5$  nm, which compares to



a)



b)



c)

**Figure 4.4.3** PL map of a Laser - RTA processed InGaAsP/InP QW sample with 5 lines of the intermixed material (a), PL peak position along the as-grown material, line 1, and the Laser - RTA produced line 2 of the intermixed material (b), and PL peak position across the sample (c).

1532  $\pm$  4 nm for the scan across the as-grown material. As predicted by the FEM calculations (figure 2.3.3), both edges of the sample have been overheated and show the increased blue-shift amplitude of the QWI material. I expect that the effect of overheating the sample edges could be avoided by using a variable speed Nd:YAG laser beam. A cross-section PL scan across the processed sample is shown in figure 4.4.3 (c). The maximum blue-shifted amplitudes that have been observed for each line of the QWI material are at 1535  $\pm$  1 nm. This illustrates that the Laser – RTA technique achieves excellent reproducibility of the annealing conditions.

## 4.5 Arbitrary QWI profiles

### 4.5.1 Gradually QWI lines for fabrication of superluminescent diodes (SLDs)

Quantum well wafers with the monolithically integrated regions of graded bandgap material are of high interest for the realization of the enhanced spectrum superluminescent diodes. I have applied the developed Laser – RTA technique to fabricate the gradually QWI material along the laser beam irradiation path. Figures 4.5.1 and 4.5.2 illustrate results obtained on AX04-182 material while figure 4.5.3 shows results of gradual intermixing of the InGaAs/InGaAsP/InP which comprises a full laser structure. In both cases I have been using my developed LabVIEW interface to precisely control the process temperature and the irradiation dwell time during the experiment by automated change of the laser beam position. To guarantee the repeatability of bandgap amplitude modification the challenge was to maintain the same processing temperature while changing the velocity of the laser beam, therefore the power of the LD 980 nm laser source has been controlled in a feedback loop by the M680 pyrometer at 10 Hz rate. The three parallel lines of the QWI material (figure 4.5.1 (a)) have two slopes of graded bandgap change visible on line # 1 cross-section in figure 4.5.1 (b). First slope of 10 nm amplitude has been created on first 200  $\mu\text{m}$  distance which corresponds to the gradient obtained for one-spot irradiation. In this experiment it has been demonstrated that the same amplitude of bandgap change can be projected on arbitrary distance, e.g. 2500  $\mu\text{m}$ . Considering the PL mapper  $\pm 0.5$  nm spectral accuracy error there is visible in figure 4.5.1 (b) that both fabricated gradient slopes are not linear, however this behaviour is clearly pronounced on both gradient slopes and can be related to the not linear QWI material response. It is visible that the material has slower response at the beginning region (814 – 816 nm) then there is a rapid phase region (814 – 809 nm) and slower region (809 – 806 nm). During this test the background temperature was 700 while the processing temperature was maintained at 820  $^{\circ}\text{C}$ . The diameters of the LD and Nd:YAG laser beams were 2 mm and 500  $\mu\text{m}$  respectively. To prove the spatial and spectral control I have conducted an additional study of the reproducibility of the Laser – RTA direct writing of the graded bandgap material. The goal was to verify the symmetry of slopes of gradually written QWI lines. The resulting PL map of three lines written with arbitrary profiles is presented in figure 4.5.2 (a).

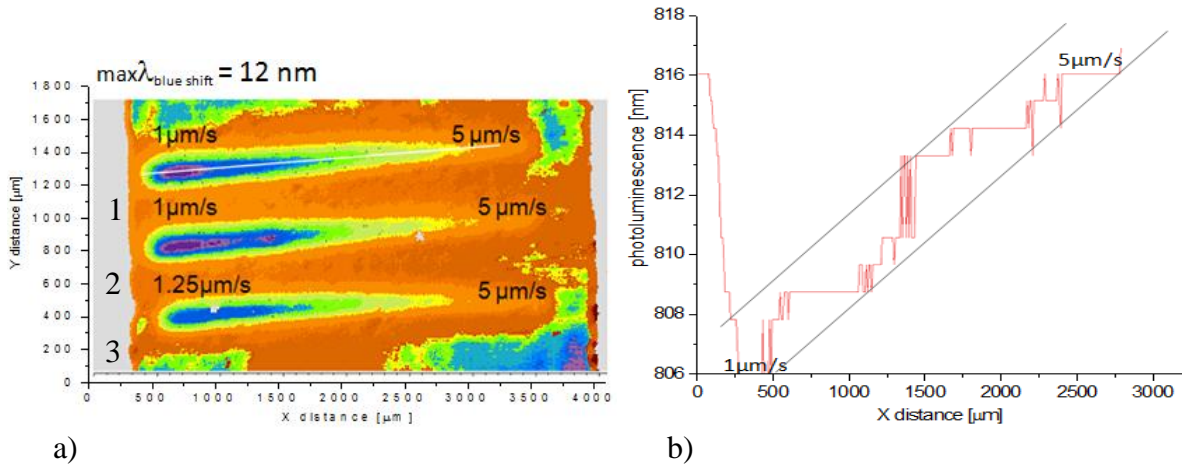


**Figure 4.5.1** PL map of a Laser - RTA processed AX04-182 QW wafer with 3 lines of gradually QWI material (a) and PL peak position along the line #1 (b).

Line nr 1 in figure 4.5.2 (a) had been written with a continuous velocity decrease from 4  $\mu\text{m/s}$  down to 1  $\mu\text{m/s}$  over 3000  $\mu\text{m}$  distance. Lines nr 2 and 3 have been written with an arbitrary sequence of velocity control. Figure 4.5.2 (b) presents the line 3 PL spectrum peak position wavelength cross-section plot together with marked the laser beam velocity values along the written line. It is clearly visible that accordingly to the increase / decrease of the laser beam processing dwell time there is direct proportional increase / decrease in the amplitude of the induced bandgap blue-shift. It is important to notice that processing with the velocity of 5  $\mu\text{m/s}$  does not alter the bandgap however there is a 5 nm bandgap variation between the regions processed with velocity 2  $\mu\text{m/s}$  and 1  $\mu\text{m/s}$ , which corresponds to 814 nm and 809 nm emission wavelengths.

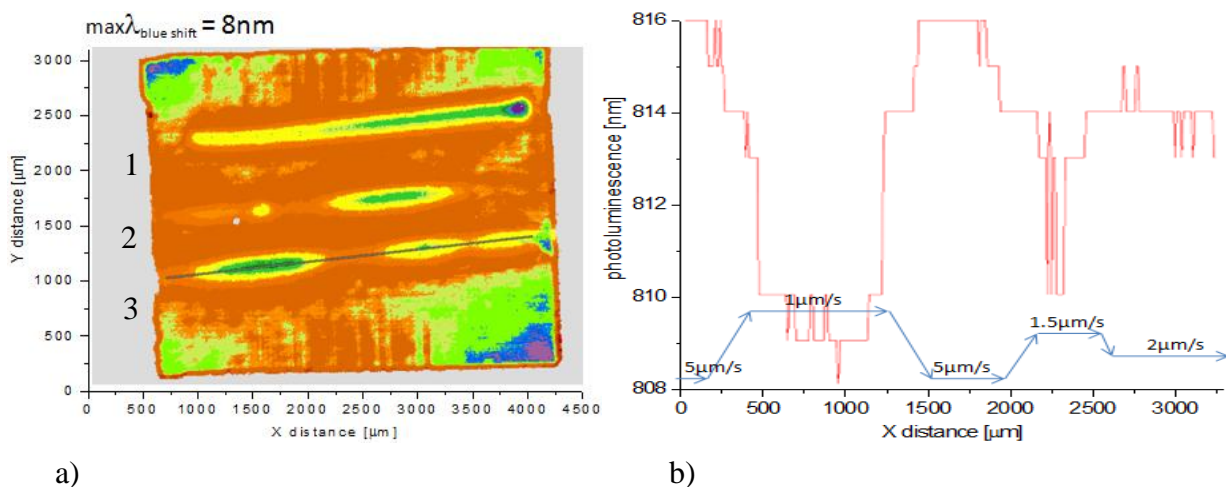


**Figure 4.5.2** PL map of a Laser - RTA processed AX04-182 QW wafer with 3 arbitrary gradient lines of QWI material (a) and PL peak position along the line #3 (b).

Laser – RTA induced blueshift amplitude results depend on the time and the temperature of the process, therefore offers convenient ways of the process control. Faster lines writing with arbitrary periods of gradient bandgap change would require increase of the process temperature. I have developed the Laser – RTA III-V QS bandgap engineering technique for direct writing of arbitrary patterns of photonics integrated circuits. Figure 4.5.3 (a) demonstrates the PL map of an example of the Laser – RTA processed and gradually QWI the InGaAs/InGaAsP laser structure prepared for fabrication of the enhanced spectrum super-luminescent diodes (SLDs). The five QWs InGaAs/InGaAsP processed wafer used for this experiment consists in : 1.4  $\mu\text{m}$  thick Si-doped n-InP lower cladding ( $2 \times 10^{18} \text{ cm}^{-3}$ ), a 80 nm thick Si-doped n-InGaAsP 1.05Q (quaternary alloy with bandgap energy centered on 1.05  $\mu\text{m}$ ) lower waveguiding core ( $10^{17} \text{ cm}^{-3}$ ), 50 nm thick Si-doped n-InGaAsP 1.2Q ( $5 \times 10^{17} \text{ cm}^{-3}$ ), five 5 nm thick InGaAs – 12 nm thick InGaAsP 1.25Q undoped QWs active layers, a 50 nm thick Si – doped n – InGaAsP 1.2Q ( $5 \times 10^{17} \text{ cm}^{-3}$ ) layer, a 80 nm thick Si-doped n-InGaAsP 1.05Q upper waveguiding core ( $5 \times 10^{17} \text{ cm}^{-3}$ ), a 200 nm thick Zn-doped p-InP layer ( $6 \times 10^{17} \text{ cm}^{-3}$ ), a 10 nm thick Zn-doped 1.3Q p-InGaAsP etch stop ( $6 \times 10^{17} \text{ cm}^{-3}$ ), a 1.2  $\mu\text{m}$  thick Zn-doped p-InP upper cladding ( $6 \times 10^{17} \text{ cm}^{-3}$ ), a 200 nm thick Zn-doped p-InGaAsP 1.2Q ( $2 \times 10^{18} \text{ cm}^{-3}$ ) layer, a 100 nm thick Zn-doped p-InGaAs etch stop ( $8 \times 10^{18} \text{ cm}^{-3}$ ), and a 200 nm thick surface undoped InP layer. The as-grown wafer had homogenous PL peak position distribution centered at 1535 nm. I have processed the material with a simplified version of the Laser – RTA setup employing the 980 nm LD as a single irradiation source without the use of the Nd:YAG laser. The fiber pigtailed (1 mm core, NA = 0.22) GaAs/AlGaAs laser diode delivered 20 W of power to the 2 mm in diameter spot projected on the back side of a 2” silicon wafer constituting substrate for the processed InGaAs/InGaAsP laser structure. During the experiment the LD position remained stable while the processed sample’s holder was moving with velocity decreased from 17  $\mu\text{m/s}$  (left side) to 5  $\mu\text{m/s}$  (right side) along the sample’s transversal direction. The reason of the laser beam velocity variation was the ‘rapid prototyping method’ of adjustment of the proper dwell time parameters to achieve the required QWI amplitude and match the  $7^\circ$  tilt to the crystallographic plans along which the fabricated devices were cleaved to avoid lasing action.

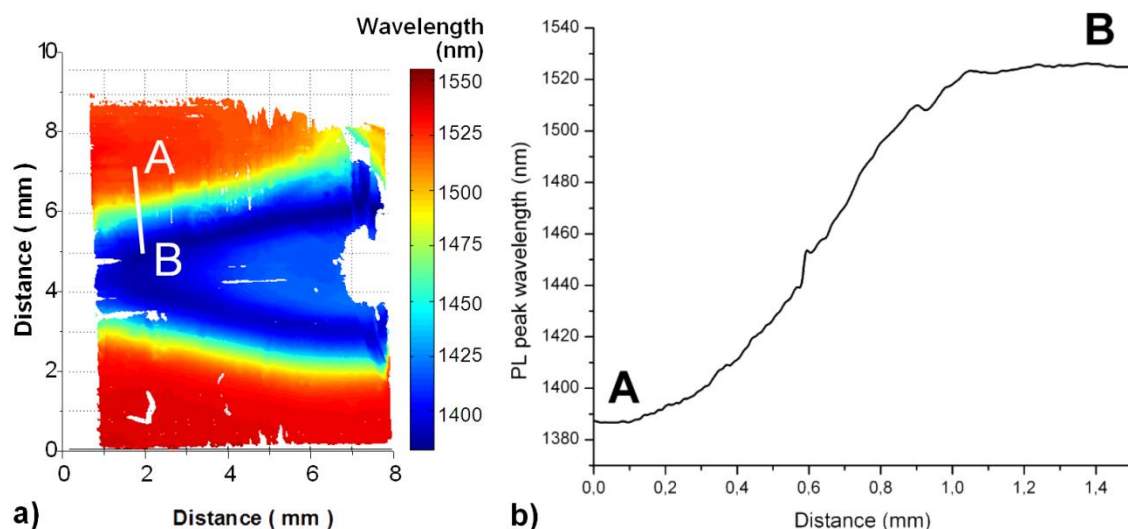


**Figure 4.5.3** PL wavelength map of a sample exposed to a CW laser beam moving at variable speed (a) and the bandgap energy profile along the AB line (b)

The PL peak wavelength has been blue-shifted to its extremity down to 1387.5nm and then it started to move back towards red for the longer processing times. The Processed InGaAs/InGaAsP wafer’s surface temperature had been continuously controlled and maintained during the processing at 730 °C. For that reason the output power of the LD has been controlled in a negative feedback loop by M680 pyrometer. From the resulted PL map it is clearly visible that at constant temperature of 730 °C the heat affected zone strongly depends on the dwell time of the process. That explains the fact that processing with greater velocities results in fabrication of narrower lines but also smaller amplitudes of blue-shift bandgap modification and vice-versa. The A-B PL peak position cross-section plot is presented in figure 4.5.3 (b). It shows the PL cross-section profile along the fabricated SLD device. The Laser – RTA processed InGaAs/InGaAsP QWI laser structure has served for further fabrication of the SLD device and had been tested and described elsewhere [Beal, 2010 – unpublished result].

## 4.6 Arbitrary QWI patterns

Another application of the Laser – RTA technique employs a fast scanning Nd:YAG laser beam writing in a one processing step an arbitrary pattern of lines. As an illustration of this potential I have written an Université de Sherbrooke logo ‘watermark’ of the QWI material.

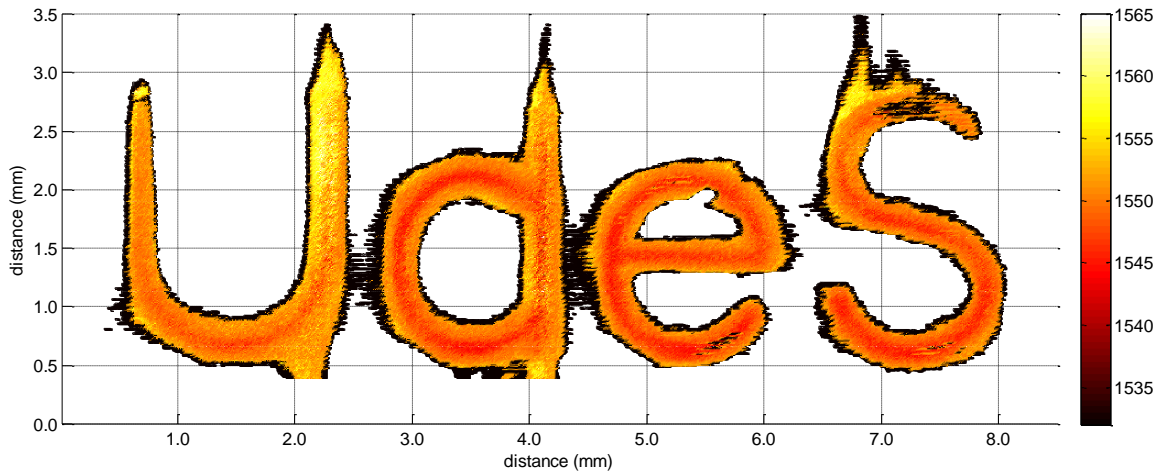


**Figure 4.6.1 PL wavelength map of the Laser - RTA processed RA30360 sample with a 'watermark' of the QWI material.**

Figure 4.6.1 shows the resulting PL wavelength map of the RA30360 processed wafer that was irradiated with the galvo-scanner controlled position of the Nd:YAG laser beam writing the letters 'UdeS'. This 'watermark' was obtained following 400 passes of the 1.2 W Nd:YAG spot moving at 50 mm/s (4 s dwell time). In this case I have used the Laser – RTA setup employing both 980 nm LD and 1064 nm Nd:YAG lasers. The background temperature of the experiment was maintained at 620 °C. It can be seen that the material has been intermixed uniformly along the entire 'UdeS' watermark with the contrast (blue-shift of the bandgap) of approximately 10 nm. It is interesting to note that the width of this Laser – RTA written line is 100  $\mu\text{m}$ , which is 5 times smaller than the diameter of the writing beam. This clearly demonstrates that similarly to the results discussed in figures 4.2.1 and 4.2.3, that only the top portion of the Nd:YAG beam induced a temperature exceeding the threshold for effective QWI.



## **Chapter 5**

# **Iterative Bandgap Engineering at Selected Areas – IBESA for QW and QD wafers**

### **5.1 Introduction**

The IBESA technique takes advantage from the computer controlled wafer's positioning at the processing site technique and automated IR Laser – RTA technique. This became an instrument for the tuning of emission wavelength at selected regions of QS wafers with controlled  $\pm 1\text{nm}$  spectral accuracy.

## 5.2 IR Laser-RTA IBESA of QWs semiconductor wafer

The results discussed in this section have been published in:

R. Stanowski, Optics Express 17(22), 19842 (2009).

### 5.2.1 Experimental details

The spatially selective laser annealing of QS wafers was carried out with the laser rapid thermal annealing (Laser-RTA) setup using the LD for background heating, and Nd:YAG laser for ‘writing’ of regions of the QWI material. The system was equipped with a galvanometric scanner (GS) allowing to raster the Nd:YAG laser beam over the sample with a controlled velocity. An F-Theta lens mounted at the output of the GS head assures that a beam with the same profile is delivered to any site of the wafer’s surface. Temperature of the processed spot was monitored with Mikron M680 and a custom designed infrared camera (IR-CAM). Another 640 x 480 pixel visible camera (Vis-CAM) operating at 10 Hz was used to monitor the sample’s positioning. With a 0.5 mm diameter of the Nd:YAG laser spot and depending on the amplitude of the blueshift, the fabrication of QWI material could be carried out with the spatial resolution of 100 to 400  $\mu\text{m}$ . Higher spatial resolution processing is feasible as the Nd:YAG laser beam delivery system allows working with laser spots down to 12  $\mu\text{m}$  in diameter. The as-grown RA30360 wafer was coated with 50 and 500 nm thick  $\text{SiO}_2$  layers, using plasma-enhanced-chemical-vapor-deposition, on the front (polished) and back (unpolished) sides of the wafer, respectively. The background and intermixing temperatures were set at 550 and 760  $^\circ\text{C}$ . Room temperature PL measurements were carried out with a commercial mapper (Philips PLM-150) using an Nd:YAG laser ( $\lambda = 532 \text{ nm}$ ) as an excitation source and an InGaAs array detector. The PL mapping was performed with 1 nm spectral and 10  $\mu\text{m}$  and spatial resolutions. Based on an edge-detection algorithm, the custom LabVIEW image recognition software was developed for precise repositioning of the samples returning from PL mapping measurements. The software interfaced VIS-CAM and the XYZ-R motorized stage allowing sample reinstallation within 5 $\mu\text{m}$  translational and 0.05 deg rotational accuracies. A schematic idea of the IBESA process is illustrated in figure 5.2.1.

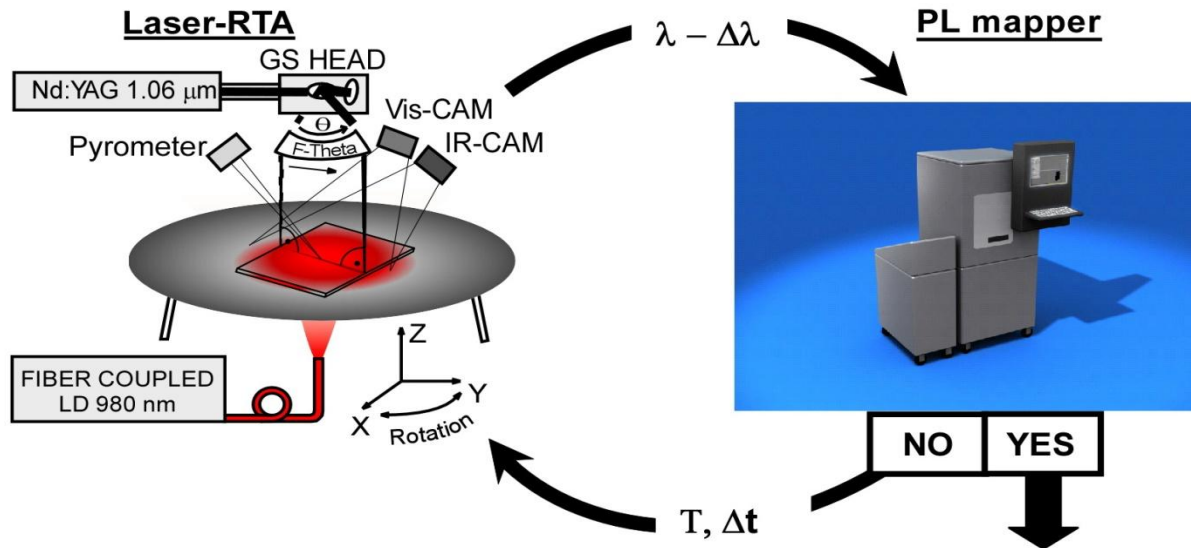


**Figure.5.2.1. Schematic idea of the IBESA process.**

The preliminary results have shown that the investigated InGaAs/InGaAsP microstructure could be blueshifted by 230 nm in a single irradiation step after 30 s irradiation at 780°C [Stanowski, Boaziz 2008]. These experiments enabled me to determine the conditions of irradiation leading to less than 2 nm blueshift in one step.

## 5.2.2 Results and discussion

Figure 5.2.2(a) shows a PL wavelength peak map of a fragment of the sample irradiated with the Nd:YAG laser beam in 20 sites for different periods of time. The conditions of the irradiation at A1-A4 and B1-B4 sites and the achieved blueshifts are given, respectively, in the ‘Step 1 processing time’ and ‘Peak wavelength’ columns of Table 5.2.1. It can be seen that the 30 sec irradiated spots A3 and B1 have been blueshifted by 70 nm from the initial 1550 nm. Their diameter is approximately 280 μm. Figure 5.2.2(b) compares the PL spectrum of the center of the A3 spot with that of the as-grown material, both obtained under nominally the same excitation conditions. The decreased PL intensity of the A3 site is related to the reduced quantum confinement of the intermixed QWs. It is worth mentioning that for blueshifts  $\leq 50$  nm the opposite effect was observed, with a slightly increased PL intensity of the intermixed material. A reduced concentration of grown-in defects following the annealing step, before the reduced confinement starts to dominate the QW PL emission intensity, could explain such a behavior.

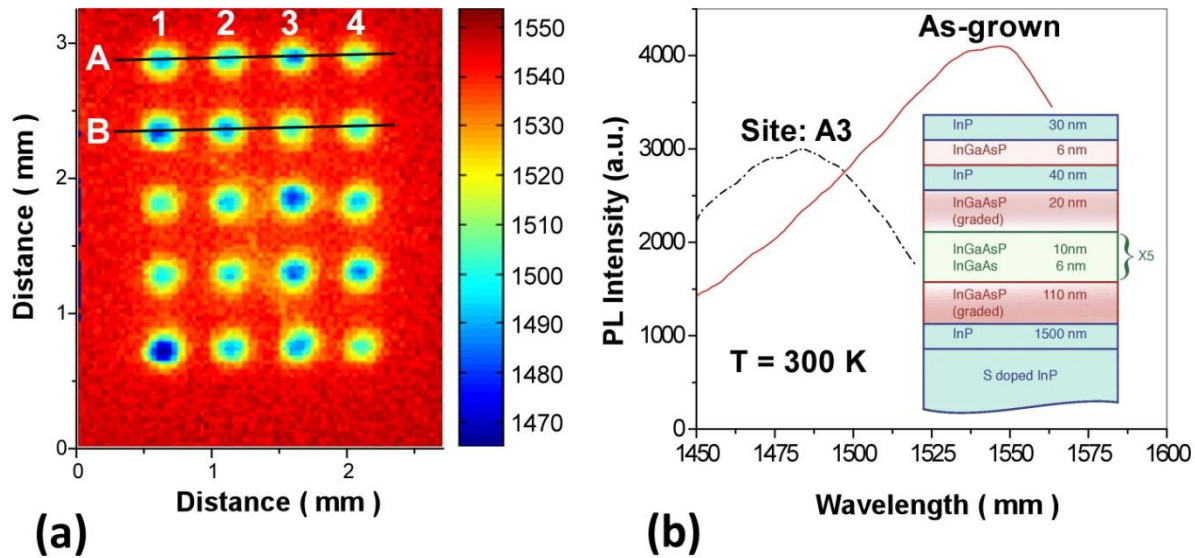


**Figure 5.2.2** PL peak wavelength map of an InGaAs/InGaAsP QW wafer with 20 sites of QWI material fabricated by Laser-RTA (a), and PL spectra of the as-grown and 70 nm blueshifted (site A3) materials (b). The inset shows details of the processed microstructure.

A similar effect has also been observed in other laser and non-laser annealed InP/InGaAsP QW heterostructures [Dubowski, 2004; Lu, 2008]. Sites A1, A2 and A4 show the QW material emitting at 1488, 1492 and 1504 nm, while site B2 emits at 1484 and sites B3 and B4 at 1497 nm. To illustrate the IBESA approach, we requested that all the sites from both rows A and B would emit at 1480 nm, i.e., at the same emission wavelength as A3 and B1. This required additional blueshift amplitudes from 9 to 23 nm. Cross-scans indicating PL peak positions for the A series sites, following processing No 1, 2 and 3, are shown in figure 5.2.3. The targeted 1480 nm emission wavelength was achieved following additional two-step processing at A2 and A4, and one-step at A1. Similarly, as illustrated in figure 5.2.4, the targeted 1480 nm emission from the B series sites has been achieved following additional one- or two-step-processing. Thus, these results demonstrate a highly reproducible process capable of controlling emission wavelength of InGaAs/InGaAsP QW microstructures, between 1550 and 1480 nm. Note that the wavelength tuning precision of  $\pm 1$  nm observed in the current experiment is limited by the relatively low resolution of room-temperature PL spectra. Although for some applications this precision is sufficient, the ultimate tuning precision of the IBESA process will require low-temperature PL data.

**Tableau 5.2.1 Irradiation time and resulting PL peak wavelength emission from InGaAs/InGaAsP QW heterostructures processed by a 3-step IBESA technique.**

Poi nt #	Step 1 processin g time (s)	Peak wavelen gth $\lambda$ (nm)	Step 2 processin g time (s)	Peak wavelen gth $\lambda$ (nm)	Step 3 processin g time (s)	Peak wavelengt h $\lambda$ (nm)
A1	27	1488	-	-	4.5	1479
A2	25	1492	3	1485	2	1480
A3	30	1480	-	-	-	1480
A4	20	1504	9	1486	2	1481
B1	30	1480	-	-	-	1480
B2	28	1484	-	-	1.8	1481
B3	23	1497	4	1486	2.1	1481
B4	23	1497	4	1486	2.1	1481

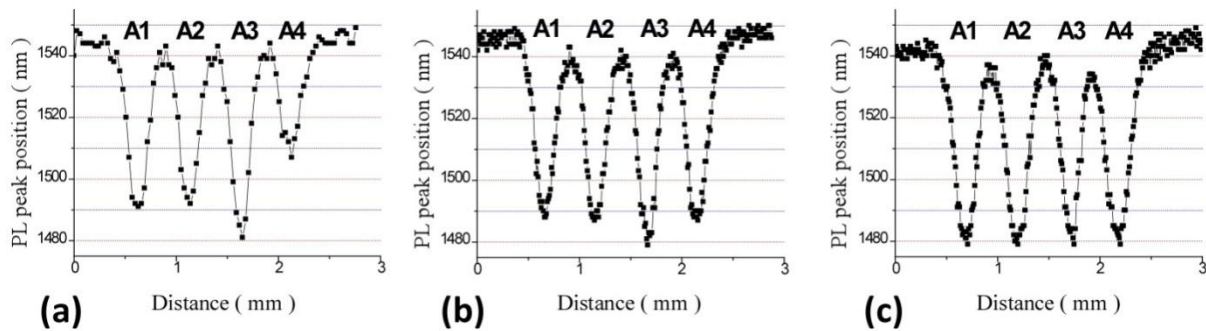


**Figure 5.2.3 PL peak wavelength cross-scans for A1, A2, A3 and A4 sites following the 1st (a), 2nd (b) and 3rd (c) IBESA annealing step.**

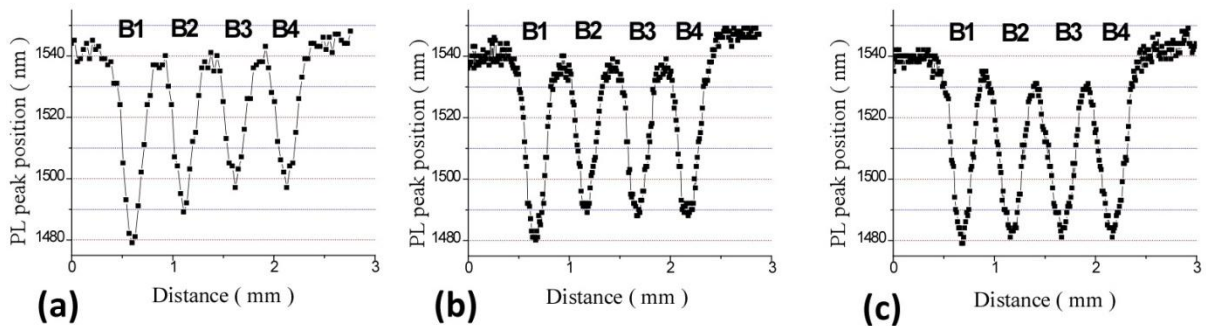


**Figure 5.2.4 PL peak wavelength cross-scans for B1, B2, B3 and B4 sites following the 1st (a), 2nd (b) and 3rd (c) IBESA annealing step.**

## 5.3 IR Laser-RTA IBESA of QDs semiconductor wafer

The concept of tuning of the emission wavelength of a single QD is demonstrated using the IR Laser – RTA IBESA technique for tuning of the average emission wavelength of a population of self-assembled InAs QDs. Single-colour arrays of 200  $\mu\text{m}$  diameter samples of QDs, emitting at wavelengths shifted by 15 nm and 25 nm have been fabricated. The achieved average spectral precision of QDs spots emission wavelength at room-temperature is better than  $\pm 0.5$  nm.

### 5.3.1 Experimental details

I have carried out the QDI experiments using the same Laser-RTA setup configuration as used for QWs wafers adjusting the background and processing temperatures to 500 °C and 700 °C respectively. The as-grown InAs QDs wafer was coated with plasma-enhanced-chemical-vapor-deposition 50 and 500 nm thick  $\text{SiO}_2$  layers on the front (polished) and back (unpolished) sides of the wafer, respectively. Room temperature PL measurements were carried out in-between the irradiation steps with a commercial PL mapper (Philips PLM-150) using an Nd:YAG laser ( $\lambda = 1064$  nm) as an excitation source and an InGaAs array detector. The PL mapping was performed with 1 nm and 10  $\mu\text{m}$  spectral and spatial resolutions, respectively. Based on an edge-detection algorithm, the custom LabVIEW image recognition software was used for precise repositioning of samples returning from PL mapping measurements.

### 5.3.2 Results and discussion

Figure 5.3.1 presents PL maps of selectively processed areas with the IR (CW) Laser – RTA IBESA technique. Maps (a), (b) and (c), (d) present the A1, A2, A3 and B1, B2, B3 processed spots after the first and last annealing steps respectively. For each PL map attached is the cross-section scan to demonstrate the resulting PL peak emission wavelength profile. Additional processing times were chosen arbitrarily and estimated separately for each processed spot after each annealing step. Spots A1, A2, A3 after first 30 s annealing step were not uniformly blueshifted with  $\Delta\lambda = 5$  nm. After the final processing the emission wavelength of all spots in

row ‘A’ was tuned to 1475 nm and  $\Delta\lambda$  between the spots decreased to 0.5 nm. Secondly, three spots constituting row ‘B’ were annealed. Figure 5.3.1(c) demonstrates that although the point B1 has been shifted by 15 nm during first annealing step points B2 and B3 were just slightly blueshifted so the difference between the spots was  $\Delta\lambda = 10$  nm. Additional processing was applied to spots B2 and B3 and it is demonstrated in figure 5.3.1(d) that all spots in row ‘B’ emit at very same 1485 nm wavelength with  $\Delta\lambda = 0.5$  nm. All processing times and resulting blueshifts per laser annealing step per spot are gathered in table 5.3.1. It is important to mention that the processed spots were written within only 1.5 mm distance from the sample’s edge, which varies the temperature profile of each heat affected zone and therefore the processing times were estimated individually for each processed spot. The width of the 15 nm blueshifted spots is 51  $\mu\text{m}$ . Width of spots blueshifted by 25 nm is 66  $\mu\text{m}$ . This width increases with the increase of the blueshift amplitude and does not depend on the number of laser annealing steps, demonstrating the adequate resolution of the sample repositioning system. Also it is important to notice that processing of spots B1, B2, B3 does not affect the PL peak position wavelength of spots A1, A2, A3, which shows that Laser – RTA process is spatially selective and might be applied for emission wavelength correction. The ultimate resolution of the Laser – RTA technique has not been studied. There are visibly altered areas in-between the processed spots. The effective blueshift of these areas depend on the blueshift amplitude of the neighbouring processed spots, the distance between the spots, the Nd:YAG laser beam diameter and the effective processing temperature profile. In this experiment the amplitude of blueshift in-between the processed spots is of about 50 % of the desired blueshift amplitude at the center of the processed spot.

**Tableau 5.3.1 Processing times vs resulting PL peak wavelength emission from InAs/InP QDs processed sites by 4-step Laser – RTA IBESA technique**

	Step 1	PL peak	Step 2	PL peak	Step 3	PL peak	Step 4	PL peak	Total	PL peak
	t [s]	$\lambda$ [nm]	t [s]	$\lambda$ [nm]	t [s]	$\lambda$ [nm]	t [s]	$\lambda$ [nm]	t [s]	$\lambda$ [nm]
A1	30	1483	5	1480	3	1477	2	1475	40	1475
A2	30	1478	3	1477	2	1476	0.5	1475	35.5	1475
A3	30	1482	7	1479	7	1475	-	1475	44	1475
B1	15	1485	-	1485	-	1485	-	1485	25	1485
B2	15	1492	16	1489	2	1488	2.5	1485	35.5	1485
B3	15	1494	16	1491	2	1489	3.8	1485	36.8	1485

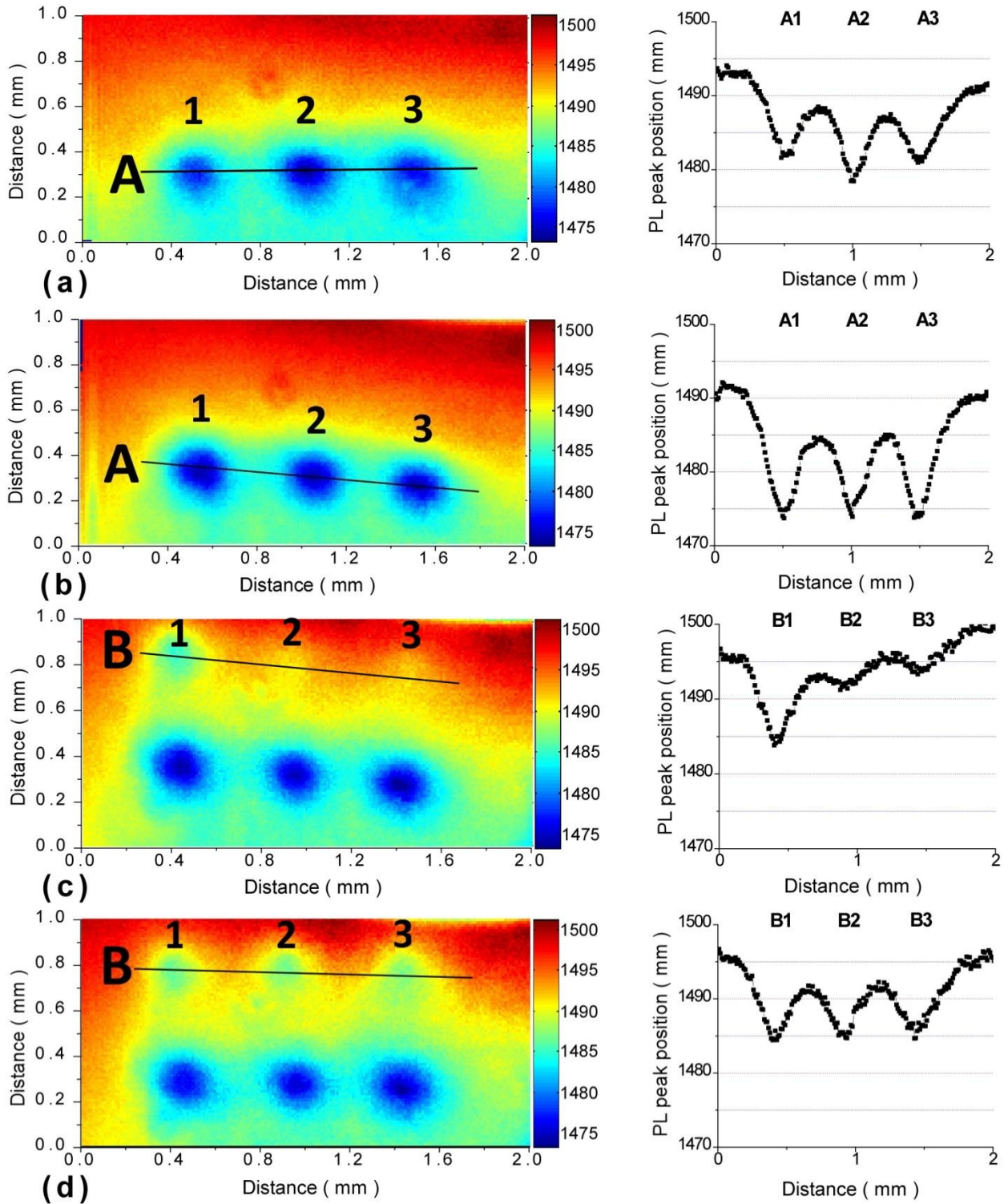
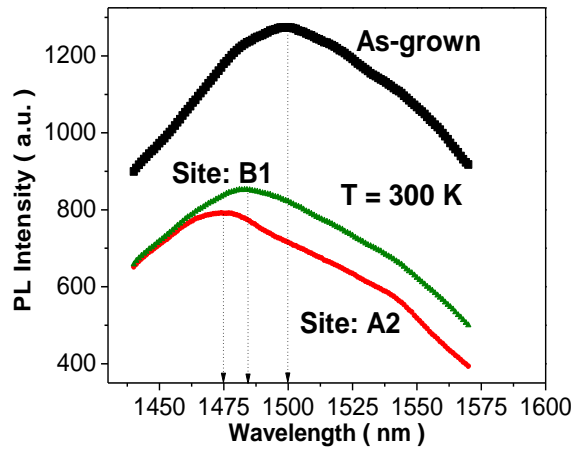


Figure 5.3.1 PL peak emission wavelength maps and corresponding cross-scans for A1, A2, A3, B1, B2, B3 following the 1st (a,c) and last (b,d) emission wavelength tuning steps.





### 5.3.2 PL spectra of the as-grown and 15 nm (green) and 25 nm (red) blueshifted materials.

The resulting blueshifted profile corresponds to the Gaussian-like laser beam profile induced processing temperature. Another important feature of this technique is that the PL signal intensity decreased by 35 % after the multiple consecutive annealing steps at room ambient conditions and was still a strong measurable signal at room temperature. Figure 5.3.2 presents the comparison of the three single spot PL curves of as-grown, 15 nm and 25 nm blueshifted InAs/InP materials. The broad signal is a result of dense self-assembled quantum dots population and large variation on their sizes. The results indicate that the Laser – RTA technique could be applicable to achieve controllable altering of the emission wavelength of a singular quantum dots.

### 5.3.3 Conclusion

Selective area QW and quantum dot (QD) emission wavelength tuning with sub-nanometer precision is demonstrated. Room ambient fabrication of the single-colour arrays of spots at emission wavelengths shifted by 70 nm for QW and 25 nm and 15 nm for QD material systems with  $\pm 0.5$  nm spectral precision has been performed with application of the developed mask-less IR (CW) Laser – Rapid Thermal Annealing (Laser – RTA) iterative bandgap engineering at selected areas (IBESA) technology. I have demonstrated the emission wavelength tuning of 8 arbitrary selected QWs spots from array of 20 spots to a desired value shifted by 70 nm from as

grown material on QWs semiconductor wafer. I have also demonstrated the emission wavelength tuning of array of 6 arbitrary area selected spots on InAs/InP QDs wafer from which 3 have been shifted by 25 nm and another 3 by 15 nm from the as grown material. This experiment has been performed to demonstrate the potential application of the Laser – RTA technique for single QD emission wavelength tuning.

## Summary and prospect

QWI can be achieved by using number of various approaches, ranging from methods that require specialized and expensive equipment (focused ion beam writing) to relatively simple and relatively inexpensive treatment that uses laser assisted semiconductor bandgap engineering techniques. This thesis concerns the development of IR CW Laser Rapid Thermal Annealing technique for spatially controlled and mask-free annealing of QS wafers. The 3D FEM modeling allowed for quantitative description of the IR Laser – QWI process carried out with either stationary or moving CW laser beams. The dynamics of the Laser-RTA process and the ability to anneal arbitrary shape patterns, e.g. spots, lines, circles, letters are well described with the 3D FEM approximation. The implementation of a 3D FEM modeling permitted the design of processing schemes that are required for accurate bandgap engineering at the wafer level. The IR Laser-RTA technique is based on using 150 W 980 nm fiber coupled laser diode and a 30 W TEM00 1064 nm Nd:YAG laser for background heating and direct ‘writing’ of the regions of QWI material respectively. The technique may be applied at room ambient conditions after capping the processed samples with SiO<sub>2</sub> cladding preventing sample’s decomposition at elevated temperatures. The innovation approach is based on the application of a 150 W 980 nm LD and a 30 W TEM00 Nd:YAG laser for simultaneous heating of the back and front sides of the wafer, respectively and application of custom developed web-cam based IR-camera for direct monitoring of the processing temperatures. The Laser-RTA technique generates heating rates of semiconductor wafers significantly exceeding those achieved with conventional RTA techniques. Typically, the overall processing times per site are shorter than 20 sec. The Laser-RTA technique allows controlled annealing with the irradiation times shorter than 1 sec. With a Nd:YAG laser focussed to a 0.5 mm spot, an array of 5 lines of the QWI material with bandgap blue-shifted by 15 nm has been successfully fabricated in a 10 mm x 14 mm sample. Each line of the QWI material is approximately 300 μm wide. I have illustrated the potential of the Laser-RTA technique in writing the arbitrary shape contours of the QWI material in the InGaAsP/InP QW microstructure. I have developed an image recognition based procedure that enables sample to return to its origin processing position after an ex-situ characterization step with 5 μm spatial, and 0.05 deg rotational precision. This feature has enabled me to introduce an innovative laser

annealing technique for iterative bandgap engineering at selected areas (IBESA). Consequently, I was able to demonstrate fine-tuning QS emission wavelength with spectral precision not worse than  $\pm 1$  nm. I have demonstrated a selective area processing of 8 sites chosen out of 20 sites array in an InGaAsP/InP QW wafer. The blueshift amplitude achieved in that case was  $70 \pm 1$  nm (from 1550 nm to 1480 nm). The IBESA processing of an InAs/InP QD wafer allowed fabricating 2 groups of 3 sites with ensembles of QDs whose emission was shifted, in each group, by  $15 \pm 0.5$  nm and  $25 \pm 0.5$  nm (from 1500 to 1485 and 1475 nm), respectively. The results of QD tuning have indicated the potential of the IBESA approach for tuning the emission wavelength of individual QDs. To achieve this with the current experimental setup would require samples with QDs separated by at least of 100  $\mu$ m from each other. Alternatively, working with more densely packed arrays of QDs should be possible if the IBESA setup were upgraded with an Nd:YAG laser beam optics delivering spots smaller than 10-20  $\mu$ m. The tests carried out in frame of this thesis were performed using only one Nd:YAG laser writing beam. In addition, multi-beam processing should also be possible, which would result in a significant decrease in overall processing times and a possibility of processing industrial size wafers.

I demonstrate the simple, reliable and universal IR (CW) Laser – RTA technology for IBESA QWI/QDI. I expect it will provide an important tool for photonic integration.

---

## Bibliography

- Adachi, S. (1987). "Model dielectric constants of Gap, GaAs, GaSb, InP, InAs, and InSb." Phys. Rev. B **35**(14): 7454-7463.
- Aimez, V., J. Beauvais, et al. (2002). "Low-energy ion-implantation-induced quantum-well intermixing." Selected Topics in Quantum Electronics, IEEE Journal of **8**(4): 870-879.
- Aimez, V., J. Beauvais, et al. (2001). "Monolithic intracavity laser-modulator device fabrication using postgrowth processing of 1.55  $\mu$  m heterostructures." Applied Physics Letters **79**(22): 3582-3584.
- Aspnes, D. E. and A. A. Studna (1983). "Dielectric functions and optical parameters of Si, Ge, GaP, GaAs, GaSb, InP, InAs, and InSb from 1.5 to 6.0 eV." Physical Review B **27**(2): 985.
- Bacewicz, R. (1995). Optyka ciała stałego. Wybrane zagadnienia. Warszawa.
- Beaudoin, M., A. J. G. DeVries, et al. (1997). "Optical absorption edge of semi-insulating GaAs and InP at high temperatures." Applied Physics Letters **70**(26): 3540-3542.
- Boon Siew, O., K. McIlvaney, et al. (1997). "Selective quantum-well intermixing in GaAs-AlGaAs structures using impurity-free vacancy diffusion." Quantum Electronics, IEEE Journal of **33**(10): 1784-1793.
- Boon Siew, O., O. Teik Kooi, et al. (2004). "Multiple-wavelength integration in InGaAs-InGaAsP structures using pulsed laser irradiation-induced quantum-well intermixing." Quantum Electronics, IEEE Journal of **40**(5): 481-490.
- Brunner, K., G. Abstreiter, et al. (1992). "Optical characterization of GaAs/AlGaAs nanostructures fabricated by focussed laser beam induced thermal interdiffusion." Surface Science **267**(1-3): 218-222.
- Brunner, K., U. Bockelmann, et al. (1992). "Photoluminescence from a single GaAs/AlGaAs quantum dot." Physical Review Letters **69**(22): 3216.
- Bugajski, M. and W. Lewandowski (1985). "Concentration-dependent absorption and photoluminescence of n-type InP." Journal of Applied Physics **57**(2): 521-530.
- Burkhard, H., H. W. Dinges, et al. (1982). "Optical properties of In<sub>[sub 1 - x]</sub>Ga<sub>[sub x]</sub>P<sub>[sub 1 - y]</sub>As<sub>[sub y]</sub>, InP, GaAs, and GaP determined by ellipsometry." Journal of Applied Physics **53**(1): 655-662.
- Burton, R. S., T. E. Schlesinger, et al. (1993). "High-performance diffusion disordered Al<sub>[sub x]</sub>Ga<sub>[sub 1 - x]</sub>As lasers via a self-aligned process and conventional open-tube annealing." Journal of Applied Physics **73**(4): 2015-2018.
- Casey, J. H. C., D. D. Sell, et al. (1975). "Concentration dependence of the absorption coefficient for n- and p - type GaAs between 1.3 and 1.6 eV." Journal of Applied Physics **46**(1): 250-257.
- Choi, W. J. (2000). Dependence of Dielectric Cap Quantum Well Disorder on the Characteristics of Dielectric Capping Film. Semiconductor Quantum Well Intermixing. E. H. Li. Amsterdam, Gordon and Breach. **8**.
-

- Cibert, J., P. M. Petroff, et al. (1986). "Kinetics of implantation enhanced interdiffusion of Ga and Al at GaAs-Ga<sub>x</sub>Al<sub>1-x</sub>As interfaces." Applied Physics Letters **49**(4): 223-225.
- COMSOL, I. COMSOL. Burlington.
- Cusumano, P., B. S. Ooi, et al. (1997). "Suppression of quantum well intermixing in GaAs/AlGaAs laser structures using phosphorus-doped SiO<sub>2</sub> encapsulant layer." Journal of Applied Physics **81**(5): 2445-2447.
- Dubowski, #160, et al. (1997). "A comparative study of laser- and ion implantation-induced quantum well intermixing in GalnAsP/InP microstructures." **2991**: IX, 294 p.
- Dubowski, J. J. (1999). "Semiconductor laser array fabricated by Nd:YAG laser-induced quantum well intermixing." Proc. of SPIE **1618**: 191.
- Dubowski, J. J. (2003). Laser-induced bandgap shifting for photonic device integration. USA. **6,670,644**.
- Dubowski, J. J. (2009). Laser-based Bandgap Engineering of Quantum Semiconductor Wafers.
- Dubowski, J. J., C. N. Allen, et al. (2000). "Laser-induced InAs/GaAs quantum dot intermixing." Applied Physics Letters **77**(22): 3583-3585.
- Dubowski, J. J., Y. Feng, et al. (2002). "Monolithic multiple wavelength ridge waveguide laser array fabricated by Nd:YAG laser-induced quantum well intermixing." Journal of Vacuum Science & Technology A: Vacuum, Surfaces, and Films **20**(4): 1426-1429.
- Dubowski, J. J., P. J. Poole, et al. (1999). "Enhanced quantum-well photoluminescence in InGaAs/InGaAsP heterostructures following excimer-laser-assisted surface processing." Applied Physics A: Materials Science & Processing **69**(0): S299-S303.
- Dubowski, J. J., C. Y. Song, et al. (2004). "Laser-induced selective area tuning of GaAs/AlGaAs quantum well microstructures for two-color IR detector operation." Journal of Vacuum Science & Technology A: Vacuum, Surfaces, and Films **22**(3): 887-890.
- Epler, J. E., R. D. Burnham, et al. (1986). "Laser induced disordering of GaAs-AlGaAs superlattice and incorporation of Si impurity." Applied Physics Letters **49**(21): 1447-1449.
- Fleming, R. M., D. B. McWhan, et al. (1980). "X-ray diffraction study of interdiffusion and growth in (GaAs)<sub>n</sub>(AlAs)<sub>m</sub> multilayers." Journal of Applied Physics **51**(1): 357-363.
- Genest, J., R. Beal, et al. (2008). "ArF laser-based quantum well intermixing in InGaAs/InGaAsP heterostructures." Applied Physics Letters **93**(7): 071106-071103.
- Genest, J., J. J. Dubowski, et al. (2004). UV-laser-based process for quantum well intermixing of III-V heterostructures. Integrated Optics and Photonic Integrated Circuits, Strasbourg, France, SPIE.
- Genest, J. and et al. (2007). "UV laser controlled quantum well intermixing in InAlGaAs/GaAs heterostructures." Journal of Physics: Conference Series **59**(1): 605.
- Glassbrenner, C. J. and G. A. Slack (1964). "Thermal Conductivity of Silicon and Germanium from 3°K to the Melting Point." Physical Review **134**(4A): A1058.
- H H Tan, S. Y., M. Gal, and C. Jagadish (2000). Optoelectronic properties of semiconductors and superlattices. Semiconductor Quantum Well Intermixing. E. H. Li. Amsterdam, Gordon and Breach. **8**.
- H. H. Tan, S. Y., M. Gal, and C. Jagadish (2000). Optoelectronic properties of semiconductors and superlattices. Semiconductor Quantum Well Intermixing. E. H. Li. Amsterdam, Gordon and Breach: 307.

- Heidrich, H. (2003). "Monolithically integrated photonic and optoelectronic circuits based on InP - System applications, technology, perspectives." Microsystem Technologies **9**(Compendex): 295-298.
- Helmy, A. S., J. S. Aitchison, et al. (1998). "Quantitative model for the kinetics of compositional intermixing in GaAs-AlGaAs quantum-confined heterostructures." Selected Topics in Quantum Electronics, IEEE Journal of **4**(4): 653-660.
- Hirayama, Y., S. Tarucha, et al. (1988). "Fabrication of a GaAs quantum-well-wire structure by Ga focused-ion-beam implantation and its optical properties." Physical Review B **37**(5): 2774.
- Holonyak, N. (1981). "IR-red GaAs-AlAs superlattice laser monolithically integrated in a yellow-gap cavity." Appl. Phys. Lett. **39**: 102.
- Holonyak, N., Jr. (1998). "Impurity-induced layer disordering of quantum-well heterostructures: discovery and prospects." Selected Topics in Quantum Electronics, IEEE Journal of **4**(4): 584-594.
- Ioffe, O.-T. I. from <http://www.ioffe.rssi.ru/SVA/NSM/Semicond>.
- Jagadish, H. H. T. Y. G. (2000). Semiconductor Quantum Well Intermixing. Amsterdam.
- Jellison, J. G. E. and F. A. Modine (1982). "Optical absorption of silicon between 1.6 and 4.7 eV at elevated temperatures." Applied Physics Letters **41**(2): 180-182.
- Johnson, S. R. and T. Tiedje (1995). "Temperature dependence of the Urbach edge in GaAs." Journal of Applied Physics **78**(9): 5609-5613.
- Kapon, E., N. G. Stoffel, et al. (1988). "BIREFRINGENT CHANNEL WAVE-GUIDES DEFINED BY IMPURITY-INDUCED SUPERLATTICE DISORDERING." Applied Physics Letters **52**(5): 351-353.
- Katayama, M., Y. Tokuda, et al. (1989). "X-ray photoelectron spectroscopic study of rapid thermal processing on SiO<sub>2</sub>/GaAs." Applied Physics Letters **54**(25): 2559-2561.
- Kelly, M. K., C. E. Nebel, et al. (1996). "Lateral structuring of III-V quantum well systems with pulsed-laser-induced transient thermal gratings." Applied Physics Letters **68**(14): 1984-1986.
- Laruelle, F., A. Bagchi, et al. (1990). "Focused ion beam channeling effects and ultimate sizes of GaAlAs/GaAs nanostructures." Applied Physics Letters **56**(16): 1561-1563.
- Liu, X. F., B. C. Qiu, et al. (2000). "Control of multiple bandgap shifts in InGaAs-AlInGaAs multiple-quantum-well material using different thicknesses of PECVD SiO<sub>2</sub> protection layers." Photonics Technology Letters, IEEE **12**(9): 1141-1143.
- Macfarlane, G. G., T. P. McLean, et al. (1959). "Exciton and phonon effects in the absorption spectra of germanium and silicon." Journal of Physics and Chemistry of Solids **8**: 388-392.
- Marsh, J. H. (1993). "Quantum well intermixing." Semiconductor Science and Technology(6): 1136.
- Marsh, J. H. (2000). Impurity-Free Vacancy Disordering of GaAs/AlGaAs Quantum Well Structures. Semiconductor Quantum Well Intermixing. E. H. Li. Amsterdam, Gordon and Breach. **8**.
- Marsh, J. H. (2005). Multiple anneal induced disordering. **WO/2005/057638**.
- Marsh, J. H., S. I. Hansen, et al. (1991). "Applications of neutral impurity disordering in fabricating low-loss optical waveguides and integrated waveguide devices." Optical and Quantum Electronics **23**(7): S941-S957.
-

- McKee, A., C. McLean, et al. (1997). "Monolithic integration in InGaAs-InGaAsP multiple-quantum-well structures using laser intermixing." IEEE Journal of Quantum Electronics **33**(1): 45-55.
- Miller, S. E. (1969). "Integrated optics: an introduction." Bell Syst. Tech. J. **48**: 205969.
- Nie, D., T. Mei, et al. (2006). "Argon plasma exposure enhanced intermixing in an undoped InGaAsP/InP quantum-well structure." Journal of Applied Physics **100**(4): 046103-046103.
- O. C. Zienkiewicz, R. L. T. (1996). The Finite Element Method. San Diego, Academic Press.
- Oleksandr Voznyy, R. S., Jan J. Dubowski (2006). "Multibandgap quantum well wafers by IR laser quantum well intermixing: simulation of the lateral resolution of the process." JLMN-Journal of Laser Micro/Nanoengineering **1**(1): 48-53.
- Ong, T. K. (1999). High spatial resolution quantum well intermixing process in GaInAs/GaInAsP laser structures. rd Pacific Rim conference on lasers and electro-optics. C. P. Rim'99. Seoul, Korea: 193.
- Palankovski, V., R. Schultheis, et al. (2001). "Simulation of power heterojunction bipolar transistors on gallium arsenide." Electron Devices, IEEE Transactions on **48**(6): 1264-1269.
- Palik, E. D. (1998). Handbook of Optical Constants of Solids.
- Pépin (2000). Selective Interdiffusion of GaAs/AlGaAs Quantum Wells through SiO<sub>2</sub> Encapsulation - Comparison with the Ion Implantation Approach. Semiconductor Quantum Well Intermixing. E. H. Li. Amsterdam, Gordon and Breach. **8**.
- Pépin, A., C. Vieu, et al. (1995). "Fabrication of quantum wires by selective intermixing induced in GaAs/AlGaAs quantum well heterostructures by SiO<sub>2</sub> capping and subsequent annealing." Superlattices and Microstructures **18**(3): 229-229.
- Petroff, P. M. (1977). "Transmission electron microscopy of interfaces in III--V compound semiconductors." Journal of Vacuum Science and Technology **14**(4): 973-978.
- Petroff, P. M., Y. J. Li, et al. (1991). "Nanostructures processing by focused ion beam implantation." Journal of Vacuum Science & Technology B: Microelectronics and Nanometer Structures **9**(6): 3074-3078.
- Prins, F. E., G. Lehr, et al. (1993). "Intermixed GaAs/AlGaAs quantum wires and the influence of implantation species on the steepness of the lateral potential." Journal of Applied Physics **73**(5): 2376-2380.
- Qiu, B. C., A. C. Bryce, et al. (1998). "Monolithic integration in InGaAs-InGaAsP multi-quantum-well structure using laser processing." Photonics Technology Letters, IEEE **10**(6): 769-771.
- Radoslaw Stanowski, O. V., Jan J. Dubowski (2006). "Finite element model calculations of temperature profiles in Nd:YAG laser annealed GaAs/AlGaAs quantum well microstructures." JLMN-Journal of Laser Micro/Nanoengineering **1**(1): 17-22.
- Ralston, J., G. W. Wicks, et al. (1986). "DEFECT STRUCTURE AND INTERMIXING OF ION-IMPLANTED ALXGA1-XAS/GAAS SUPERLATTICES." Journal of Applied Physics **59**(1): 120-123.
- Ralston, J. D., S. O'Brien, et al. (1988). "Room-temperature exciton transitions in partially intermixed GaAs/AlGaAs superlattices." Applied Physics Letters **52**(18): 1511-1513.
- Rastelli, A., A. Ulhaq, et al. (2007). "In situ laser microprocessing of single self-assembled quantum dots and optical microcavities." Applied Physics Letters **90**(7): 073120-073123.



- Ravindra, N. M., S. Abedrabbo, et al. (1998). "Temperature-dependent emissivity of silicon-related materials and structures." Semiconductor Manufacturing, IEEE Transactions on **11**(1): 30-39.
- Ravindra, N. M., P. Ganapathy, et al. (2007). "Energy gap-refractive index relations in semiconductors - An overview." Infrared Physics & Technology **50**(1): 21-29.
- Stanowski, R., S. Bouaziz, et al. (2008). Selective area bandgap engineering of InGaAsP/InP quantum well microstructures with an infrared laser rapid thermal annealing technique. Photon Processing in Microelectronics and Photonics VII, San Jose, CA, USA, SPIE.
- Stanowski, R. and J. J. Dubowski (2009). "Laser rapid thermal annealing of quantum semiconductor wafers: a one step bandgap engineering technique." Applied Physics A-Materials Science & Processing **94**(3): 667-674.
- Stanowski, R., M. Martin, et al. (2009). "Iterative bandgap engineering at selected areas of quantum semiconductor wafers." Optics Express **17**(22): 19842-19847.
- Stanowski, R., Voznyy O., Dubowski J.J. (2005). Modelling of temperature profiles in Nd:YAG laser annealed GaAs/AlGaAs quantum well microstructures. Laser Applications in Microelectronic and Optoelectronic Manufacturing X. San Jose, SPIE.
- Stanowski, V., Dubowski (2006). "Finite element model calculations of temperature profiles in Nd:YAG laser annealed GaAs/AlGaAs quantum well microstructures." JLMN-Journal of Laser Micro/Nanoengineering **1**(1): 17-22.
- Steen, M. W. (1998). Laser Material Processing. Berlin, Springer.
- Sturge, M. D. (1962). "Optical Absorption of Gallium Arsenide between 0.6 and 2.75 eV." Physical Review **127**(3): 768.
- Sze, S. M. (1981). Physics of Semiconductor Devices. New York, Wiley.
- TIEMEIJER, J. J. M. B. P. J. A. T. T. v. D. E. J. J. A. A. M. T. S. G. N. v. d. H. L. F. (1997). "Characterization of Butt-Joint InGaAsP Waveguides and Their Application to 1310 nm DBR-Type MQW Gain-Clamped Semiconductor Optical Amplifiers." IEICE TRANSACTIONS on Electronics **E80-C**(5): 675.
- Timans, P. J. (1992). "The experimental determination of the temperature dependence of the total emissivity of GaAs using a new temperature measurement technique." Journal of Applied Physics **72**(2): 660-670.
- Trivedi, D. A. and N. G. Anderson (1996). "Modeling the near-gap refractive index properties of semiconductor multiple quantum wells and superlattices." Selected Topics in Quantum Electronics, IEEE Journal of **2**(2): 197-209.
- Turner, W. J., W. E. Reese, et al. (1964). "Exciton Absorption and Emission in InP." Physical Review **136**(5A): A1467.
- Vieu, C., M. Schneider, et al. (1991). "Optical characterization of selectively intermixed GaAs/GaAlAs quantum wires by Ga[<sup>+</sup>] masked implantation." Journal of Applied Physics **70**(3): 1444-1450.
- Voznyy, S., Stanowski, R., Dubowski (2006). "Multibandgap quantum well wafers by IR laser quantum well intermixing: simulation of the lateral resolution of the process." JLMN-Journal of Laser Micro/Nanoengineering **1**(1): 48-53.
- Wallin, J., G. Landgren, et al. (1992). "Selective area regrowth of butt-joint coupled waveguides in multi-section DBR lasers." Journal of Crystal Growth **124**(1-4): 741-746.
- Yap, D., K. R. Elliott, et al. (2001). "High-speed integrated optoelectronic modulation circuit." Photonics Technology Letters, IEEE **13**(6): 626-628.
-


# Appendix

## LabVIEW interface for IR Laser – RTA IBESA technique

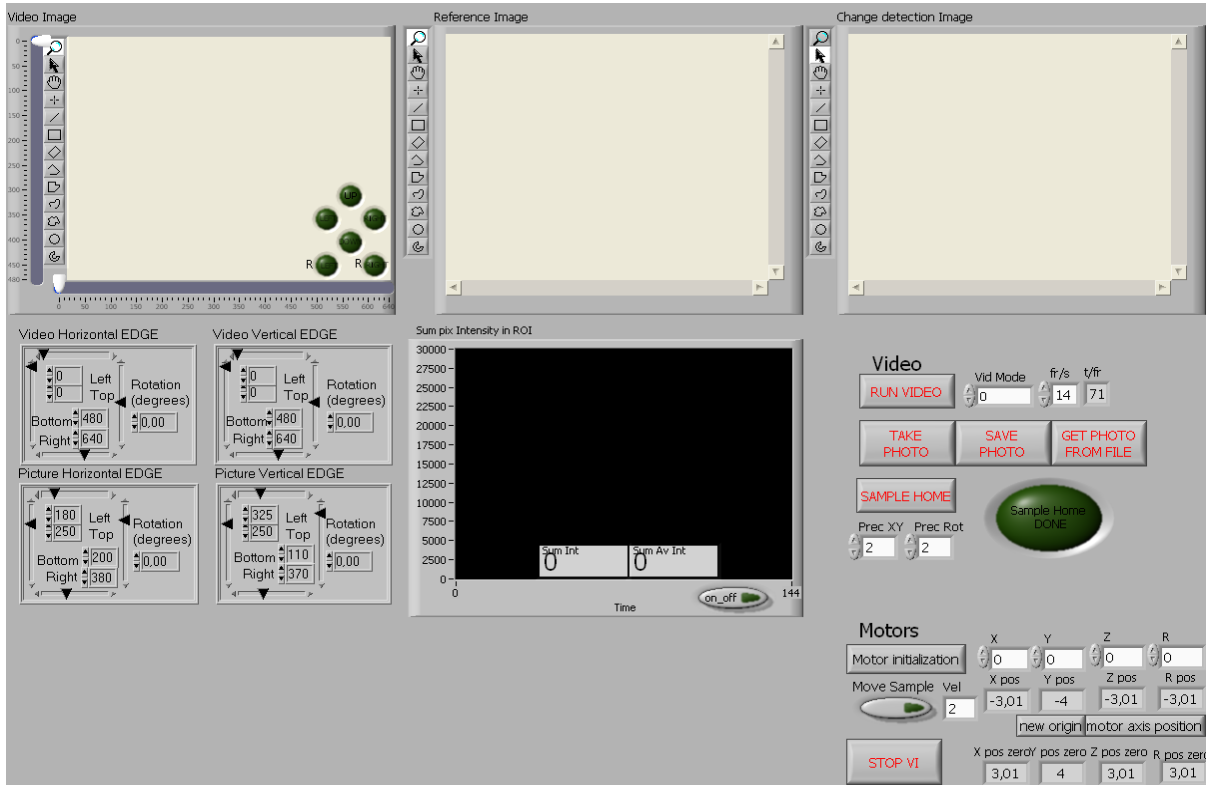


**Figure 0.1** LabVIEW based IR Laser – RTA IBESA interface. In-situ process monitoring, position or reposition section.

The IR LabVIEW IBESA interface is presented in two parts in figures 6.1.1 and 6.1.10. The first part concerns the sample's repositioning technique while the second part concerns the setting of the Laser – RTA processing parameters and the performing of the experiment. The three image processing windows: 'Video Image', 'Reference Image' and 'Change detection Image' are used to display the Vis-CAM video stream, steady image of sample's position of origin, and calculated differential image between the 'Reference Image' and 'Video Image' windows, respectively. For the purpose of sample repositioning, the user is required to follow the processing steps presented in figure 6.1.2. After the initialization of motors, the user should perform the proper adjustments of the arbitrary sample's processing position. The user is

required to press the ‘RUN VIDEO’  button, which turns on the VIS-CAM and allows for sample’s position monitoring.

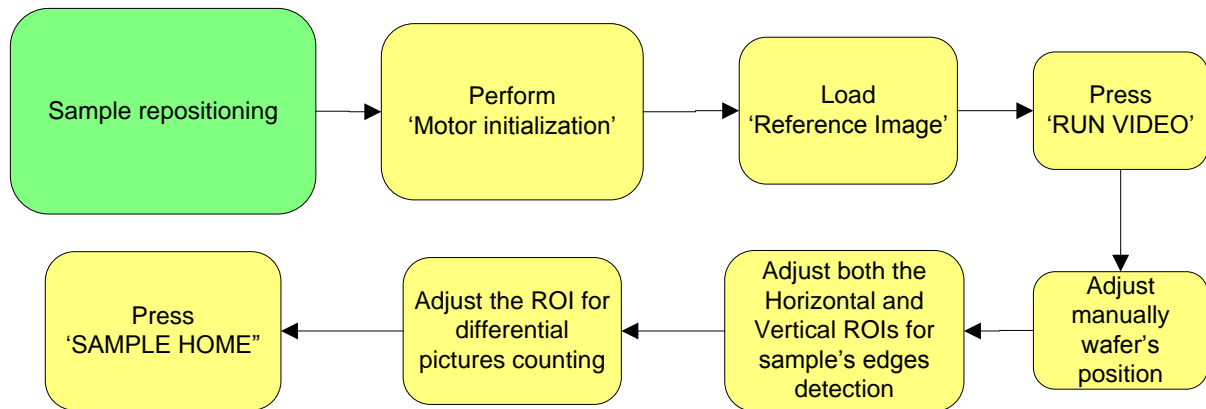


**Figure 0.2 Block diagram of sample repositioning processing steps.**

The user must pay attention to adapt such an experimental sample’s position that provides the most stable edge detection conditions. I have enhanced the edge detection accuracy by placing the silicon wafer with its unpolished-side-up to support the processed sample placed with its polished side up. The enhanced precision edge detection by contrast improvement for the sample RA30360 placed on silicon wafer is illustrated in figure 6.1.3. The actual sample’s position, monitored in real time is displayed in the ‘Video image’ window. The video stream from the Vis-CAM is analyzed in frame-by-frame mode. The controls named ‘Video Horizontal EDGE’ and ‘Video Vertical EDGE’ allow specifying the regions of interest (ROI) wherein separately the

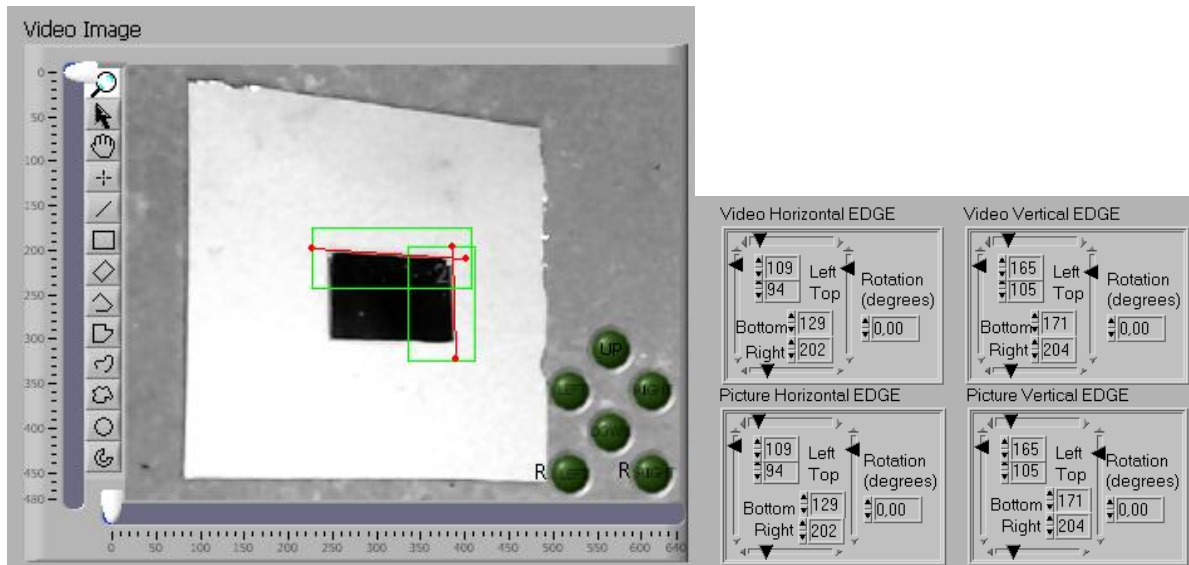


**Figure 0.3 Video Image with detected horizontal and vertical sample's edges**

horizontal and vertical edges would be detected on the video stream in the separate ROIs that have visible green color border frames. The user is required to specify arbitrarily the area of ROI to detect edges that the sample repositioning procedures will work on. The detected edges are marked by the straight red lines. The ROIs area is adjusted in such a manner that will produce the most stable behaviour of the edges detection red-color markers. It could be useful to rotate the sample by  $\pm 3-5$  deg, so there would be more pixels involved inside the region of interest to detect the processed sample's edge accurately. Once both the horizontal and vertical edges are detected, the user can register the sample's position of origin by saving its position's still image 'Reference Image' and save it on the computer's HDD. to the user presses the buttons 'TAKE PHOTO'  and 'SAVE PHOTO'  sequentially. After this procedure, the user proceeds with the IBESA IR Laser-RTA experiment and takes the sample for ex-situ characterization. It is necessary to note for future reference the 'Video Horizontal EDGE' and 'Video Vertical EDGE' ROIs parameters. To reposition the sample to its origin position after the ex-situ characterization step, it is necessary to compare the sample's origin position image stored on the HDD with its real-time position acquired by VIS-CAM. Values in 'Picture Horizontal EDGE' and 'Picture Vertical EDGE' should be adjusted to match values in 'Video Horizontal EDGE' and 'Video Vertical EDGE' respectively. User has to adjust them manually.

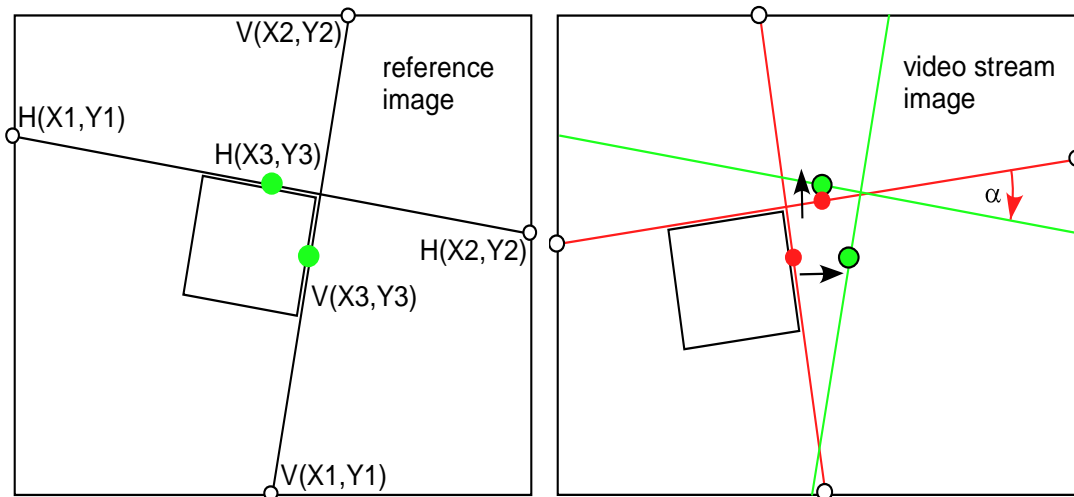


**Figure 0.4** Sample on processing stage. Two straight lines denominate its position in the camera's field of view.


To load sample's image from the computer HDD to the 'Reference Image' window it is necessary to stop the actual position video acquisition, so choose  and then press 'GET PHOTO FROM FILE'  button. The image will be loaded and edges detected. The horizontal and vertical edges on the reference image were detected and during the repositioning procedure, were compared with their corresponding horizontal and vertical edges, which detected on each consecutive frame of the video stream. The arithmetical center of each line is calculated to achieve an average position of each line with fraction of a pixel precision. This produced an increase in precision of this technique to singular micrometers. Figure 6.1.4 demonstrates the alignment procedure that compared the position of arithmetical center of horizontal line on video stream versus that on the reference image. If the distance in pixels was greater than required precision the "move" command would be sent to the appropriate motor to get the sample's position corrected. Afterwards, the same procedure was applied to the vertical axis position. Finally the angle between horizontal line on video stream and horizontal line on reference image were calculated and sample was rotated. These three detection steps were consecutively executed until the required precision was met for all of them. During the sample repositioning process the actual direction of the correction movement is indicated by illumination of the green circular indicators placed on 'Video Image' window and presented in figure 6.1.5. At this moment, the user can turn on the actual position video acquisition by clicking on the


**RUN VIDEO** button. The user positions the sample with 1-2 mm precision to its position of origin– it is useful to look in the Video Image window during the manual sample repositioning stage. Once the sample’s edges are in the ROIs fields it is possible to get advantage of the automated sample repositioning routine. User should choose the ‘SAMPLE

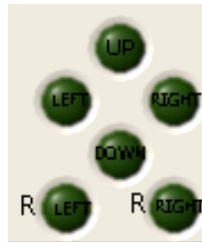


**Figure 0.5 Console presenting actual direction of sample's movement**

HOME’ **SAMPLE HOME** button and wait till the ‘Sample Home DONE’  indicator color

turns to green . During the sample’s repositioning process the motors’ step precision

values are displayed . This value is displayed in pixels of the VIS-CAM units. At any moment, the user can estimate the quality of the sample’s repositioning adequacy by observing the ‘Change detection Image’ window presented in figure 6.1.6. The user is required to adjust the size of the ROI following the processed sample’s dimensions. A particular problem represent mechanical stage’s motors which have the positioning error greater than 1  $\mu\text{m}$  while performing singular incremental moves. Therefore a “differential pixels intensity counting” technique presented in figure 6.1.7 was developed and implemented to improve the technique’s accuracy and diminish error corresponding to X, Y, Theta mechanical motors inertia. It also serves as an alternative method of sample’s repositioning error elimination. To assure that repositioning accuracy error corresponds only to the sample’s position misalignment a special region of interest selecting only the processed sample and some part of the unpolished silicon wafer was selected as the ROI.

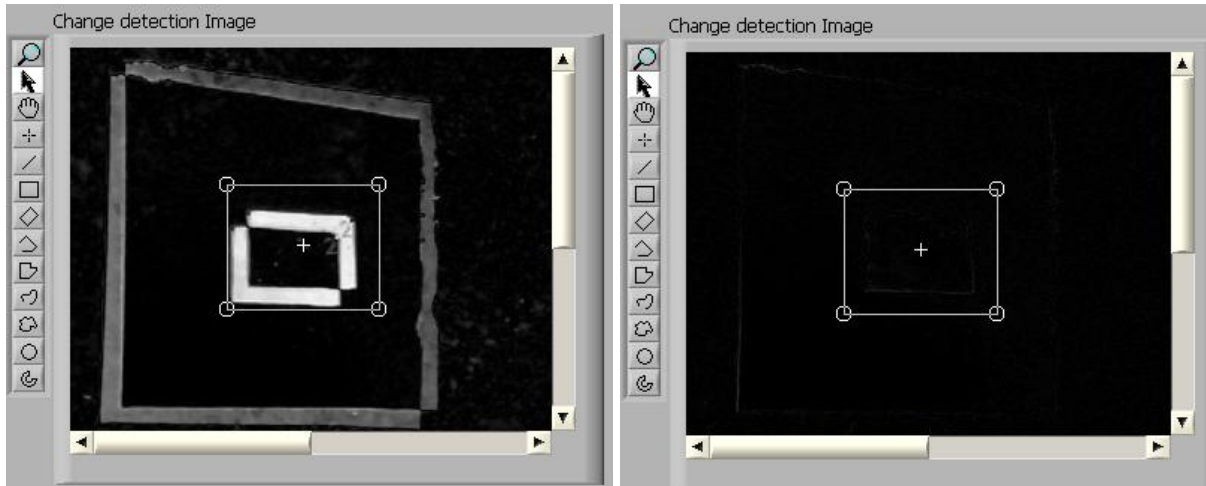


**Figure 0.6** Change detection image a) before and b) after sample's repositioning process

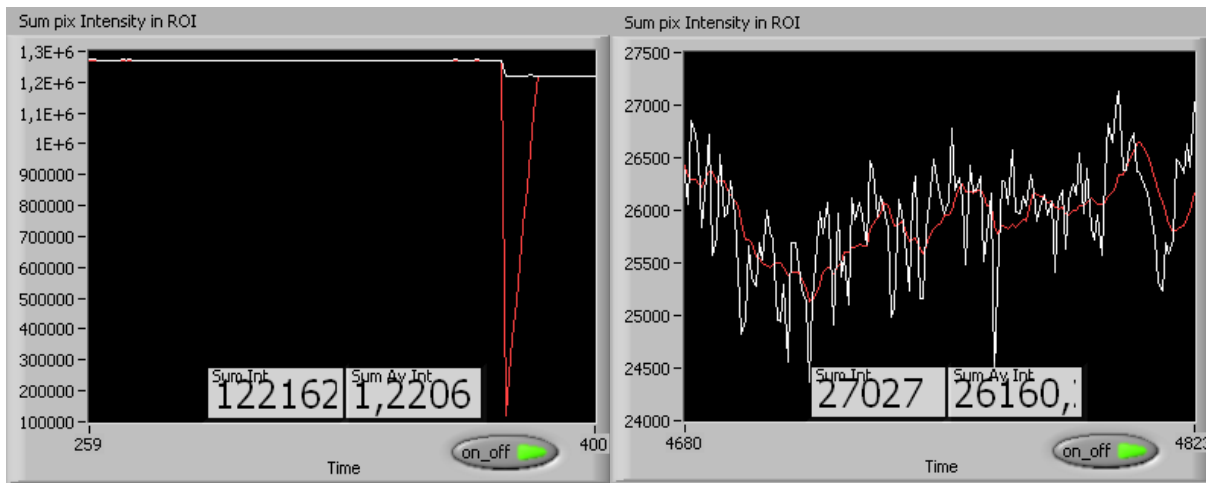


**Figure 0.7** Sum pix Intensity in ROI a) before and b) after sample's repositioning process

The user has to pay the particular attention to the estimation of the noise level of the VIS-CAM pixels intensities. Figure 6.1.7 (a) and Fig. 6.1.7 (b) present the parts of the ‘Sum pix Intensity in ROI’ plots corresponding to the beginning stage and final stage of the sample’s repositioning process shown in figures 6.1.6 (a) and 6.1.6 (b) respectively. Figure 6.1.8 presents the plot of ‘Sum of differential pixels intensity’ collected during the full sample’s repositioning procedure. For each differential video stream frame in real time there has been calculated the total sum of differential pixels intensities inside the selected ROI.

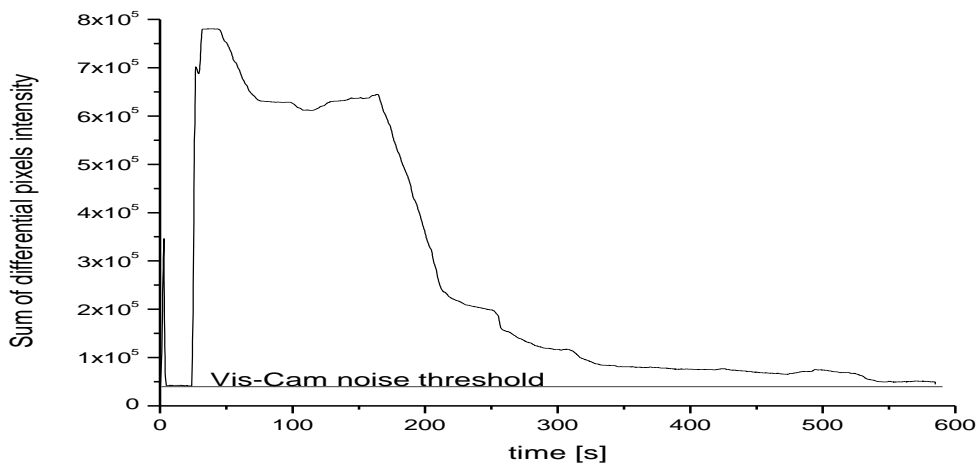


**Figure 0.8 Sample repositioning technique based on differential pixels intensity counting.**

It can be seen that the process takes about 10 min and constitutes a fully automated procedure. This technique's precision depends strongly on the camera's sensor resolution, white noise, and optical magnification capability, so its ultimate resolution could be greatly improved by using a high quality, cooled and faster CCD detector. A sample's differential image was also used to center LD, Nd:YAG and pyrometer measurement spot on same sample's cross-section axis by detecting the peak intensity on both infra-red laser beam profiles. It is also possible to perform the arbitrary sample's displacements with X, Y, Z and Theta (rotation) motors with the 'Motors' section presented in figure 6.1.9. To perform the 'Move Sample' command the user is required to initialize motors by choosing the 'Motor initialization'  button. The X pos, Y pos, Z pos, R pos fields will be zeroed. After motors initialization user can input the arbitrary displacement values to set new position in the X, Y, Z, R edit fields and press 'Move sample'  button. User can choose the average velocity of the motors movement from 0 – 2 in the field 'Vel' . Additionally at all times, the user can select the current position as 'new Origin' position and press the  button. This will set X pos, Y pos, Z pos, R pos to zero. This section also allows for the in-situ process monitoring with both 1064 nm and 980 nm infrared laser beams and verification of their spots' diameters. It provides also a precise and practical technique as the alignment tool for the pyrometer's detecting spot focal distance adjustment.



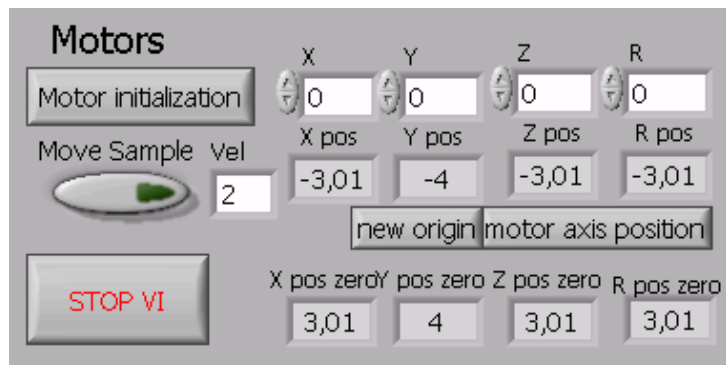
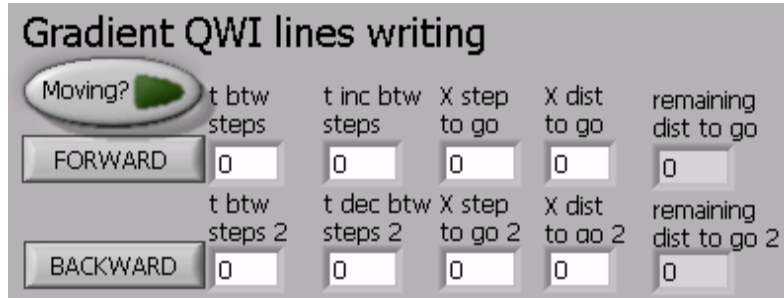


Figure 0.9 Move sample routine.



Figure 0.10 LabVIEW based IR Laser – RTA IBESA interface. Automated processing routines.

A custom designed module has been developed for sample's displacement with variable velocity. It is called 'Gradient QWI lines writing' and it is presented in figure 6.1.11. User is required to input the processing parameters into corresponding editable fields. For example to move the sample forward by 10 mm with a step of 1 mm and time 1 second for the first



**Figure 0.11 Variable speed sample displacement module**

step and 0.1 second time increment between steps it is necessary to input 't btw steps' = 1 [s]; 't inc btw steps' = 0.1 [s]; 'X step to go' = 1 [mm]; 'X dist to go' = 10 [mm]. During the movement the indicator 'Moving' will turn light green and the remaining distance to go will be displayed in 'remaining dist to go' indicator field. I have developed a custom interface to communicate with the commercial MIKRON M680 pyrometer, for the purpose of creating the feed-back loop to control automatically the LD output power. I have developed the whole driver from scratch because it was not provided by the manufacturer. It can retrieve the measurement data with 10 Hz frequency and indicate the temperature value in a numeric indicator field as well as plot it on a chart presented in figure 6.1.12. The temporal temperature reflects the actually measured most recent temperature value. However to avoid the overshooting of the processing temperature I have implemented an algorithm to predict the temperature value and upon this prediction adjust the IR Laser Diode current increase.

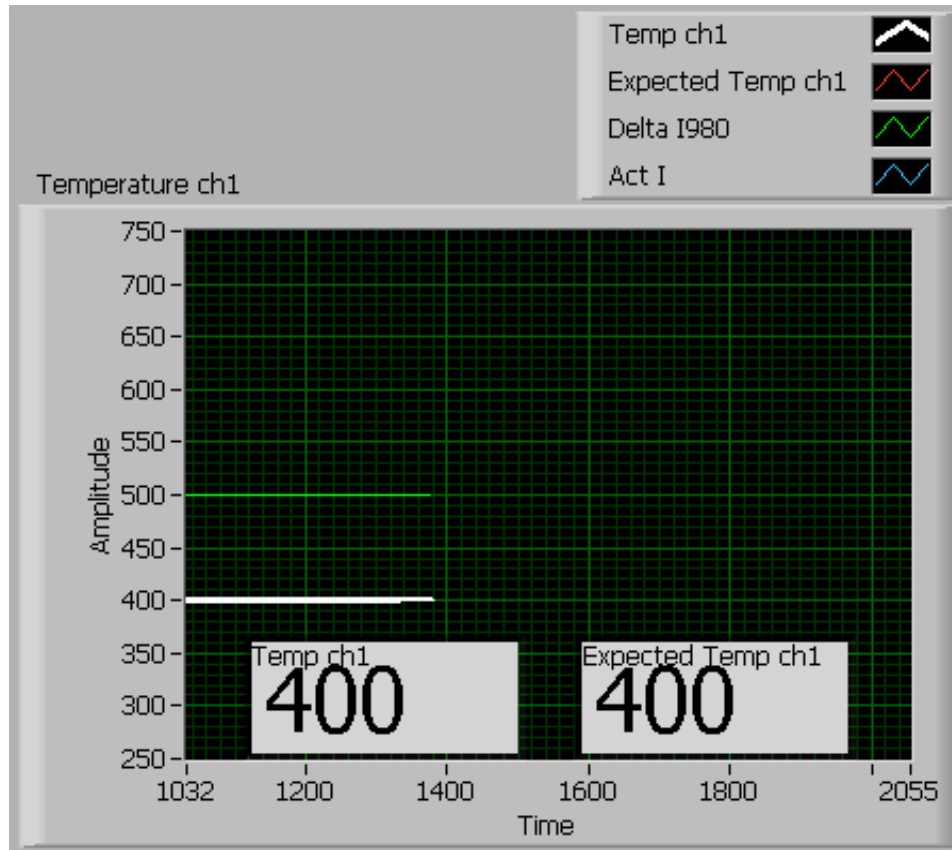


**Figure 0.12 Measured and expected temporal temperature behavior measured with the first channel of M680 pyrometer**

The expected temperature is calculated by finding the difference between the most recent measured temperature value and its previous value then if the difference is positive multiplies its value by a factor of three and adds to the just measured temperature value but if the just measured temperature is smaller than previous it does not modify it and takes it as expected. In such a case the system can much sooner decrease the IR LD current increment and avoid temperature overshooting the desired processing temperature value. In the ‘Temperature ch1’ window chart there are plotted beside the temperature values the ‘Delta I980’ and ‘Act I’ values corresponding to IR LD current increase and actual IR LD current.

To perform fast temperature mapping I have additionally developed the LabVIEW based interface for communication with the custom developed IR-CAM. Having a map-at-once approach it is possible to verify sample’s temperature distribution. The interface is presented in figure 6.1.13. The IR-CAM module presents a raw Video Image 4 signal and random noise

filtered signal. To filter out the inherent to the inexpensive webcam detector random noise I have applied the low pass filter with X Size = 3, Y Size = 3 and Tolerance % =10. That allowed filtering out the random noise. The applied algorithm allows also tracking the highest intensity pixel value in the custom selected ROI. It displays the hottest pixel's value and marks it on the camera image. It calculates as well the average temperature from the ROI area. On the corresponding chart it plots the 'Act I', 'Temp ch 1', 'T max', 'T average' values.

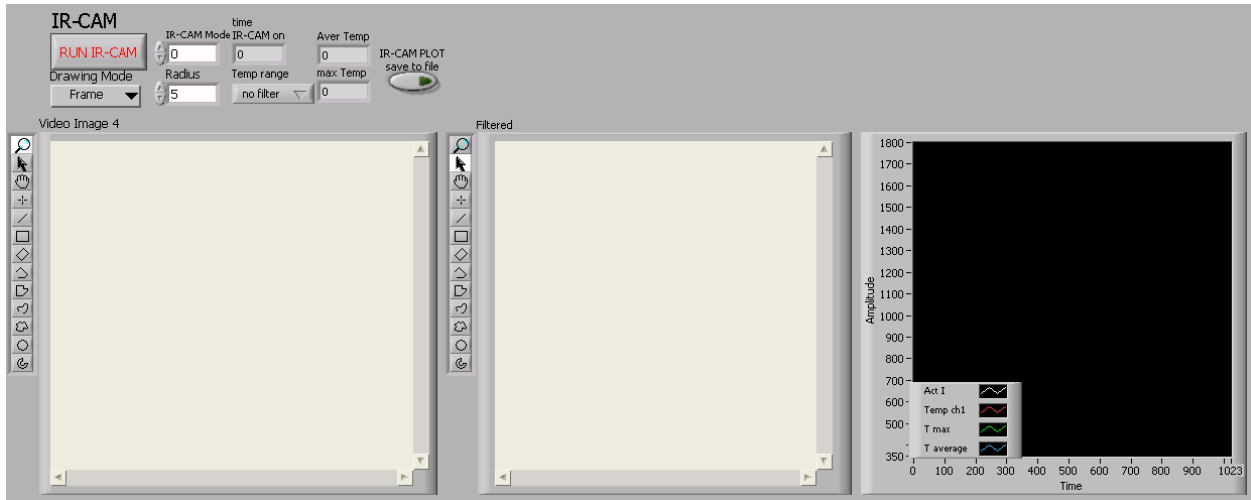


Figure 0.13 IR-CAM module



Figure 0.14 Nd:YAG galvo-scanner interface controller

LabVIEW platform does not support multiple USB cameras in parallel sessions, so as a disadvantage the VIS-CAM cannot be used at the same time with the IR-CAM. I have developed a custom interface module presented in figure 6.1.14 to control the position of the Nd:YAG laser galvo-scanner. This module enables the user to move the laser beam to any

arbitrary position by setting its mm corresponding value in volts into the 'X YAG'  and 'Y

YAG'  corresponding edit fields. There is also a possibility to store two sets of X, Y coordinates for quick laser beam position switching. When the laser beam is at the proper position 'to wait', user is required to choose the 'Set wait pos'  button and respectively when the laser beam is at the proper position to process user is required to choose the 'Set intx pos'  button. The coordinates in volts units are stored and displayed in the 'X wait', 'Y wait' and 'X intx' and 'Y intx' numeric indicator text fields respectively. User can at this moment quickly move the Nd:YAG laser beam between the 'process position' and 'wait position' by choosing the buttons 'Move to wait pos'  and 'Move to intx position'  respectively. Another module presented in figure 6.1.15 allows to monitor stability of the Nd:YAG laser. It takes advantage of a photo-diode detector installed behind the 99.9% Nd:YAG cavity mirror. The induced photo-voltage in the photo-diode can be monitored after the user turns on the 'Nd:YAG power'  button.

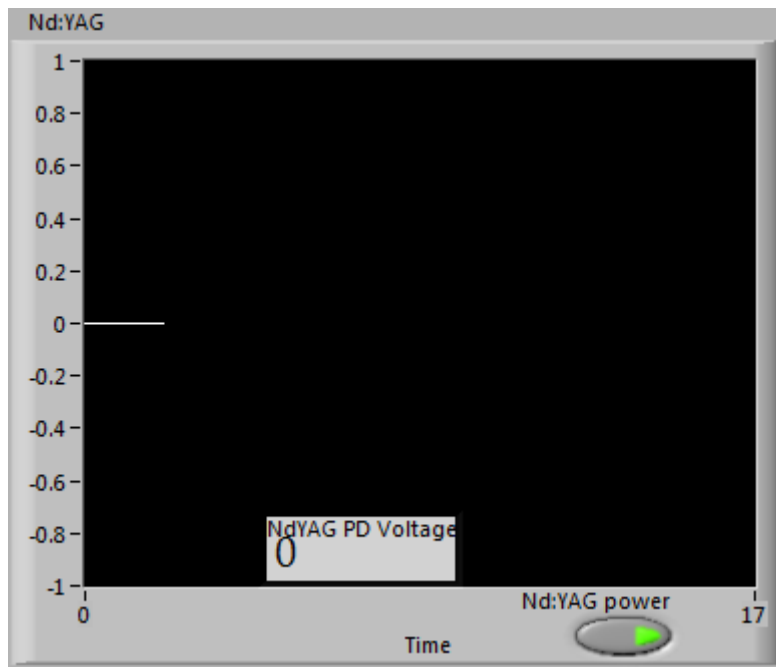
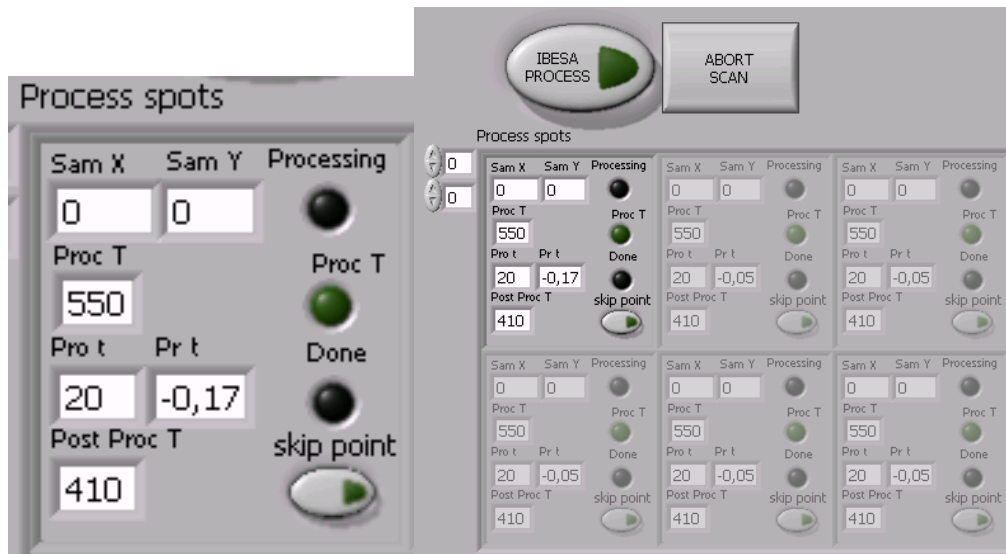


Figure 0.15 Nd:YAG power stability monitor

The photo-voltage is then plotted in real-time on the Nd:YAG chart and its numeric value is displayed on the 'Nd:YAG PD Voltage' numeric indicator text field. The IR LD power can be controlled by the 'LD & Pyro fd-bk loop' module presented in figure 6.1.16. It allows for setting the initial current value and also increment or decrement the IR LD current during the experiments. After first communication with the IR LD system, the numeric indicator field displays the actual current value in the 'Act I' numeric indicator text field. The IBESA PROCESS routine module presented in figure 6.1.17 is to automate the Laser-RTA process for selective area QWI.

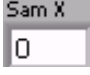
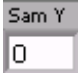
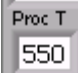
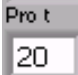
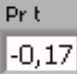




**Figure 0.16 IR LD current control module**



**Figure 0.17 IBESA PROCESS routine module**

It is designed to process arbitrary number of QW/QD sites on the wafer. The module consists of an array of cluster blocks activated after entering the processing parameters. The two dimensional array of clusters is expandable. Each cluster consists of same elements. Values of spot's position, processing temperature and time and also background temperature should be set

separately for every spot. Spot position in mm unit should be input into ‘Sam X’  and ‘Sam Y’  numeric edit fields. Processing temperature into ‘Proc T’  numeric edit field. Processing time in seconds units should be input into ‘Pro t’  numeric edit field. The processing remaining time is displayed for each point in the ‘Pr t’  numeric edit field automatically. The sample’s background temperature value is input into ‘Post Proc T’  numeric edit field. During the IBESA processing it might be necessary to skip a spot. For this purpose the ‘skip point’  button should be selected.

The processed spots will indicate the current processing stage with the Boolean indicators

‘Processing’, ‘Proc T’ and ‘Done’. .

## Articles written during the PhD thesis:

R. Stanowski, M. Martin, R. Arès, J.J. Dubowski (2009). **"Iterative bandgap engineering at selected areas of quantum semiconductor wafers"**

Optics Express **17**(22): 19842-19847.

DOI:10.1364/OE.17.019842

Stanowski, R. and J. J. Dubowski (2009). **"Laser rapid thermal annealing of quantum semiconductor wafers: a one step bandgap engineering technique"**

Applied Physics A-Materials Science & Processing **94**(3): 667-674.

DOI: 10.1007/s00339-008-4955-7

R. Stanowski, S. Bouaziz, J.J. Dubowski (2008). **"Selective area bandgap engineering of InGaAsP/InP quantum well microstructures with an infrared laser rapid thermal annealing technique"**, Photon Processing in Microelectronics and Photonics VII,

SPIE proceedings, Vol. 6879, pp.68790D-68790D-8.

DOI: 10.1117/12.774828.

R. Stanowski, O. Voznyy, J.J. Dubowski (2006). **"Finite element model calculations of temperature profiles in Nd:YAG laser annealed GaAs/AlGaAs quantum well microstructures"**

JLMN-Journal of Laser Micro/Nanoengineering **1**(1): 17-22.

O. Voznyy, R. Stanowski, J.J. Dubowski (2006). **"Multibandgap quantum well wafers by IR laser quantum well intermixing: simulation of the lateral resolution of the process."**

JLMN-Journal of Laser Micro/Nanoengineering **1**(1): 48-53.

---



## Conference presentations during the PhD thesis

R. Stanowski, J.J. Dubowski, "**Laser tuning of InAs quantum dot emission wavelength**",  
14th Canadian Semiconductor Technology Conference, Hamilton, Canada, August 10-14 (2009);

R. Stanowski, J.J. Dubowski, "**Iterative laser rapid thermal annealing for monolithically integrated GaAs/AlGaAs photonic devices**",  
PHOTONICS WEST, LASE 2009, San Jose, USA, January 24-29, (2009);

R. Stanowski, M. Martin, J.J. Dubowski, "**Local-area infrared laser engineering of bandgap gradient controlled quantum well semiconductor wafers**",  
LPM 2008, Quebec City, Canada, June 16-20 2008;

R. Stanowski, J.J. Dubowski, "**Infrared laser-induced bandgap engineering technique for fabrication of multi-bandgap quantum well semiconductor wafers**",  
PHOTONICS NORTH 2008, Montreal, Canada, June 2-4 (2008);

R. Stanowski, J.J. Dubowski, "**Selective area bandgap engineering of AlGaAs/GaAs quantum well microstructures with a laser rapid thermal annealing technique**",  
PICALO 2008, Beijing, China, April 16-18, (2008);

R. Stanowski, S. Bouaziz, J.J. Dubowski, "**Selective area bandgap engineering of InGaAsP/InP quantum well microstructures with an infrared laser rapid thermal annealing technique**",  
PHOTONICS WEST, LASE 2008, San Jose, USA, January 19-24, (2008);  
Photon Processing in Microelectronics and Photonics VII, SPIE proceedings, Vol. 6879,  
pp.68790D-68790D-8.  
DOI: 10.1117/12.774828.

R. Stanowski, O. Voznyy, J.J. Dubowski, "**Finite element model calculations of temperature profiles in Nd:YAG laser annealed GaAs/AlGaAs quantum well microstructures**",  
LPM 2005, Williamsburg, USA, April 4-8, (2005);

---